

**STUDY OF DEEP EARTH STRUCTURE USING
CORE PHASES AND THEIR SCATTERED
ENERGY RECORDED AT
SEISMIC ARRAYS**

Zuihong Zou, M.S.

An Abstract Presented to the Faculty of the Graduate
School of Saint Louis University in Partial
Fulfillment of the Requirements for the
Degree of Doctor of Philosophy

2008

Abstract

In the thesis, I endeavor to explore the structure of the Earth's deep interior by analyzing seismic core phases and their related scattered energy generated by small-scale heterogeneities inside the Earth. By modeling the differential traveltimes and amplitude ratios between PKP-DF and PKP-Cdiff measured from a large dataset recorded at seismic arrays, I find that the optimum model by fitting the differential travel times has relatively low velocity at the base of the outer core as in AK135, however, the optimum model found by fitting the amplitude ratios does not exhibit this feature, and instead is closer to PREM. The discrepancy may be explained by small-scale topography on the inner core boundary (ICB) or a thin layer with relatively low Q at the base of the outer core. I also analyzed the coda waves following PKP-Cdiff to locate the lateral heterogeneity and to attempt to understand its nature. By combined modeling of the travel times, slownesses, and envelopes of the coda waves, I find a very strong heterogeneity in the lowermost mantle beneath the Amazon River in South America. To examine the strength of small-scale random heterogeneities in the mantle, I assembled a large, geographically diverse data set of PKP precursor envelopes from globally distributed international monitoring system seismic arrays. I find that the amplitudes of the precursors change from region to region, and exhibit significant variations within specific geographic regions. This may imply that the lower mantle is not perfectly mixed by mantle convection, and that compositional heterogeneities can survive in the mantle for billions of years. By modeling the globally averaged PKP precursors using a seismic phonon method, my results show that a model with random heterogeneities at a scale-length of 8 km with 0.05% r.m.s. velocity perturbation uniformly distributed throughout the lower mantle can provide a reasonable fit to the observations. On the contrary, confining the heterogeneities near the core mantle boundary (CMB) or in the D'' does not yield the amplitude versus time pattern observed in our data. Furthermore, extra scattering near the CMB or in the D'' is not justified.

**STUDY OF DEEP EARTH STRUCTURE USING
CORE PHASES AND THEIR SCATTERED
ENERGY RECORDED AT
SEISMIC ARRAYS**

Zuihong Zou, M.S.

A Dissertation Presented to the Faculty of the Graduate
School of Saint Louis University in Partial
Fulfillment of the Requirements for the
Degree of Doctor of Philosophy

2008

©Copyright by
Zuihong Zou
ALL RIGHTS RESERVED

2008

COMMITTEE IN CHARGE OF CANDIDACY:

Associate Professor Keith D. Koper,
Chairperson and Advisor

Professor Robert B. Herrmann

Associate Professor Lupei Zhu

Acknowledgments

First of all, I owe the deepest gratitude to my parents and my siblings. It is your unconditional love and support that gave me beautiful dreams and made my dreams come true.

I am deeply grateful to my advisor, Dr. Keith D. Koper, for his kindness, guidance, advice, support, and stimulating discussions throughout my PhD study and research at SLU. It was his suggestions and ideas that guided me through all the ups and downs of my research to reach this point. I am so grateful for the four years' great learning experiences, which will be extremely beneficial to my future career.

I deeply thank Dr. Lupei Zhu and Dr. Robert B. Herrmann for their careful and detailed reviews of the thesis and their persistent help and advice during my four years of graduate study at SLU. I thank Dr. David J. Crossley, Dr. John Encarnacion, Dr. Timothy M. Kusky, Dr. David Kirschner and Dr. Brian J. Mitchell. The knowledge and skills I've learned from them will be a priceless fortune for the rest of my life. Thank you all so much for your teaching, advice, sharing your experiences, kindness and friendship. And also, I must acknowledge my master's thesis advisor, Dr. Xiaofei Chen at Peking University, who had a significant influence on my research interest and has been helping and encouraging me persistently.

Each article in this thesis was made possible with the help of my advisor, collaborators and colleagues. I wish to thank Dr. Vernon Cormier, Dr. Felipe Leyton, Dr. Peter Shearer and Kevin Seats for their contributions. I thank Dr. Xiaodong Song, Dr. Satoru Tanaka, Dr. Christine Thomas and several anonymous reviewers for their insightful and constructive comments of the manuscripts. The financial support of the PhD research work came from the graduate assistantship of Saint Louis University, NSF grants under contracts EAR-0229103, EAR-0229586, EAR-050537438 and EAR-0296078.

I would also like to take this opportunity to extend my gratitude to all the geoscience students. Thank you for your friendship and help to make my four years at SLU happy, en-

joyable and memorable. Special thanks to my dear friends and colleagues: Hongyi, Felipe, Ali, Michelle, Sabreen, Boston, Kevin, Oner, Hongfeng, Risheng, Young-Soo, Nathalie, Sebastiano and Safat. The help and friendship from many friends at University of Illinois were essential for me to get through the first year in the US, especially the help from Zhaohui, Xinlei, Fang, Jingyun, Ellen, Mo, and Hsiang-Hsin.

I want to thank all the staff in the Earth and Atmospheric Sciences Department at SLU. Bob Wurth and Eric Haug helped me to solve many computer-related issues. I thank them for their support during my four years' stay in the department. Those interesting and fun chats with Melanie in Maclewane Hall made my life more enjoyable.

At last, I would like to express my deepest gratitude to my husband, Chuntao Liang, for his love, caring, encouragement, support, and cheering me up ... I am deeply sorry for your 50,000 miles driving on highways during the completion of this thesis. No words can express how much I appreciate what you have done for me. Thank you, very much.

Table of Contents

List of Tables	vii
List of Figures	viii
CHAPTER 1: Introduction	1
CHAPTER 2: The Structure of the Base of the Outer Core Inferred from Seismic Waves Diffracted Around the Inner Core	6
2.1 Introduction	7
2.2 Assembly of PKP_{Cdiff} Waveform Database	10
2.3 Analysis of Differential Travel Times ($PKP_{Cdiff}-PKP_{DF}$)	13
2.3.1 Data Processing	13
2.3.2 Data Modeling	16
2.4 Analysis of Amplitude Ratios (PKP_{Cdiff}/PKP_{DF})	19
2.4.1 Data Processing	19
2.4.2 Data Modeling	21
2.5 Discussion	25
2.5.1 Hypothesis #1: A Rough ICB	26
2.5.2 Hypothesis #2: A Slurry Zone at the Base of the Outer Core	27
2.6 Conclusions	29
CHAPTER 3: Partial Melt in the Lowermost Mantle Near the Base of a Plume	32
3.1 Introduction	33
3.2 Data	35
3.3 Ray Parameter of PKP_{Cdiff} Coda	35

3.4	The Origin of the PKP_{Cdiff} Coda	41
3.5	Conclusions and Discussion	48
CHAPTER 4:	Using PKP Precursors Recorded at IMS Arrays to Determine the Small-scale Heterogeneity in the Mantle	50
4.1	Introduction	51
4.2	Data Processing	55
4.3	Modeling Global Average PKP Precursor Envelopes	60
4.4	Regional Variations of PKP Precursor Amplitude	70
4.5	Conclusions and Discussion	73
APPENDIX:	Copyright Permission	75
	References	77
	Vita Auctoris	90

List of Tables

Table 2.1: Events and seismic arrays used in this study	13
Table 4.1: IMS seismic arrays used and the number of events selected	56

List of Figures

Figure 2.1: P-wave velocity structure near the ICB	8
Figure 2.2: Ray path for PKP waves	9
Figure 2.3: An example of a vertical seismic record section	11
Figure 2.4: The great circle paths from earthquakes to arrays	12
Figure 2.5: Observed $PKP_{Cdiff} - PKP_{DF}$ differential times	17
Figure 2.6: Synthetic tests for factors affecting travel times	18
Figure 2.7: The best fitting model from the differential times	20
Figure 2.8: Observed amplitude ratios	22
Figure 2.9: Synthetic tests for amplitude ratios	24
Figure 3.1: Source-receiver geometry for the seismic data	36
Figure 3.2: Vertical component record section	37
Figure 3.3: Event 990302	38
Figure 3.4: Event 990305	39
Figure 3.5: Comparison of waveforms of the empirical source	41
Figure 3.6: Comparison between synthetic seismograms and data	42
Figure 3.7: Properties of the geometrical scattered waves	45
Figure 3.8: Trade-off between scattering volume	47
Figure 4.1: Ray paths and travel time curves for the core phases and precursors .	53
Figure 4.2: Geometry of IMS seismic arrays	57
Figure 4.3: Vertical record section of an example event and its sliding window slowness analysis	58
Figure 4.4: Average precursor amplitudes as a function of time and distance . .	61
Figure 4.5: Comparison of observed precursor and predicted precursor	63
Figure 4.6: Comparison of observed precursor and predicted precursor	65

Figure 4.7: Comparison of observed precursor and predicted precursor	66
Figure 4.8: Comparison of observed precursor and predicted precursor	67
Figure 4.9: Comparison of observed precursor and predicted precursor	68
Figure 4.10: Comparison of observed precursor and predicted precursor	69
Figure 4.11: The standard deviations of the globally averaged precursors' amplitudes	71
Figure 4.12: The geographical distribution of precursors	72

Chapter 1

Introduction

The Earth is a complex and quasi-spherical body with a radius of ~ 6371 km. Seismological studies during the last 100 years have revealed in great detail the 1-D radial Earth structure. The seismogram is the primary resource that scientists rely on to explore the structure of the Earth's deep interior. Although the basic theory needed to interpret the observations was well developed in the early 1800s, the development of seismic instrumentation was behind the theory, which prevented scientists from achieving breakthroughs in discovering the Earth's interior structure until 1900s. In 1900, Richard Oldham identified P , S , and surface waves from seismograms and discovered the Earth's liquid core a few years later based on the P -wave shadow zone (*Oldham, 1906*). Following Oldham's notice of the P -wave shadow zone, Gutenberg estimated the depth of the boundary between the mantle and the liquid core to be about 2900 km for the first time (*Gutenberg, 1913*), which is very close to the value of 2891 km, obtained from modern seismic data in the Preliminary Reference Earth Model (PREM) (*Dziewonski and Anderson, 1981*). In 1909, Andrija Mohorovičić unveiled the discontinuity between the lower density crust and the higher density mantle through his meticulous analyses of two sets of waves from one earthquake. In 1936, Inge Lehmann discovered a weak P wave in the shadow zone and hypothesized the existence of a solid inner core within the liquid core (*Lehmann, 1936*), which was confirmed by other scientists later (*Birch, 1940; Dziewonski and Gilbert, 1971*).

By the 1940s, the concept that the travel times of seismic arrivals can be used to infer the velocity structure of the Earth was well established and scientists agreed on the 1-D layered Earth structure (from the surface to the center are the crust, the mantle, the outer core and the inner core). The JB tables which contain the arrival times of seismic phases were published by Jeffreys and Bullen in 1940 and are still good reference today. Since then, the availability of more and more modern seismic data has led to rapid progress in

unveiling increasingly detailed structure of Earth's interior. In the 1960s, there was enough evidence to support the existence of seismic velocity discontinuities at depths of about 410 km and 660 km (e.g. *Niazi and Anderson, 1965; Johnson, 1967; Anderson, 1967*). The thickness and topography of the transition zone (the layer between the two discontinuities) are still under scrutiny (see *Shearer 2000* for a review). Now all modern 1-D reference Earth models, such as PREM, AK135 (*Kennett et al., 1995*), and IASP91 (*Kennett and Engdahl, 1991*), include those seismic discontinuities at only slightly different depths. In the mean time, more sophisticated imaging techniques have led to many interesting breakthroughs about the large-scale lateral heterogeneity inside the Earth. For instance, global tomography revealed the fate of subducted slabs and the origin of upwelling plumes (e.g. *Grand et al., 1997; van der Hilst et al., 1997; Montelli et al., 2004; Lei and Zhao, 2006*).

Most of the findings about the 1-D Earth structure so far have been achieved by analyzing the travel times and waveforms of the main seismic phases. The large-scale non-radial structures are mostly revealed by seismic tomography (both the traditional ray-theory tomography and the new finite-frequency tomography). The travel times and waveforms of main phases predicted by 1-D Earth models are still the most important tools to image the large-scale structure of the Earth. However, resolving the small-scale structure (with a scale of 5-10 km) is beyond the resolution of seismic tomography because of the spatial aliasing and contamination of waves scattered by the strong heterogeneities inside the Earth. High-frequency coda waves following *P* or *S* waves are direct evidence for small-scale random heterogeneity in the lithosphere. *Aki (1969)* first showed that the scattered coda waves, which used to be treated as noise, can be used to estimate the strength of the random heterogeneity. Observations of *PKP* precursors concluded that small-scale heterogeneity must also exist in the deep mantle (*Doornbos and Husebye, 1972; Cleary and Haddon, 1972*). More recently, small-scale heterogeneity inside the inner core has also been discovered by many different authors (e.g. *Vidale and Earle, 2000; Cormier and Li, 2002; Koper et al., 2004; Leyton and Koper, 2007*). In order to obtain a high-resolution image of the Earth's interior to better understand the nature of the small-scale heterogeneities and the dynamics of the whole Earth, we must put a great effort to the analysis of high-frequency scattered energy.

In this dissertation, I attempted to explore the interior structure of the Earth by analyzing the seismic core phases and their related scattered energy generated by small-scale heterogeneities inside the Earth, which may arrive before or after the main phases (coda waves or precursors). Guided by this intention, the dissertation is composed of four chapters. This chapter (Chapter 1) is an overview of the whole dissertation, which introduces previous related work and the motivations of my work. Each one of the following three chapters (Chapter 2 - Chapter 4) consists of an independent paper addressing different issues, thus having the complete structure of a standard journal paper. At the time of publication of the thesis, Chapter 3 has been published in *Geophysical Journal International* (see *Zou et al.*, 2007) with the corresponding copyright permission shown in the Appendix; Chapter 2 has been accepted for publication in *Journal of Geophysical Research*; while Chapter 4 is in preparation for submission to *Journal of Geophysical Research*.

The velocity structure of the inner core boundary (ICB) plays an important role for us to understand the chemical composition and dynamics of the core. The velocity gradient can be linked to the density gradient. The widely used reference Earth model PREM has a uniform composition throughout the outer core. However, some more recent models such as AK135 and PREM2 (*Song and Helmberger*, 1995) have a reduced velocity gradient at the base of the outer core, which implies some sort of chemical heterogeneity there. In Chapter 2, I followed the traditional seismological methods to examine the travel time and amplitude of PKP_{Cdiff} , which is the wave that diffracts around the inner core boundary (ICB), to infer the velocity structure at the base of the outer core. In the past, systematic study of PKP_{Cdiff} at distances greater than 154° was not conducted because this phase is only observable over a very limited range of source-receiver distances, has relatively small amplitude, and thus is difficult to observe. The proliferation of regional broadband arrays over the last decade has made the observations of PKP_{Cdiff} waves less difficult because closely-spaced seismic arrays allow small coherent phases to be identified and isolated, and slowness estimates can be made to verify the identity of prospective phases. By assembling a large, high-quality set of PKP_{Cdiff} waveforms from seismic arrays, I was able to constrain the velocity structure at the base of the outer core and then to learn about the chemistry and dynamics of the core.

As I examined PKP_{Cdiff} waves, I noticed strong coda waves following PKP_{Cdiff} for one of the events recorded at INDEPTH-III (International Deep Profiling of Tibet and the Himalayas Phase III) array. However, two other nearby events do not show these prominent coda waves. The scattered coda waves recorded at arrays are very useful to locate the scatterer in the deep Earth if we can carefully model their travel times, slownesses, and amplitudes. The PKP_{Cdiff} coda waves have been reported and investigated by several authors. For example, *Tanaka (2005)* presented characteristics of PKP_{Cdiff} coda waves from the small-aperture array short-period stations of the International Monitoring System. He observed a wide range of slownesses for the PKP_{Cdiff} coda waves, and interpreted the coda waves with slowness larger than 2 s/deg as scattering from the core-mantle boundary under the source side and receiver side, although an ICB origin could not be ruled out. In Chapter 3, I presented an analysis of a high-quality PKP_{Cdiff} record section recorded by a temporary array of broadband seismometers in Tibet from the INDEPTH-III experiment. I was able to model the differential travel times and slownesses relative to PKP_{DF} , and envelopes of the coda using single-scattering theory to locate the anomalous region and obtain its velocity perturbation.

The scattered energy generally arrives after the main phase as coda, however, the special velocity structure at the CMB can cause the scattered energy from the heterogeneities in the mantle to arrive before the main phase $PKIP$ as precursors. This type of scattered energy preceding PKP was first observed in 1934 (*Gutenberg and Richter, 1934*). Previous studies of the PKP precursors had controversy about their origin, including refraction in the inner core (*Gutenberg, 1957*), refraction or reflection in a transition layer between the outer and inner cores (*Bolt, 1962; Sacks and Saa, 1969*), and diffraction from the CMB (*Bullen and Burke-Gaffney, 1958*). It is now widely accepted that PKP precursors are generated by the scattering from volumetric inhomogeneities near the CMB or within the lower mantle, or from CMB topography (*Doornbos and Husebye, 1972; Cleary and Haddon, 1972; Bataille et al., 1990*). However, the radial and lateral distributions, as well as the magnitude of the small-scale mantle heterogeneity are still not well resolved. Modeling of global average precursors tends to favor a whole mantle scattering model instead of confining the heterogeneity near the CMB. However, the magnitude of P -wave velocity per-

turbation among different studies varies by a factor of ten. The discrepancy come from two possible causes. One is related to the data used in different studies. Due to uneven data sampling and different data processing schemes, different authors may obtain different global average PKP precursor envelopes. The other possible reason may be related to differences in forward modeling methods. For the same precursors, the single-scattering theory may yield different magnitudes of heterogeneity from a multiple-scattering or diffusion-based theory. In Chapter 4, I assembled a large, geographically diverse dataset of PKP precursor envelopes by using the globally distributed International Monitoring System (IMS) seismic arrays. An advantage of using arrays over single stations is that the recordings of all elements at one array can be coherently stacked to suppress noise, and thus obtain high signal-to-noise (SNR) ratio PKP precursors, even for relatively small earthquakes. I then used a type of Monte-Carlo seismic phonon method to model the globally averaged PKP precursor envelopes to learn about the small-scale heterogeneities in the mantle, which may provide some insights about mantle dynamics.

Chapter 2

The Structure of the Base of the Outer Core Inferred from Seismic Waves Diffracted Around the Inner Core

We systematically searched for seismograms of waves diffracted around the inner core (PKP_{Cdiff}) from all the temporary seismic arrays with data currently available at the IRIS DMC, as well as some permanent regional seismic arrays including F-NET in Japan and GRF in Germany, to assemble the largest high-quality PKP_{Cdiff} database ever created. PKP_{Cdiff} waves preferentially sample the base of the outer core and so contain important clues about Earth structure in this region. We measured $PKP_{DF} - PKP_{Cdiff}$ differential travel times and PKP_{Cdiff}/PKP_{DF} amplitude ratios in the distance range of $154^\circ - 160^\circ$ and modeled the observations using grid searches and full wave theory synthetic seismograms. The optimum model found by fitting the differential travel times has relatively low velocity at the base of the outer core as in AK135, which is consistent with many previous travel time studies. However, the optimum model found by fitting the amplitude ratios (PKP_{Cdiff}/PKP_{DF}) does not exhibit this feature, and instead is closer to PREM. The discrepancy may be explained by two likely causes. One is that small-scale topography or roughness on the ICB tends to scatter energy away from PKP_{Cdiff} waves by generating trailing coda waves. The other is that there exists a thin layer with relatively low Q at the base of the outer core. This might be expected if there are suspended solid particles at the base of the outer core, as proposed decades ago. Both mechanisms could generate smaller PKP_{Cdiff} amplitudes without significantly affecting PKP_{Cdiff} travel times.

2.1 Introduction

A large number of seismological studies have suggested that the region just above the inner core boundary (ICB) is distinct from the rest of the outer core. The layer about 400 km above the ICB was originally termed the F-layer and was characterized by a strong low velocity zone (*Jeffreys, 1939*). Later Earth models, constructed with more accurate travel time data, instead defined this as a region of increased velocity, and often included one or more first order discontinuities above the ICB (*Bolt, 1962, 1964; Adams and Randall, 1964; Sacks and Saa, 1969*). Ultimately though, these model types were also discarded, as PKP precursors were reinterpreted as energy scattered from mantle heterogeneities near the core mantle boundary (CMB) (*Doornbos and Husebye, 1972; Cleary and Haddon, 1972; Haddon and Cleary, 1974*). Hence, modern reference Earth models universally have smoothly increasing velocities at the base of the outer core.

There is still some uncertainty, however, about the steepness of the velocity gradient at the base of the outer core. This is important because the velocity gradient strongly constrains the density gradient in the Earth's core. If we assume the pressure derivative of the bulk modulus is constant (~ 3.5) in the outer core (*Anderson and Ahrens, 1994*), then the Bullen parameter η (*Bullen, 1963*), which is the ratio between the actual density gradient and the gradient corresponding to uniform composition, only depends on the velocity gradient. The widely used reference Earth model PREM (*Dziewonski and Anderson, 1981*) has the Bullen parameter $\eta \sim 1$ through the outer core, which implies a homogeneous, adiabatic medium.

More recent reference Earth models, such as PREM2 (*Song and Helmberger, 1995*) and AK135 (*Kennett et al., 1995*), have significantly lower velocity gradients at the base of the outer core, corresponding to Bullen parameters significantly higher than 1 (Figure 2.1). In other words, these models imply that near the base of the outer core density increases too quickly to be explained solely by compression, and some sort of change in chemistry or phase must occur. Interestingly, core dynamical studies suggested a slurry layer occupied by free-floating broken dendrites just above the ICB several decades ago (*Loper and Roberts, 1978; Loper, 1978; Loper and Roberts, 1981*). However, more recent studies con-

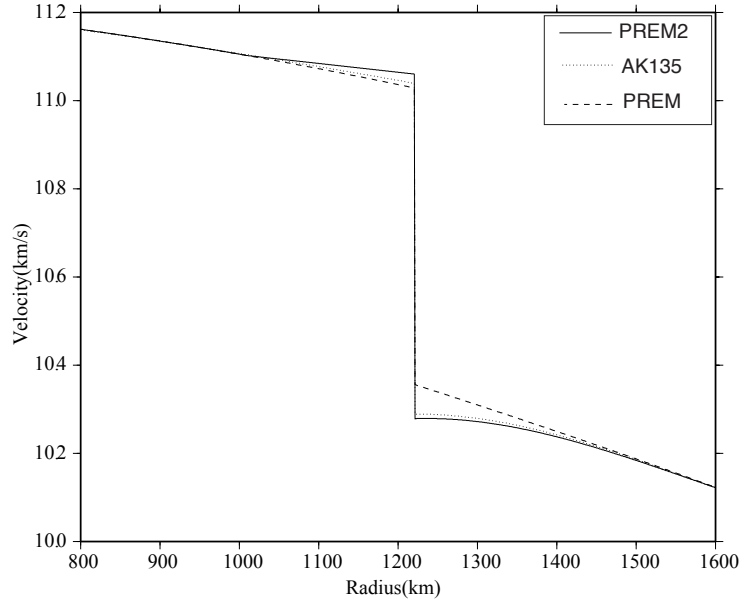


Figure 2.1: P-wave velocity structure near the ICB. The radius of ICB in AK135 is shifted to be the same as PREM and PREM2. Dashed curve is for PREM, solid one is for PREM2 and dotted curve is for AK135. AK135 is nearly identical to PREM2 at the base of the outer core.

sider a slurry of suspended particles unlikely to exist in the Earth and instead suggest that a thin mushy zone is more probable (*Bergman, 2003; Shimizu et al., 2005*).

But not all seismic studies support a relatively low velocity gradient at the base of the outer core. *Choy and Cormier (1983)* found that KOR5 predicts too large PKP_{Cdiff} amplitudes compared to the observations and ruled out the low velocity gradient zone above the ICB, which is consistent with their previous results (*Rial and Cormier, 1980; Cormier, 1981*). Both *Huang (1996)* and *Kaneshima et al. (1994)* investigated the ICB velocity structure beneath North America's Pacific seashore and they obtained a slightly smaller P-wave velocity than that in PREM, but significantly larger than that in AK135 at the base of the outer core. Most recently *Yu et al. (2005)* re-examined the outer core velocity structure by analyzing differential travel times, amplitude ratios and waveforms of various PKP waves recorded at Global Seismograph Network (GSN) and several regional networks and they found out that the velocity structure at the base of the outer core exhibited a strong hemispherical difference. The data sampling the quasi-eastern hemisphere ($40^{\circ}\text{W}-180^{\circ}\text{E}$) can be explained by a PREM-type outer core velocity structure, while those sampling the

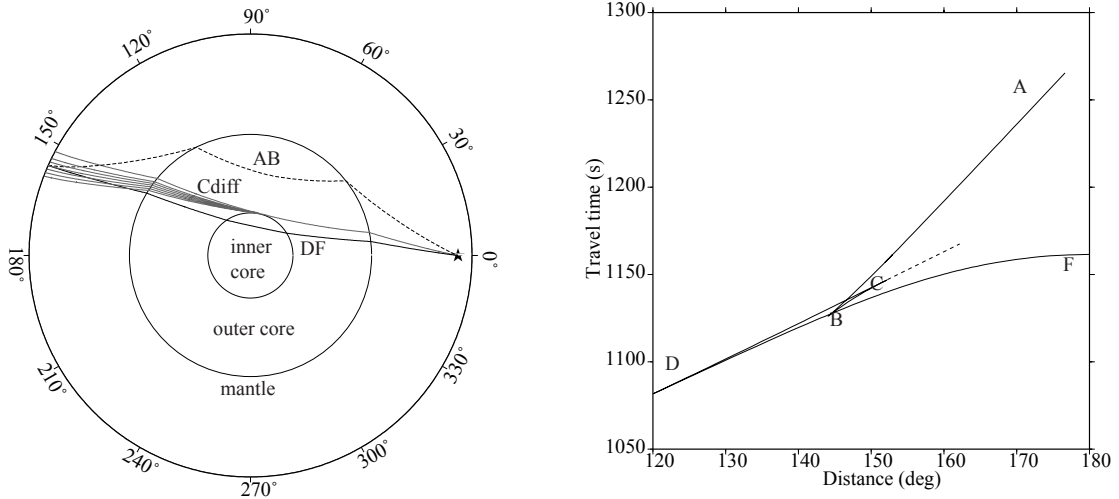


Figure 2.2: **(Left)** Ray path for PKP waves at the C-cusp for an event at 400 km depth. Black curve represents the ray path of PKP_{DF} at a distance of 156° . Gray curves indicate the ray paths of PKP waves diffracted along the ICB. **(Right)** Standard travel time curve for PKP waves in PREM. The dashed line indicates propagation of PKP_{Cdiff} .

quasi-western hemisphere (180°W - 40°E) can be best explained by their preferred model OW, which has velocity closer to PREM2 than PREM at the base of the outer core.

In this study, we focus on studying the structure of the base of the outer core by analyzing PKP_{Cdiff} waves, which are waves diffracted around the ICB and are more sensitive to the base of the outer core than any other phase. Although ray theory predicts zero amplitude after the C-cusp (Figure 2.2), which occurs at a distance of $\sim 152.5^\circ$ in PREM or $\sim 155.5^\circ$ in AK135 for a source at 100 km depth, both theoretical calculations (Cormier and Richards, 1977; Cormier, 1981) and observations (Huang, 1996) indicate that PKP_{Cdiff} has significant energy for several degrees into the inner core shadow zone. At these distances the amplitude decay of PKP_{Cdiff} is mainly controlled by diffraction and is extremely sensitive to the velocity gradient just above the ICB and the period of PKP_{Cdiff} .

Systematic study of PKP_{Cdiff} at distances greater than 154° has been somewhat neglected because it is difficult to observe. Small earthquakes do not generate PKP_{Cdiff} waves large enough to be observed above the background noise, and large earthquakes usually have long source durations, which makes PKP_{DF} interfere with PKP_{Cdiff} (the time separation between them is less than 10 s). Similarly, shallow earthquakes sometimes

generate PKP_{DF} depth phases that interfere with PKP_{Cdiff} , though with careful modeling of the source time functions this problem can often be overcome.

The proliferation of regional broadband arrays over the last decade has made the observations of PKP_{Cdiff} waves less difficult, and has enabled us to assemble a large, high-quality set of PKP_{Cdiff} waveforms. In order to reduce shallow structure effects, we use PKP_{DF} as a reference phase since it has a ray path very similar to PKP_{Cdiff} in the crust and mantle. Although the top of the inner core always has an effect on the travel time and amplitude of PKP_{DF} , our synthetic tests show that this effect is small compared with the effect of the base of the outer core on PKP_{Cdiff} . Therefore, the differential travel times and amplitude ratios between PKP_{DF} and PKP_{Cdiff} measured from the high-quality record sections provide an excellent opportunity to explore the structure at the base of the outer core.

2.2 Assembly of PKP_{Cdiff} Waveform Database

Because PKP_{Cdiff} is only observable over a very limited range of source-receiver distances and has relatively small amplitude, a closely-spaced seismic array is important to identify the phase and to generate a high-quality PKP_{Cdiff} data set. An array allows small coherent phases to be identified and isolated, and slowness estimates can be made to verify the identity of prospective phases. Another advantage is that the differential travel times ($PKP_{Cdiff} - PKP_{DF}$) can be measured more accurately by cross-correlating waveforms in the PKP_{Cdiff} time window and the PKP_{DF} time window respectively, instead of cross-correlating the PKP_{Cdiff} window with the PKP_{DF} window for a single station. This is especially important because diffracted waves undergo some shape change as they arrive at larger distances, and so they have shapes dissimilar with PKP_{DF} .

We systematically examined the waveforms of earthquakes with depth greater than 60 km and magnitude greater than 5.5 M_w from all the temporary PASSCAL networks with data open to public researchers at the IRIS DMC, as well as some permanent regional seismic arrays such as F-NET (Full Range Seismograph Network of Japan) and GRF (Gräfenberg) array in Germany. Deep earthquakes have relatively short source durations,

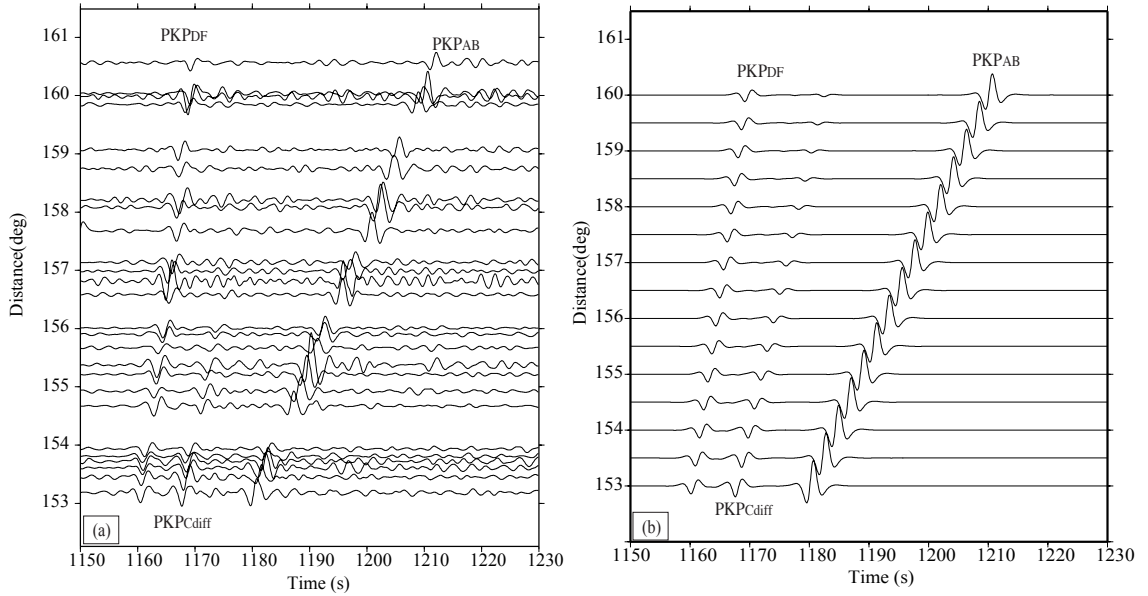


Figure 2.3: **(a)** An example of a vertical-component seismic record section which shows good PKP_{DF} and PKP_{Cdiff} waveforms from an event recorded at the F-net array with a magnitude of 6.1 Mw and a depth of 274 km (Event No. 4 in Table 2.1). Seismograms are filtered around 3 s using band-pass filtering. **(b)** The corresponding synthetic seismograms computed from full-wave theory method for an explosivesource at a depth of 274 km based on the PREM model.

which enables us to separate PKP_{DF} and PKP_{Cdiff} more easily since the differential time between these two phases is about 10 s. And deep sources avoid the potential interference of the depth phase $pPKP_{DF}$ with PKP_{Cdiff} .

All the record sections in the distance range $154^\circ - 160^\circ$ were checked visually for quality. We picked those events that have high signal-to-noise ratios (SNRs) records and show clear PKP_{DF} and PKP_{Cdiff} phases (Figure 2.3). The amplitudes of PKP_{Cdiff} waves decay with distance and are almost at the noise level after a few degrees. In our data selection criteria, we choose all the traces with high SNRs after 154° until the one at which the PKP_{Cdiff} phase is no longer identifiable. We discuss the possible bias caused by choosing only the “best” data in a later section of this manuscript.

As expected, the PKP_{Cdiff} waves are very difficult to observe. We examined 111 record sections from F-net, 110 record sections from GRF, and more than 300 record sections from the temporary networks at IRIS DMC in the distance range $154^\circ - 160^\circ$. The

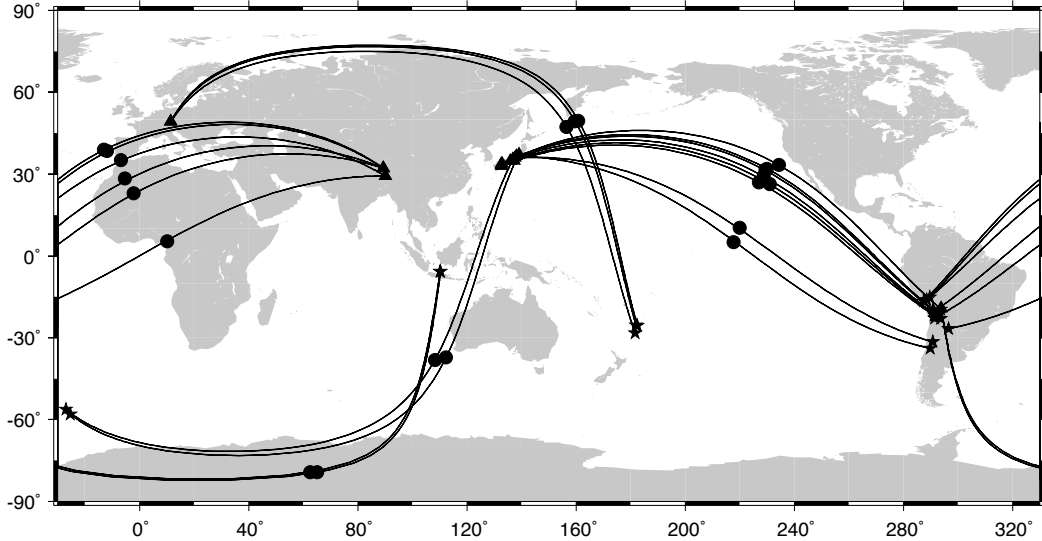


Figure 2.4: The great circle paths from earthquakes to corresponding seismic arrays for high-quality PKP_{DF} and PKP_{Cdiff} waveforms. The triangles are seismic arrays, the stars are earthquake locations, and the black circles indicate the turning point of PKP_{DF} in the inner core.

total number of seismograms inspected was about 11,000. We obtained only 21 record sections, corresponding to 370 individual seismograms, which show high-quality PKP_{Cdiff} waves. Table 2.1 lists all the events and the corresponding seismic arrays used in this study. Among the 21 events in Table 1, 10 events were recorded at F-NET, 3 events were recorded at GRF, 2 events were recorded by the BANJO/SEDA (Broadband Andean Joint and Seismic Exploration of the Deep Altiplano) experiment, 2 events were recorded from INDEPTH-II (International Deep Profiling of Tibet and Himalayas, Phase II) experiment and 4 events were recorded by the INDEPTH-III experiment. Due to the small number of high quality seismograms, the geographical sampling of the core by the PKP_{Cdiff} data set is limited (Figure 2.4). Most of our data sample the quasi-western hemisphere (180°W-40°E) with limited sampling points in the quasi-eastern hemisphere (40°E-180°E).

Table 2.1: Events and seismic arrays used in this study

Event ID	EventTime (yr/mon/day/hr:min)	Lat (°N)	Lon (°E)	Depth (km)	Mag (Mw)	Array ^a Code	# ^b	ϕ^c (°)
1	1997/07/20/10:14	-22.98	-66.30	256	6.1	FN	12	60
2	1999/11/21/03:51	-21.75	-68.78	101	5.8	FN	8	62
3	2000/06/16/07:55	-33.88	-70.09	120	6.4	FN	22	54
4	2001/06/29/18:35	-19.52	-66.25	274	6.1	FN	23	62
5	2002/09/24/03:57	-31.52	-69.20	119	6.2	FN	32	55
6	2003/09/17/21:34	-21.47	-68.32	127	5.7	FN	14	62
7	2004/09/11/21:52	-57.98	-25.34	64	6.1	FN	24	43
8	2005/06/12/19:26	-56.28	-26.98	95	6.0	FN	26	44
9	2005/06/13/22:44	-19.90	-69.13	111	7.7	FN	26	63
10	2005/08/14/02:39	-19.74	-69.02	83	5.8	FN	12	63
11	1994/06/16/18:41	-15.18	-70.34	225	5.9	DII	9	67
12	1994/08/19/10:02	-26.65	-63.38	565	6.4	DII	8	61
13	1994/09/28/17:33	-5.72	110.38	634	6.0	BS	18	83
14	1994/11/15/20:18	-5.61	110.20	559	6.5	BS	14	83
15	1998/10/08/04:51	-16.12	-71.40	136	6.1	DIII	27	66
16	1999/03/02/17:45	-22.72	-68.50	110	5.9	DIII	27	62
17	1999/03/05/00:33	-20.42	-68.90	110	5.8	DIII	27	63
18	1999/04/03/06:17	-16.66	-72.66	87	6.8	DIII	30	64
19	1995/10/14/08:00	-25.57	-177.51	70	6.2	GRF	13	52
20	1997/04/12/09:21	-28.17	-178.37	184	5.9	GRF	13	51
21	2001/03/11/00:50	-25.37	-177.97	231	5.8	GRF	13	53

^a For the array code, FN stands for F-net, DII stands for INDEPTH-II, DIII stands for INDEPTH-III, BS stands for BANJO/SEDA, and GRF stands for Gräfenberg.

^b # is the number of seismograms used in the record section.

^c ϕ is the angle of the turning direction of PKP_{DF} in the inner core with respect to the Earth's rotation axis.

2.3 Analysis of Differential Travel Times ($PKP_{Cdiff} - PKP_{DF}$)

2.3.1 Data Processing

Differential $PKP_{Cdiff} - PKP_{DF}$ travel times from our data set are measured as follows. First for each record section, we filter velocity seismograms with a 3-pole Butterworth bandpass filter around 3 s with a one octave band. Although in theory filtering the seismograms at different frequency bands can provide us a separate constraint about the

velocity structure at the base of the outer core, unfortunately, we found that it is difficult to get accurate measurements of $PKP_{Cdiff} - PKP_{DF}$ travel times at higher or lower frequencies. At longer periods, the short time interval between PKP_{DF} and PKP_{Cdiff} makes them interfere with each other (*Souriau and Roudil, 1995*). At higher frequencies, noise and complicated waveforms prohibit cross-correlation from working properly to get accurate travel time estimates. Around 3 s, PKP_{Cdiff} and PKP_{DF} are well separated, and we can obtain the most accurate measurements for the differential times and the amplitude ratios.

After filtering, we use the multichannel cross-correlation method (mccc) (*van Decar and Crosson, 1990*) to align the record section within the PKP_{DF} time window to get relative time shifts. Then we stack the aligned record section to get the time of the peak amplitude. By using those relative time shifts and the time of the peak amplitude, we can get the arrival times of PKP_{DF} as described in *van Decar and Crosson (1990)*. Repeating the same procedure for PKP_{Cdiff} , we get the travel time of PKP_{Cdiff} and then the differential times $PKP_{Cdiff} - PKP_{DF}$. The differential times measured by the mccc method were compared with those obtained with the adaptive stacking technique (*Rawlinson and Kennett, 2004*), which was proposed specifically for aligning waveforms with somewhat dissimilar shapes. The methods give almost identical results for the $PKP_{Cdiff}-PKP_{DF}$ differential times. For each record section, we also invert the arrival times yielded by mccc for the slowness and back azimuth of PKP_{DF} and PKP_{Cdiff} phases. We find that they are generally very close to the predicted values in AK135 for most of the events, which ensures that we are indeed analysing the proper phases. For a few events the deviations are somewhat big, but in these cases the standard errors are also large because of poor source-receiver geometry. As an example, we have poor backazimuth resolution for some events recorded at INDEPTH-III because the strike of the array matches the expected backazimuth (see Figure 1 of *Zou et al. (2007)*).

We apply this same method to predict $PKP_{Cdiff} - PKP_{DF}$ differential times for arbitrary velocity models using synthetic seismograms calculated with the full-wave theory technique (*Cormier and Richards, 1977*). This method works with spherically symmetric, anelastic Earth models parametrized as polynomial functions of normalized radius. Full-

wave theory correctly accounts for the diffraction and tunnelling of body waves at and near the grazing incidence to a boundary by incorporating the Langer approximation (*Cormier and Richards, 1988*). This technique is computationally fast and because it operates in spherical geometry it avoids the earth-flattening approximation. It has shown good agreement with the reflectivity method (*Choy et al., 1980*) and the generalized ray method (*Song and Helmberger, 1992*) for generating synthetic core phases. An example record section is shown in Figure 2.3. We compared full wave theory synthetics to those calculated using a frequency-wavenumber (fk) integration method (*Zhu and Rivera, 2002; Herrmann and Mandal, 1986*) and found slightly different results; however, the fk synthetics contained some artifacts that were presumably related to layering in a flattened Earth model.

Our observed $PKP_{Cdiff} - PKP_{DF}$ differential travel times are plotted relative to PREM in Figure 2.5. The effect of different source depth is accounted for as follows. For each event's depth and distance, we find the PKP_{DF} ray parameter predicted by PREM. For that ray parameter, we find the corresponding distance for an event at 100 km depth, which is the distance plotted in Figure 2.5. All the synthetics are computed with a source depth at 100 km. Although the data are somewhat scattered, it appears that AK135 fits the data better than PREM. We use a statistical method called an F -test (*Menke, 1989*) to verify this quantitatively. First, we calculate the variances of the misfits between the data and the predicted values from the two models, which are 0.1524 for AK135 and 0.2117 for PREM, respectively. The F value is then formed from the ratio of the two variances, which is 1.3891. Using an F -calculator (<http://faculty.vassar.edu/lowry/tabs.html>), we find that there is only a 0.16% probability that the two models are equal, which implies that AK135 is better than PREM at a 99.8% probability in terms of fitting the data. However, we do not observe obvious quasi-hemispherical differences in the data as seen for instance by *Yu and Wen (2006)*. Although the average differential travel time residual for the eastern hemisphere (crosses in Figure 2.5) is a little bigger than for the western hemisphere (gray dots in Figure 2.5), the scattering ranges of the data overlap. The reason for the lack of a clear hemispherical signal may be that our data set is limited in the eastern hemisphere, or because the hemispherical pattern of the inner core velocity observed by some studies (*Niu and Wen, 2001a; Wen and Niu, 2002; Garcia, 2002; Stroujkova and Cormier, 2004; Yu*

et al., 2005; *Yu and Wen*, 2006) disappears at larger distances (such as the range considered here) as reported by other authors (*Garcia et al.*, 2006; *Garcia*, 2002; *Cao and Romanowicz*, 2004). This would be expected if the quasi-hemispherical pattern in the inner core exists only to relatively shallow depths beneath the ICB.

2.3.2 Data Modeling

In modeling the travel time data we only vary the velocity structure at the base of the outer core and fix the velocity in the remainder of the Earth according to PREM. There are several reasons why this type of limited parametrization is justified. First, because the ray paths of PKP_{DF} and PKP_{Cdiff} are very close in the crust and most of the mantle, the differential times can be attributed mainly to the velocity structure in the lower outer core and at most the upper 500 km of the inner core. For our distance range of $154^\circ - 160^\circ$ the reference phase PKP_{DF} turns at 300-500 km below the ICB, while PKP_{Cdiff} has maximum sensitivity just above the ICB. Second, the difference in inner core and the lowermost mantle velocity structure between standard reference models has very small effects on $PKP_{Cdiff} - PKP_{DF}$ differential times, while the difference in the velocity at the base of outer core between standard reference models has a large effect (Figure 2.6). Third, we note that the angle of PKP_{DF} with respect to Earth's rotation axis for all our data is greater than 45° (Table 2.1). Based on the reported inner core anisotropy models (e.g. *Creager*, 1992; *Shearer*, 1994; *Vinnik et al.*, 1994; *Song and Richards*, 1996), the travel time difference of PKP_{DF} caused by anisotropy is very small (less than 0.2 s). So the observed differential times $PKP_{Cdiff} - PKP_{DF}$ would not be affected significantly by inner core anisotropy. Fourth, we do not observe a strong quasi-hemispherical signal in the data, and so separate modeling for each hemisphere is not warranted.

Among velocity models at the base of the outer core reported by different studies (e.g. *Qamar*, 1973; *Dziewonski and Anderson*, 1981; *Choy and Cormier*, 1983; *Souriau and Poupinet*, 1991; *Song and Helmberger*, 1995; *Kennett et al.*, 1995; *Yu et al.*, 2005), the main difference is the structure of the velocity and its gradient at the bottom 400 km (or less) of the outer core. In PREM (*Dziewonski and Anderson*, 1981), the velocity increases with a

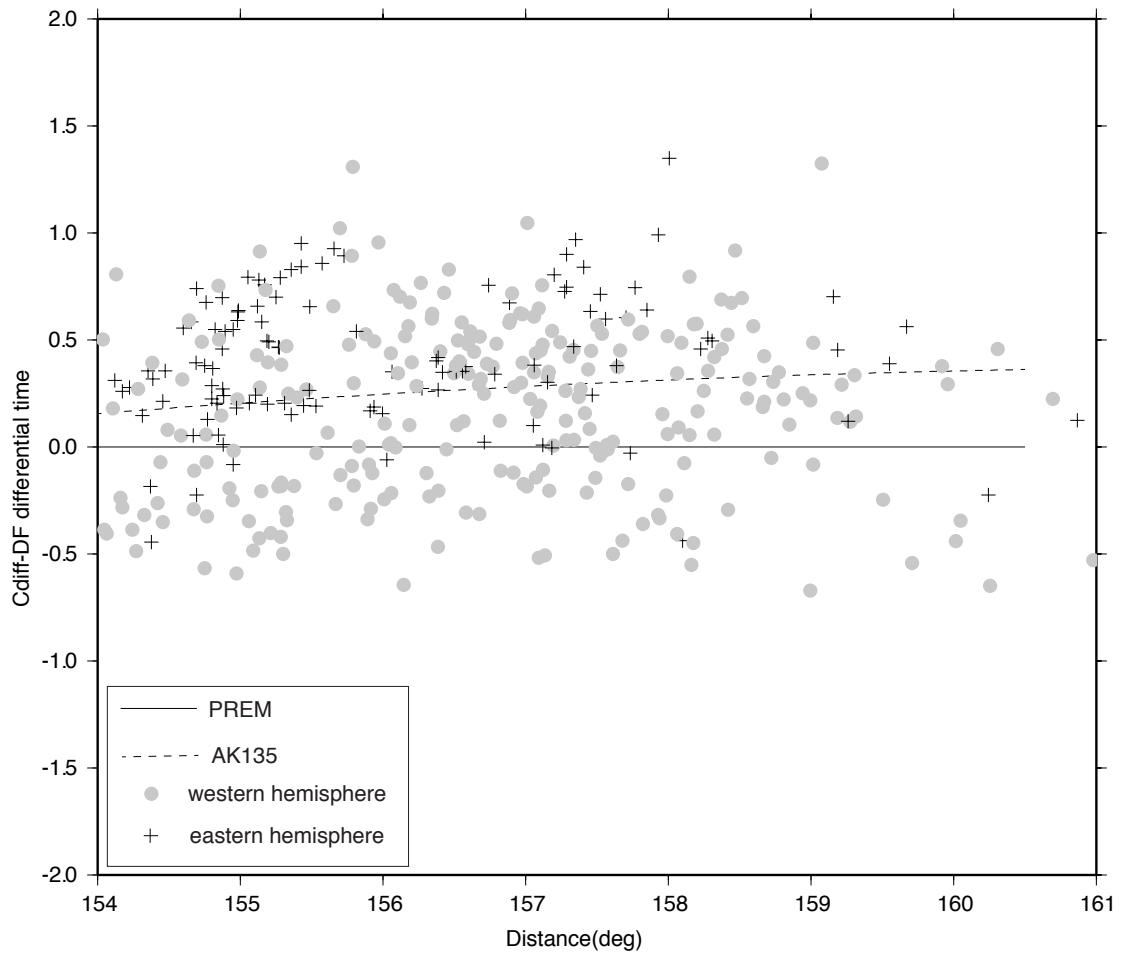


Figure 2.5: Observed $PKP_{Cdiff} - PKP_{DF}$ differential travel times relative to PREM. The solid line is for PREM, which is zero since it is used as a reference. The dashed line represents predicted differential times of AK135 relative PREM. The pluses are for the data sampling the eastern hemisphere, and the gray circles are for the data sampling the western hemisphere.

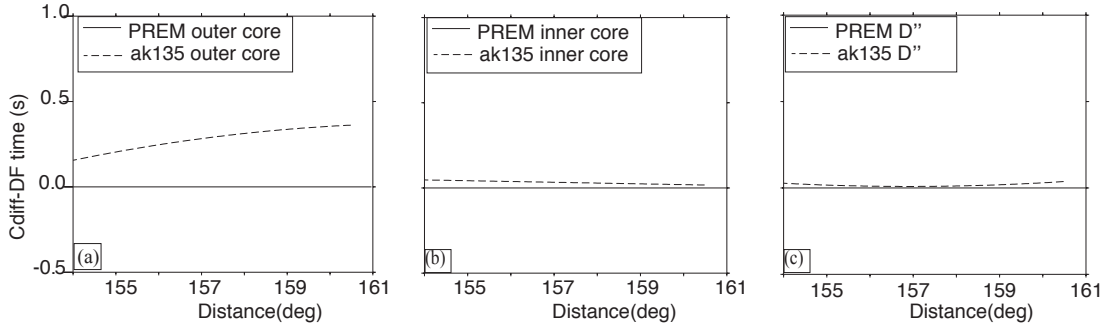


Figure 2.6: **(a)** The difference in the differential times caused by the velocity difference at the base of the outer core between PREM and AK135. **(b)** The difference in the differential times caused by the velocity difference in the inner core between PREM and AK135. **(c)** The difference in the differential times caused by the velocity difference in the lowermost mantle. In all three panels, the solid line is for PREM, and the dashed line is for AK135.

nearly constant gradient around $0.6 \times 10^{-3} s^{-1}$. In PREM2 (*Song and Helmberger, 1995*) and AK135 (*Kennett et al., 1995*), the velocity gradient decreases from about $0.6 \times 10^{-3} s^{-1}$ at 400 km above the ICB to nearly zero at the ICB, and the velocity profile with depth is more flat than that in PREM. Therefore, we choose 400 km above the ICB as the minimum “pinning depth” at which the models we evaluate are constrained to agree with PREM in value and gradient.

We use a systematic grid search to find a model that best fits the data. We let the pinning depth start at 400 km above the ICB and increase it in 50 km intervals until it is 50 km above the ICB. For each pinning depth, we keep the velocity and its gradient the same as in PREM, and let the gradient decrease linearly with different slopes to satisfy the velocity gradient at the ICB between $0.6 \times 10^{-3} s^{-1}$ (the value in PREM) and zero (the value in AK135) with an increment of $0.01 \times 10^{-3} s^{-1}$. We use 2nd-order polynomials (3 polynomial coefficients) to describe the velocity structure and have two constraints at the pinning depth and one constraint at the ICB. Therefore, we have exact analytical solutions for the polynomial coefficients. In this way, we generate 488 different velocity models at the base of the outer core (8 different pinning depth \times 61 different slopes of the gradient for each different pinning depth).

For each trial velocity model, we compute the synthetic seismograms and get the differential times ($PKP_{Cdiff} - PKP_{DF}$) with the method described above. Using an L2 norm

misfit function between the synthetics and the data, we find a best fitting model that is very close to AK135 (Figure 2.7). This is consistent with the results of *Garcia et al.* (2006) who worked with a much larger data set of PKP arrivals at different distances. The uncertainty of our results is estimated using a bootstrap resampling algorithm (*Tichelaar and Ruff*, 1989), which randomly resamples the data with replacement to generate a pseudo-dataset with the same number of elements as the true dataset. An optimal solution is obtained by fitting the pseudo-dataset. By repeating the procedure 200 times, we obtain a population of best fitting models and therefore the mean and standard deviation can be estimated (Figure 2.7).

2.4 Analysis of Amplitude Ratios (PKP_{Cdiff}/PKP_{DF})

PKP_{Cdiff} amplitudes are very sensitive to the velocity gradient at the bottom of the outer core, just as P_{diff} amplitudes are very sensitive to the gradient at the base of the mantle (*Alexander and Phinney*, 1966; *Phinney and Alexander*, 1966; *Valenzuela and Wyss*, 1998). Different velocity gradients focus or defocus the seismic energy in different ways. A larger positive gradient bends energy back towards the surface, causing smaller amplitudes of the diffracted waves; a negative or smaller positive gradient traps more energy near the ICB, thus causing larger amplitude of the diffracted wave into the shadow zone.

2.4.1 Data Processing

Similar to the travel time analyses, in order to mitigate the effects of shallow structure on PKP_{Cdiff} amplitude, we use the amplitude ratios between PKP_{Cdiff} and PKP_{DF} to constrain the velocity structure at the base of the outer core. The procedure we use to obtain the amplitude ratios is similar to the one used to get the differential times. We measure the peak-to-peak amplitudes from the filtered seismograms for both PKP_{DF} and PKP_{Cdiff} . Synthetic amplitude ratios are obtained in the same way from the synthetic seismograms computed with full-wave theory for an explosive source. In order to compare the observed amplitude ratios with the synthetic ones, we apply the source corrections to the data by

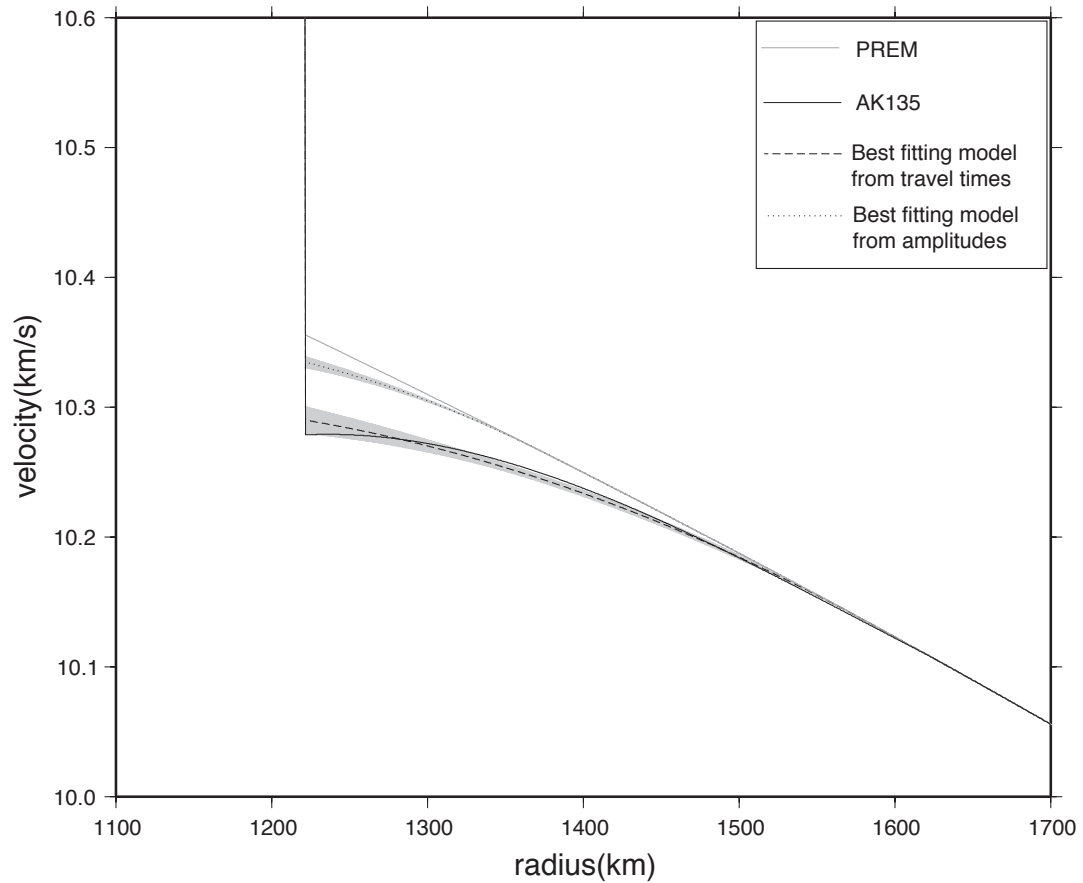


Figure 2.7: The best fitting model from the differential times ($PKP_{Cdiff} - PKP_{DF}$) and from the amplitude ratios (PKP_{Cdiff}/PKP_{DF}). The top gray curve is for PREM, the bottom black curve is for AK135, the black dashed curve with gray shaded region is the best fitting model with one standard deviation from the differential times, and the dotted black curve with gray shaded region is our best fitting model with one standard deviation from the amplitude ratios with inner core $Q=400$ discussed in Section 4.2.

using radiation coefficients of PKP_{DF} and PKP_{Cdiff} according to the Harvard CMT focal mechanism. Since the take-off angles of PKP_{DF} and PKP_{Cdiff} are very close, the corrections are quite small. The distance of each measurement is adjusted for focal depth using the same approach as in the travel time analysis. The corrected measurements are presented in Figure 2.8. The observed amplitude ratios do not exhibit clear hemispherical differences, which is consistent with the amplitude observations of *Yu and Wen* (2006) (see their Figure 5), as well as the travel time observations presented here (Figure 2.5). However, the amplitude ratios observed by *Souriau and Roudil* (1995) (see their Figure 8) are consistently larger than our data. They also filtered the seismograms around 3 s to get the measurements, and so the differences must be due to different Earth sampling or data quality. One possibility for the discrepancy is that by using arrays to identify PKP_{Cdiff} waves we are able to confidently include smaller phases, while the data set of *Souriau and Roudil* (1995) only includes phases that were large enough to be confidently identified on individual seismograms.

2.4.2 Data Modeling

Before we evaluate the different trial models, we perform sensitivity tests to see what Earth properties most affect PKP_{Cdiff}/PKP_{DF} amplitude ratios. As expected, we find that the difference in the inner core and the lowermost mantle velocity between different reference models does not affect the amplitude ratios significantly, but that the difference in the velocity at the base of the outer core has a very prominent effect on the amplitude ratios (Figure 2.9). A smaller velocity gradient at the bottom of the outer core tends to generate larger PKP_{Cdiff} amplitudes, thus larger amplitude ratios (PKP_{Cdiff}/PKP_{DF}). Therefore, AK135 predicts much larger PKP_{Cdiff}/PKP_{DF} amplitude ratios than PREM. We also confirmed that the difference in the velocity at the base of the outer core between PREM and AK135 has nearly no effect on the PKP_{DF} amplitude. Thus the large amplitude ratios from AK135 are totally due to the large PKP_{Cdiff} amplitudes. Unlike the differential travel times, however, the effect of inner core P-wave attenuation (Q) on amplitude ratios is not negligible (Figure 2.9c). Smaller Q in the inner core decreases the PKP_{DF}

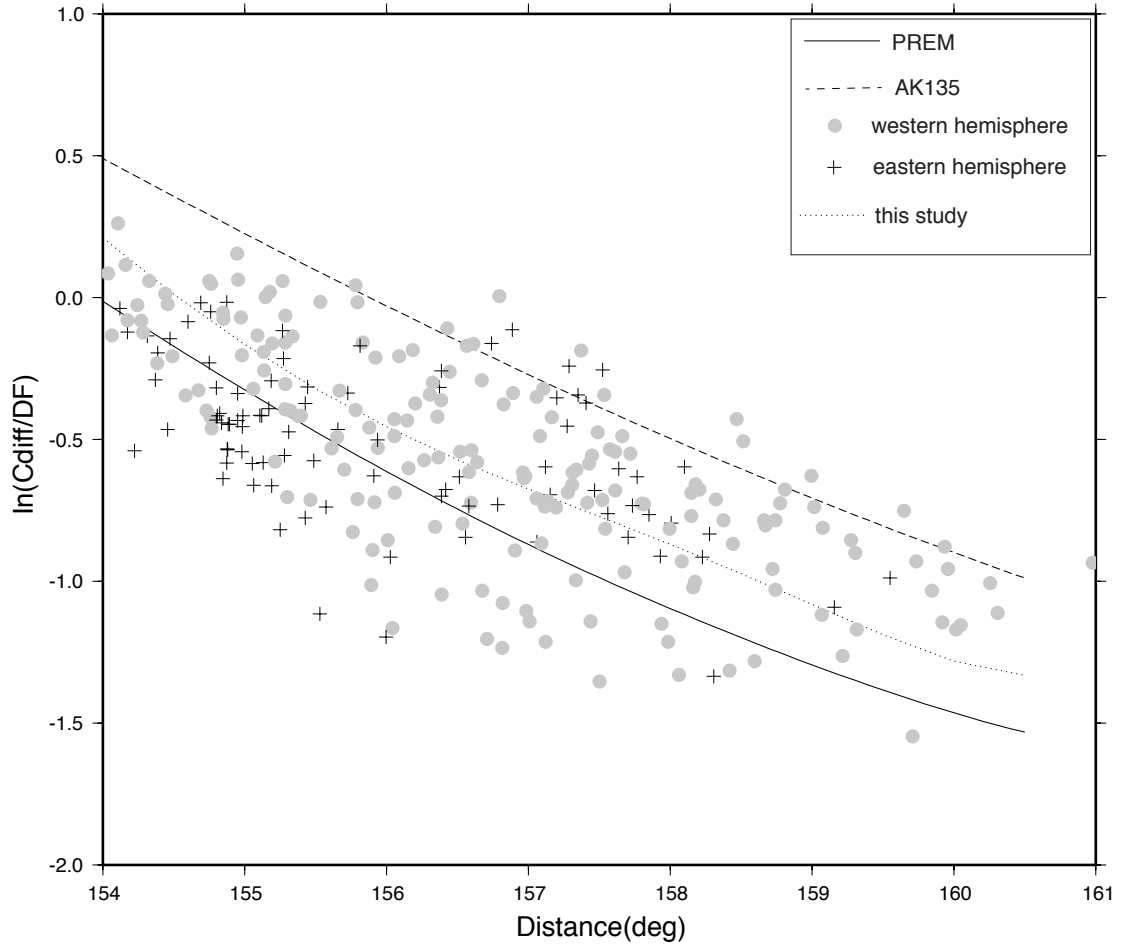


Figure 2.8: Observed amplitude ratios of $(PKP_{C_{diff}}/PKP_{DF})$. The solid curve is the predicted amplitude ratios from PREM and the dashed curve is for AK135. The pluses are for the data sampling the eastern hemisphere, and the gray circles are for the data sampling the western hemisphere. The dotted curve is the synthetic amplitude ratio from the velocity model yielded by the amplitude ratios when inner core $Q = 400$ as shown in dotted curve in Figure 2.7. Both data and synthetics have been obtained from seismograms filtered with a narrow bandpass centered at 3 s.

amplitude, and thus increases the PKP_{Cdiff}/PKP_{DF} amplitude ratio. Therefore, there is always a trade-off between inner core attenuation and the velocity structure at the base of the outer core.

We perform a similar grid search over the velocity structure at the base of the outer core as we did for the travel times. To account for the effects of inner core attenuation, we assign different inner core Q values (300, 400, 500, 600) for each of the velocity models. This range is defined based on the results of several recent investigations (e.g. *Dziewonski and Anderson, 1981; Bhattacharyya et al., 1992; Wen and Niu, 2002; Cao and Romanowicz, 2004; Yu and Wen, 2006; Garcia et al., 2006*). Therefore, the total number of models we evaluate is four times those evaluated in the travel time analysis. By minimizing the L2-norm misfit function between the observed and synthetic amplitude ratios in log-space, we find the best fitting model.

Not surprisingly, for different values of inner core Q, we obtain different best fitting models. However, all the models are significantly different from the best model found by fitting the travel times. Even when we let the inner core Q be 600, the best model with respect to the amplitude ratios still has significantly faster velocity at the base of the outer core than the best model with respect to the differential times. For example, the dotted line with shadowed area in Figure 2.7 shows the best fitting model and its uncertainty obtained from bootstrap resampling algorithm with a reasonable inner core Q value of 400. The corresponding predicted amplitude ratio curve is presented in Figure 2.8 as the dotted curve. A smaller inner core Q value decreases the PKP_{DF} amplitude, and thus requires a smaller PKP_{Cdiff} amplitude, which corresponds to a steeper velocity structure. The best model from the travel times gives too big PKP_{Cdiff} amplitudes that are inconsistent with our observations.

We check the robustness of this result with several additional tests. Allowing for a depth-dependent inner core Q, by using different combinations of Q in the upper 200 km of the inner core (Q from 100 to 1000) and Q for the rest of the inner core (Q from 600 to 1000), we find PKP_{Cdiff}/PKP_{DF} amplitude ratios for the best travel-time derived velocity model are consistently too large compared to the observations. We find the same result for several other high-quality velocity models determined in section 3.2. Considering

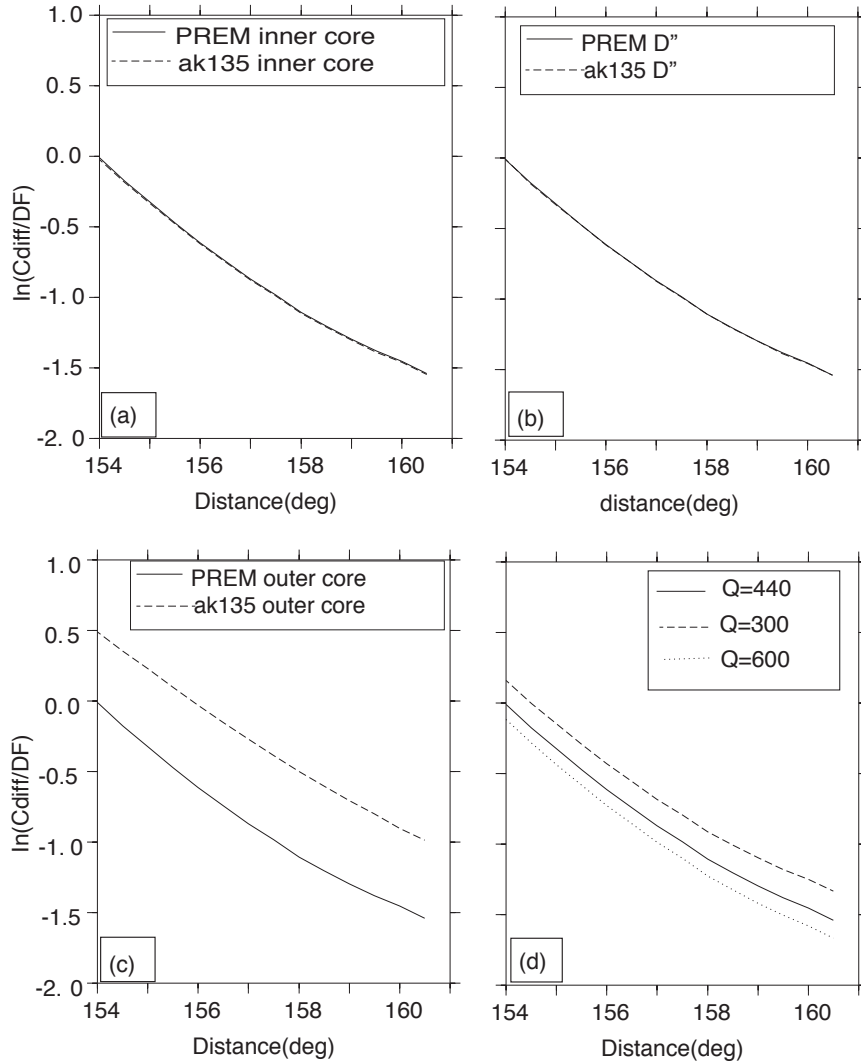


Figure 2.9: **(a)** The difference in the amplitude ratios (PKP_{Cdiff}/PKP_{DF}) caused by the velocity difference in the inner core between PREM and AK135. **(b)** The difference in the amplitude ratios (PKP_{Cdiff}/PKP_{DF}) caused by the velocity difference in the lowermost mantle between PREM and AK135. **(c)** The difference in the amplitude ratios caused by the velocity difference at the base of the outer core between PREM and AK135. In panel **(a)**, **(b)** and **(c)**, the solid curve is for PREM and the dashed one is for AK135. **(d)** The difference in the amplitude ratios caused by different inner Q values. The solid curve is for Q=440, the dashed one is for Q=300 and the dotted one is for Q=600.

a frequency-dependent inner core Q model suggested previously (e.g. *Li and Cormier, 2002; Cormier and Li, 2002*), we experiment with lower corner frequency of 0.1-0.5 Hz and find that they do not significantly change the amplitude ratios as well. We also find that changes to the density jump and shear velocity jump across the ICB have relatively small changes on the theoretical amplitude ratios, and do not allow the travel time data to be reconciled with the amplitude data.

2.5 Discussion

Our $PKP_{Cdiff} - PKP_{DF}$ differential times give a flatter velocity structure at the base of the outer core than PREM (*Dziewonski and Anderson, 1981*), which may imply a different chemical composition at the base of the outer core, as suggested by previous studies (*Souriau and Poupinet, 1991; Song and Helmberger, 1995*). However, our PKP_{Cdiff}/PKP_{DF} amplitude ratios do not support this feature (Figure 2.7), instead they prefer a PREM-type velocity structure at the base of the outer core, regardless of inner core Q values. This apparent discrepancy is indirectly supported by many previous studies. The result from the differential times is especially consistent with those studies based on travel times (e.g. *Souriau and Poupinet, 1991; Song and Helmberger, 1995; Kennett et al., 1995; Yu et al., 2005*). Meanwhile, our result from the amplitudes ratios is consistent with previous PKP_{Cdiff} amplitudes studies (*Choy and Cormier, 1983; Cormier, 1981*). Note that it is also consistent with the results of PREM2 (*Song and Helmberger, 1995*). In that study the authors found that for either constant Q or constant t^* in the inner core, the PKP_{Cdiff}/PKP_{DF} amplitude ratios predicted by PREM2 were larger than the observations (see Figure 8 in *Song and Helmberger (1995)*).

It is also important to point out that any potential bias in our data selection magnifies the discrepancy. By choosing only waveforms with high quality PKP phases, it is possible that our dataset is skewed towards abnormally large PKP_{Cdiff} waves. However, the best-fitting travel time model would be inconsistent with PKP_{Cdiff} waves even larger than what we observe. In other words, if a hypothetical perfectly averaged PKP_{Cdiff} data set has lower amplitudes than our data set, the discrepancy with the travel times would be even

bigger than what we observe.

To summarize, the observed PKP_{Cdiff} amplitudes are smaller than what is expected. This is analogous to earlier seismological studies that found unexpectedly small amplitudes for P_{diff} amplitudes, suggesting some sort of complexity in the lowermost mantle (e.g. *Ruff and Helmberger, 1982*). In that case, the preferred interpretation of the authors was of a jagged, but positive velocity gradient in the lowermost mantle, implying that D” is more complicated than a simple, thermal boundary layer. However, in our case the velocity structure just above the ICB cannot be altered to match the observed amplitudes because the predicted travel times would then become inaccurate. Instead a non-standard mechanism must exist that acts to reduce PKP_{Cdiff} amplitudes while not significantly affecting the corresponding travel times. It appears that the small-scale heterogeneity inside the inner core observed by many authors (e.g. *Vidale and Earle, 2000; Cormier and Li, 2002; Koper et al., 2004; Leyton and Koper, 2007*) would not be able to explain this discrepancy because the inner core scattering would decrease the PKP_{DF} amplitude and thus increase the PKP_{Cdiff}/PKP_{DF} ratios. We believe the two primary candidates for explaining the observed discrepancy are (1) small-scale topography or roughness on the ICB that scatters energy from the main PKP_{Cdiff} phase into trailing coda waves, and (2) a layer at the base of the outer core that possesses low intrinsic Q owing to anelastic mechanisms.

2.5.1 Hypothesis #1: A Rough ICB

Although strong coda waves following PKP_{Cdiff} have been observed, they are generally not interpreted as being caused by irregularities at the ICB (*Nakanishi, 1990; Tanaka, 2005; Zou et al., 2007*). Slowness information derived from array and polarization analysis tends instead to support scatterer locations in the mantle. However, these studies do not exclude a contribution to PKP_{Cdiff} coda waves from complexities at the ICB, and several recent studies have found independent evidence favoring a rough ICB. *Poupinet and Kennett (2004)* proposed inner core boundary scattering to explain the complexity of the $PKiKP$ coda recorded at Warramunga seismic array and suggested the ICB has some short-scale heterogeneities with lowered wavespeed. *Koper and Dombrovskaya (2005)* found large

variation in $PKiKP/P$ amplitude ratios and suggested the presence of heterogeneities at, or very near the ICB. Significant variability of $PKiKP$ amplitudes from explosion sources also led to the suggestion of a mosaic structure at the inner core's surface (*Krasnoshchekov et al.*, 2005). Most recently, high-quality earthquake doublet data recorded at different locations suggested that small-wavelength, irregular topography is present at the ICB (*Wen*, 2006; *Cao et al.*, 2007).

To evaluate this hypothesis numerical simulations of short-period PKP_{Cdiff} waves for rough ICB models need to be carried out to determine if geodynamically reasonable structures have the desired effect. This is a difficult problem that is outside the scope of this paper, but it is potentially feasible using modern computation approaches such as the axi-symmetric finite difference method that has recently been used to simulate the effect of complicated CMB models on ScS and core grazing S waves (*Lay et al.*, 2006), or the pseudo-spectral method recently applied to inner core scattered waves (*Cormier*, 2007). A numerical evaluation is also important because of the counter-intuitive possibility that a rough ICB would lead to enhanced PKP_{Cdiff} amplitudes, as in Biot scattering associated with seafloor topography (*Menke*, 1982).

2.5.2 Hypothesis #2: A Slurry Zone at the Base of the Outer Core

In this scenario, we hypothesize that intrinsic attenuation in the lowermost outer core is much higher compared to the rest of the outer core. Thus, the amplitude of PKP_{Cdiff} would be significantly reduced while travelling horizontally in the low-Q layer, but PKP_{DF} amplitudes would be less affected because of the steeper ray paths through the layer. This type of model has been suggested on geodynamical grounds and termed a slurry zone (*Loper and Roberts*, 1978; *Loper*, 1978; *Loper and Roberts*, 1981). Such a feature could be formed by the nucleation and gradual precipitation of solid particles from super-cooled fluid at the base of the outer core. Alternatively, the super-cooling instability could lead to the radial growth of dendritic arms of solid material from the inner core into the outer core, forming a thin, mushy zone; presumably, dendrites from the mushy zone could be broken and distributed throughout the base of the outer core by large scale convective motions

(Copley *et al.*, 1970; Loper and Roberts, 1978). Internal friction between suspended solid particles and the surrounding fluid is expected for seismic waves traversing the region, and therefore the slurry layer might be expected to have relatively low Q compared to the rest of the outer core.

To our knowledge, there has been only one seismic study in which such a model has been quantitatively evaluated (Cormier, 1981). In this model (designated as QIC3) Q increased smoothly from 200 to 10,000 as the radius increased from the ICB to about 250 km shallower. QIC3 was rejected because it underpredicted absolute short-period PKP_{DF} amplitudes measured at WWSSN stations (Buchbinder, 1971). However, we note that QIC3 also possessed an extremely low- Q layer at the top of the inner core, with a minimum Q value of 125 just beneath the ICB tapering to a Q value of 1000 about 250 km beneath the ICB.

To evaluate the possibility of a low- Q layer at the base of the outer core we carry out a systematic grid search similar to the ones described earlier. We fix the velocity structure to the model preferred by the $PKP_{DF} - PKP_{Cdiff}$ differential travel times (Figure 7) and search over a range of Q values (from 100 to 600 with 50 as the interval) and thicknesses (from 50 km to 400 km with 50 km as the interval) to find the parameters that best fit the observed PKP_{DF}/PKP_{Cdiff} amplitude ratios. Assuming an inner core Q of 400, the best model has a Q of 300 over the bottom 350 km of the outer core. In this case, the predicted amplitude ratio curve is very close to the synthetic curve (the dotted curve in Figure 2.8) from the best model preferred by the amplitude ratios. Unfortunately, the problem is underdetermined as there are significant trade-offs among the model parameters: between inner core Q and outer core Q , and between outer core Q and layer thickness. However, we do find that extremely thin (< 100 km) outer core low- Q layers are incompatible with the amplitude ratios because they lead to overly steep decay rates.

The best-fitting models found above significantly reduce absolute PKP_{DF} amplitudes, although not as much as QIC3. For instance, with a Q of 300 at the bottom 350 km outer core, PKP_{DF} amplitude decreases by 24%, and PKP_{Cdiff} amplitude decreases by 52% at distance of 158° . This effect would be expected to be larger at smaller distances, as PKP_{DF} travel less steeply through the base of the outer core; however, the variation in

absolute PKP_{DF} amplitude is on the same order predicted for models with extremely low-Q layers at the top of the inner core and a standard outer core model.

2.6 Conclusions

We systematically searched the high-quality PKP_{Cdiff} waveforms from all the temporary networks with data currently available at IRIS DMC and some regional seismic arrays to assemble the largest PKP_{Cdiff} data set ever. Our best model derived by fitting the differential times ($PKP_{Cdiff} - PKP_{DF}$) indicates that the velocity and its gradient at the base of the outer core are significantly lower than those in PREM, which is consistent with many previous studies (e.g. *Souriau and Poupinet, 1991; Song and Helmberger, 1995; Kennett et al., 1995; Yu et al., 2005*). The relatively low gradient at the base of the outer core implies that the Bullen parameter is significantly greater than 1, which in turn implies the existence of an abnormally dense layer at the base of the outer core (*Souriau and Poupinet, 1991; Song and Helmberger, 1995*). This may explain why recent body wave estimates of the density jump across the ICB are smaller than estimates made from broadly sensitive normal mode observations (*Koper and Dombrovskaya, 2005*).

However, our best fitting model derived from the amplitude ratios lacks the flat velocity profile at the base of the outer core required by the travel times, and instead it is closer to the velocity profile in PREM. This result is also consistent with some previous PKP_{Cdiff} amplitude studies (*Choy and Cormier, 1983; Cormier, 1981*). We believe the velocity profile at the base of the outer core is in fact significantly flatter than PREM, as revealed by our travel time analysis, and that observed PKP_{Cdiff} amplitudes are reduced by a non-standard mechanism not normally included in synthetic seismograms.

One way to reconcile our travel time and amplitude observations is with the existence of rough topography on the ICB that acts to scatter energy away from PKP_{Cdiff} as it propagates horizontally above the ICB. A complicated or rough ICB has recently been suggested by several authors using independent data sets of waves reflected from the ICB (*Poupinet and Kennett, 2004; Koper and Dombrovskaya, 2005; Krasnoshchekov et al., 2005; Wen, 2006; Cao et al., 2007*). This would be an elastic process in which energy is partitioned

away from the main phases into later arriving coda waves. Several researchers have examined unusual looking PKP_{Cdiff} coda waves, but to date all of the analyses have preferred mantle locations for the scatterers. Nevertheless, the evidence from the $PKiKP$ studies warrants the future numerical experimentation to determine if reasonable models of ICB complexity can produce the needed reduction in PKP_{Cdiff} amplitudes, while leaving PKP_{Cdiff} travel times relatively unchanged.

A second way to reconcile our observations is with the existence of a relatively low-Q layer at the base of the outer core. For example, a model with flat velocities at the base of the outer core (similar to AK135), an inner core Q_p of 400, and a 350 km thick layer with Q_p of 300 at the bottom of the outer core fits both the travel time and amplitude constraints. Therefore, besides being unusually dense, the base of the outer core may also be unusually attenuating at body wave periods (1-10 s). A physical model for such properties was suggested by *Loper and Roberts (1978)* in the form of a slurry layer of suspended solid Fe particles in a fluid matrix. Extrapolating results of ultrasonic attenuation experiments with metal powder-viscous liquid suspensions (*Schulitz et al., 1998*) suggests that the viscosity of such a slurry would be on the order of 10^{11} Pa s to produce the observed body wave attenuation. Recent metallurgical studies, however, suggest that such a slurry layer is unlikely to exist, because of the dendritic growth patterns observed in solidifying metals (*Bergman, 1997; Bergman et al., 2005*). However, a recent study (*Gubbins et al., 2007*) re-investigated this scenario and proposed a core model in which part of the light components forms a solid upon freezing of the inner core, and then floats upwards and remelts at some point. To fit the seismic properties and heat fluxes, their preferred model has a 200 km thick layer at the base of the outer core which has less light elements concentration than the rest of the outer core. This provides a physical explanation for the larger density gradient and smaller velocity gradient for the bottom 200 km of the outer core, and the possible low Q there as well.

Although bulk Q in the upper 1000 km of the outer core has been measured to be nearly infinity from high frequency body waves (e.g. *Cormier and Ricards, 1976*), it is possible there may be some deeper bulk attenuation. This idea of a low-Q layer at the base of the fluid core can be further evaluated in two ways. First, the optimal models reported here can

be tested against the large databases of PKP_{DF}/PKP_{AB-BC} amplitude ratios that exist at distances both smaller and larger than the range considered here (*Garcia et al.*, 2006). Second, the low-Q models can be tested against normal mode observations. A recent study that used a global search algorithm to fit a large database of normal mode observations found that existing radial Q_κ models of the outer are too large by factors of 2-10 (*Resovsky et al.*, 2005). Those authors preferred a value of $Q_\kappa \sim 6000$ for the outer core, a value much higher than suggested here for the base of the outer core; however, the outer core was treated as a single layer and no allowance was made for variation within this layer. Because the mode data averages significantly over radius, it's possible a low-Q layer is consistent with the data if a more flexible parametrization is used.

Chapter 3

Partial Melt in the Lowermost Mantle Near the Base of a Plume

Precursors to the seismic core phase PKP have long been used to study small-scale heterogeneities at the base of the mantle. They are preferred to PKP coda waves (postcursors) because the latter are more biased by shallow structure, and so are cruder probes of the deep Earth. In this work, however, we present an array-based analysis of PKP coda waves that provides a unique opportunity to image small-scale structure in the deep mantle. Seismograms of a Peru earthquake recorded by an array of broadband seismometers in Tibet show strong coda waves following PKP_{Cdiff} . The coda waves are strongest for distances of $154^\circ - 157^\circ$ at frequencies above 0.5 Hz. No such strong coda waves exist after PKP_{DF} and PKP_{AB} , and an empirical source time function of the earthquake is likewise simple. This implies that the coda waves are being created by anomalous structures deep within the Earth. Using slant stack analysis we find that the ray parameter of the PKP_{Cdiff} coda waves is similar to that of the main PKP_{Cdiff} phase, implying that the coda waves are not simple precursors to the minimax PKP_{AB} phase. Combined modeling of the differential travel times, differential slownesses ($PKP_{DF}-PKP_{Cdiff}$), and envelopes of the coda suggests that the waves are created by strong heterogeneity at the source side of the lowermost mantle that scatters incident P energy into postcritical reflections from the inner core boundary ($P.PKP_{CD}$). Although the precise geometry is unconstrained, if we use single scattering theory the data are consistent with a region of at least 15% P wave velocity reduction. The most likely cause for such a strong velocity anomaly is the presence of partial melt. The geographical location of the anomalous region, beneath the Amazon River in South America, roughly corresponds with the expected base of a newly discovered plume.

3.1 Introduction

Precursors to the core phase *PKP* were observed in the shadow zone as early as 1934 (*Gutenberg and Richter, 1934*), but debate has continued until the present on their origin and implications. Early studies of the precursors favored the presence of a transition layer between the outer and inner cores (*Bolt, 1962; Sacks and Saa, 1969*). The first challenge to this idea came from Doornbos and Husebye's array-based observations that the travel times and slownesses of the precursors were inconsistent with the transition layer interpretation (*Doornbos and Husebye, 1972*). Moreover, *Cleary and Haddon (1972)* showed that the theoretical travel time curve of singly scattered waves generated by irregularities near the core-mantle boundary (CMB) was consistent with the observations of travel time and slowness. By adapting Chernov's acoustic scattering theory (*Chernov, 1960*) to elastic media, *Haddon and Cleary (1974)* first computed scattered amplitudes due to volumetric inhomogeneities and showed that random heterogeneities of 1 per cent variation in seismic velocity and density throughout a 200 km thick D'' can explain the observed energy level of precursors. Later computations of the amplitude of scattered waves due to an irregular CMB topography by *Doornbos (1978)* indicated that a few hundred meters in height would also produce the observed energy level, a result confirmed by *Bataille and Flatte (1988)*.

Although it is now generally accepted that *PKP* precursors are generated by the scattering of volumetric inhomogeneities in the mantle or CMB topography (*Bataille et al., 1990*), the debate about their distribution and properties, and what they imply about the Earth, remains active. Small-scale weak heterogeneity (1 per cent r.m.s. velocity variation) uniformly distributed throughout the mantle is supported by the modelling of *PKP* precursor amplitudes (*Hedlin et al., 1997*). However, anomalously large *PKP* precursors from earthquakes in northern Tonga indicate much stronger regional heterogeneity (10-15 per cent r.m.s. velocity variation) in a layer about 60 km thick near the CMB, supporting the presence of partial melt (*Vidale and Hedlin, 1998*). *PKP* precursors sampling the ultra-low velocity zone (ULVZ) at the CMB beneath the Western Pacific also support the presence of partial melt in a region 60 km to 80 km in height, with at least 7 per cent r.m.s. velocity perturbation (*Wen and Helmberger, 1998*). However, not all heterogeneity in the

lower mantle is thought to be related to partial melt, for example, an analysis of PcP precursors in the North Atlantic indicating the existence of small-scale heterogeneities with weak positive velocity anomaly in the lowermost mantle, is consistent with chemical heterogeneity (*Braña and Helffrich, 2004*).

Precursors to PKP have been frequently used to study the small-scale structure of the deep Earth because they are not contaminated by late-arriving scattered waves created by shallow structures. The utility of postcursors to PKP (coda waves) has also been investigated although it is a less sensitive probe for inferring mantle heterogeneity. *Hedlin and Shearer (2002)* analyzed PKP recordings filtered in the bandpass from 0.7 and 2.5 Hz at distances from 120° to 145° and concluded the existence of small-scale heterogeneities with 1 per cent r.m.s. velocity variation throughout the lower mantle. However, the coda arrivals did not strongly constrain the vertical distribution of heterogeneity in the mantle because of the large standard errors of their stacked data, presumably caused by interference with the energy scattered from shallower depth. *Nakanishi (1990)* observed PKP_{Cdiff} coda waves from a deep earthquake at a seismic array in Japan and pointed out the complicated frequency-dependent phenomenon of PKP_{Cdiff} coda waves. He found a slowness of the coda waves of ~ 4 s/deg, which is approximately equal to that of PKP_{AB} , and interpreted them as the scattering from the upper mantle (about 650 km). More recently, *Tanaka (2005)* presented characteristics of PKP_{Cdiff} coda waves from the small-aperture array short-period stations of the International Monitoring System. He observed wide range of slownesses for the PKP_{Cdiff} coda waves, and interpreted the coda waves with slowness larger than 2 s/deg as scattering from the core-mantle boundary under the source side and receiver side, although an ICB origin could not be ruled out.

Here we present an analysis of a high quality PKP_{Cdiff} record section recorded by a temporary array of broadband seismometers in Tibet (INDEPTH-III, International Deep Profiling of Tibet and the Himalaya Phase III). The seismograms were generated from a deep Peru earthquake and show enormous PKP_{Cdiff} coda waves at distances of $154.7^\circ - 157^\circ$. Combined modeling of the travel time, horizontal slowness, amplitude, and frequency content of the coda waves leads to a precise estimate of the location and properties of the anomalous Earth structure responsible for creating the coda waves.

3.2 Data

The INDEPTH-III array consisted of 54 broadband and short period seismometers deployed from August, 1998 through May, 1999 (Figure 3.1). The stations were arranged in a linear geometry with interstation spacing of about 10 km, and were well-positioned to record PKP waves from earthquakes in the South America subduction zone. One earthquake with moment magnitude 6.1 in Peru (event 981008 in Figure 3.1) in particular showed clear PKP_{Cdiff} waves followed by prominent coda waves at distances of $154.7^\circ - 157^\circ$ (Figure 3.2). For an event at this depth the C-cusp of the PKP travel time curve occurs at approximately 152.6° in PREM (Dziewonski and Anderson, 1981), and past this point geometric ray theory predicts no arrivals. However, calculations using full wave theory show that significant diffracted energy exists well past the C-cusp, even at relatively high frequencies (Cormier, 1981).

We selected those broadband recordings of PKP_{Cdiff} with high signal-to-noise ratio (SNR), and applied different bandpass filtering to the waveforms. We found that the amplitudes of these coda waves decrease for longer periods: they are clearly seen above 0.5 Hz and are not seen at lower frequencies. In Figure 3.2 we present a vertical component record section in a higher frequency passband (0.33-0.67 Hz) and a lower frequency passband (0.067-0.133 Hz). Note that at the lower frequencies the PKP_{Cdiff} coda waves essentially disappear and after about 157° the coda waves disappear even in the higher frequency band. It is important to point out that we do not see PKP_{Cdiff} coda waves from two neighboring events (events 990302 with M_w 5.9 and 990305 with M_w 5.8) with distance ranges of $157.2^\circ - 159.3^\circ$ and $156.1^\circ - 158.1^\circ$, respectively, although PKP_{Cdiff} itself is clearly seen for both of them (Figure 3.3 and Figure 3.4).

3.3 Ray Parameter of PKP_{Cdiff} Coda

In order to identify the origin of the high-frequency coda following PKP_{Cdiff} (Figure 3.2), we used a slant stack analysis. First, we aligned all of the traces with cross correlation over the PKP_{DF} time window. We then fixed the backazimuth at the theoretical value and

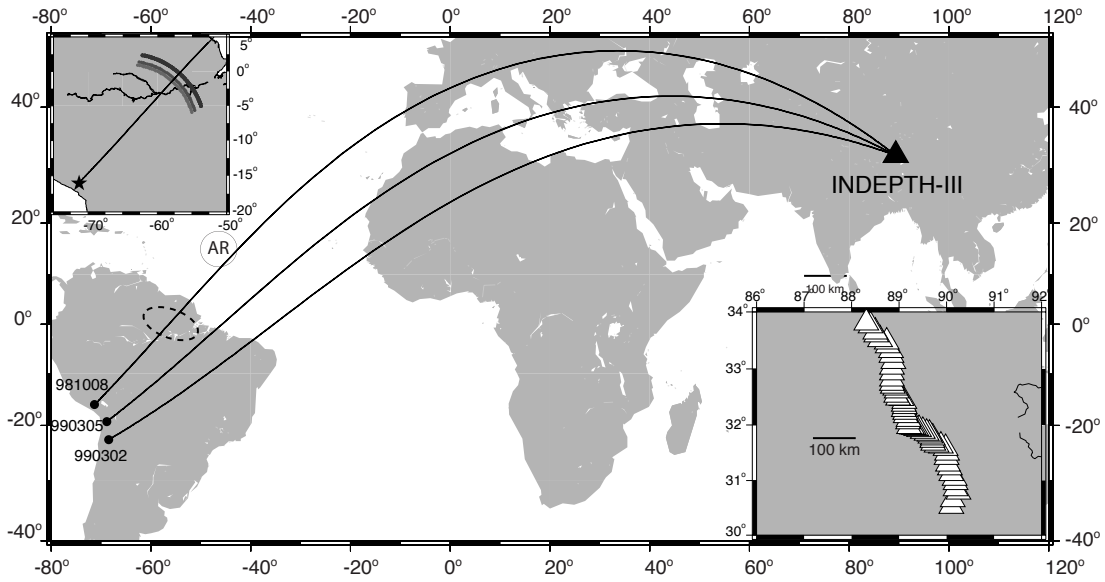


Figure 3.1: Source-receiver geometry for the seismic data presented here. The three dots represent the locations of the three events (981008: 16.12°S , 71.40°W , 136 km; 990305: 20.42°S , 68.96°W , 106 km; 990302: 22.72°S , 68.50°W , 110 km). The solid triangle is where the INDEPTH-III array was deployed. The ellipse marks the region at the CMB where partial melt is likely to exist, and the heavy black curves represent the great circle path (theoretically, the seismic ray path) from the events to the array. The circle with "AR" inside is the surface location of the Atlantic ridge plume (from *Montelli et al.* 2004). The upper left insert shows the detailed possible location of the partial melt at the CMB, in darker gray for PREM, lighter for PREM2, and lightest for AK135. The lower right insert shows the configuration of the INDEPTH-III array.

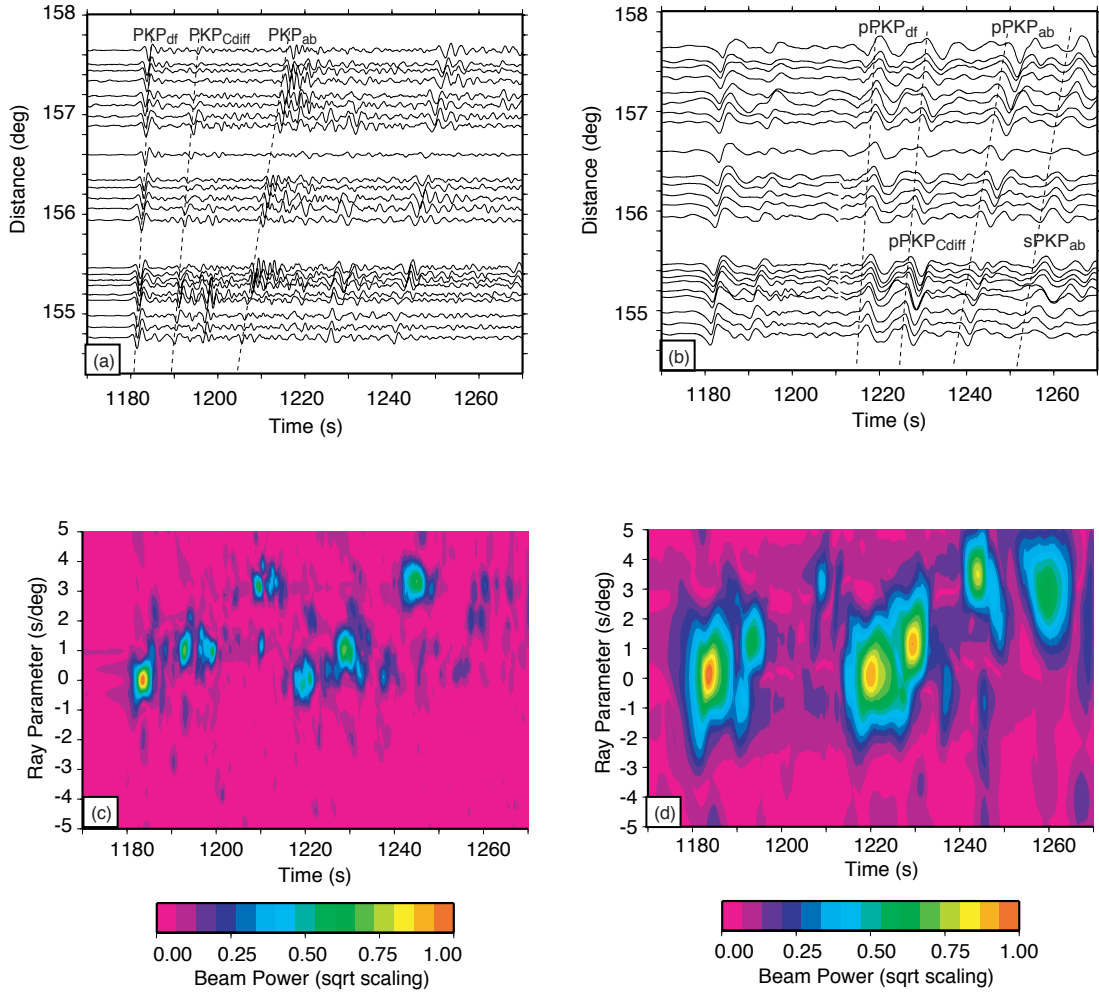


Figure 3.2: **(a)** Vertical component record section at the INDEPTH-III array for the Peru earthquake (event 981008 illustrated in Fig. 1). The traces have been bandpass filtered at 0.333-0.667 Hz. Theoretical arrival times for PKP_{DF} , PKP_{Cdiff} and PKP_{AB} in PREM are shown as dashed lines. Note the prominence of the coda waves following PKP_{Cdiff} and their quick decay after a distance of about 157° . **(b)** Same as **(a)** except that the waveforms have been bandpass filtered at 0.067-0.133 Hz. Theoretical arrival times for the depth phases $pPKP_{DF}$, $pPKP_{Cdiff}$, $pPKP_{AB}$ and $sPKP_{AB}$ in PREM are marked as dashed lines. The PKP_{Cdiff} coda waves have disappeared, but the depth phases are more prominent. **(c)** Differential slowness with respect to PKP_{DF} in the high frequency band. The slant stack does not include the data after 157° . The arrival at 1182 s with 0 s/deg is PKP_{DF} , and at 1192 s with a slowness of 0.84 s/deg is PKP_{Cdiff} . The clear arrival at about 1200 s has a similar slowness to PKP_{Cdiff} . PKP_{AB} has slowness of about 3 s/deg at 1212 s. The depth phases with similar slowness as their corresponding direct arrivals are also shown in the figure. $pPKP_{DF}$ arrives at 1220 s, $pPKP_{Cdiff}$ arrives at 1230 s and $pPKP_{AB}$ arrives at about 1250 s. **(d)** Same as **(c)** but for the low frequency band. Note the poorer slowness resolution compared to the high frequency band.

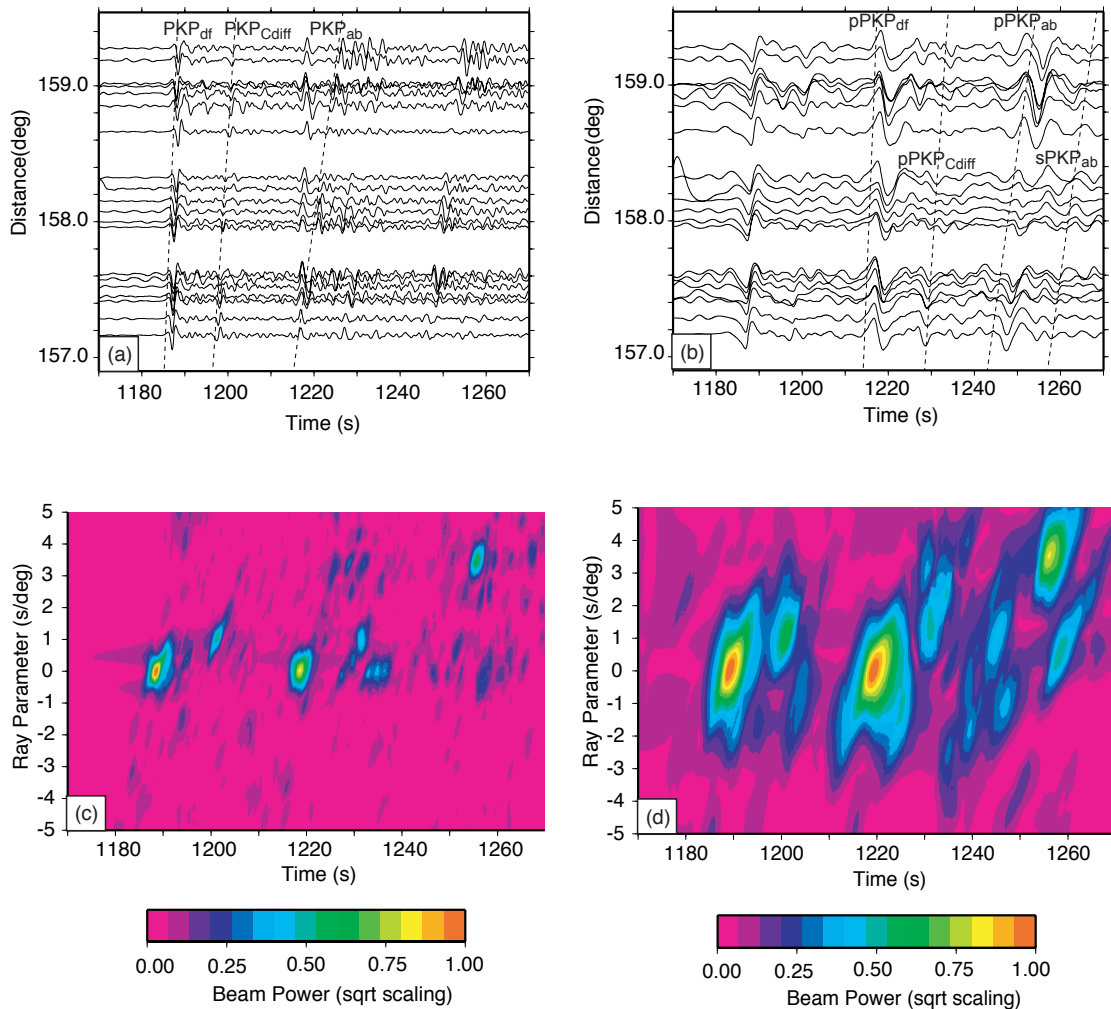


Figure 3.3: The same as Figure 3.2 except for another South America earthquake recorded at INDEPTH-III (event 990302 in Fig. 1). From both the waveforms and the slant stack analysis, there is a lack of energy for the PKP_{Cdiff} coda even though the PKP_{Cdiff} itself is very strong.

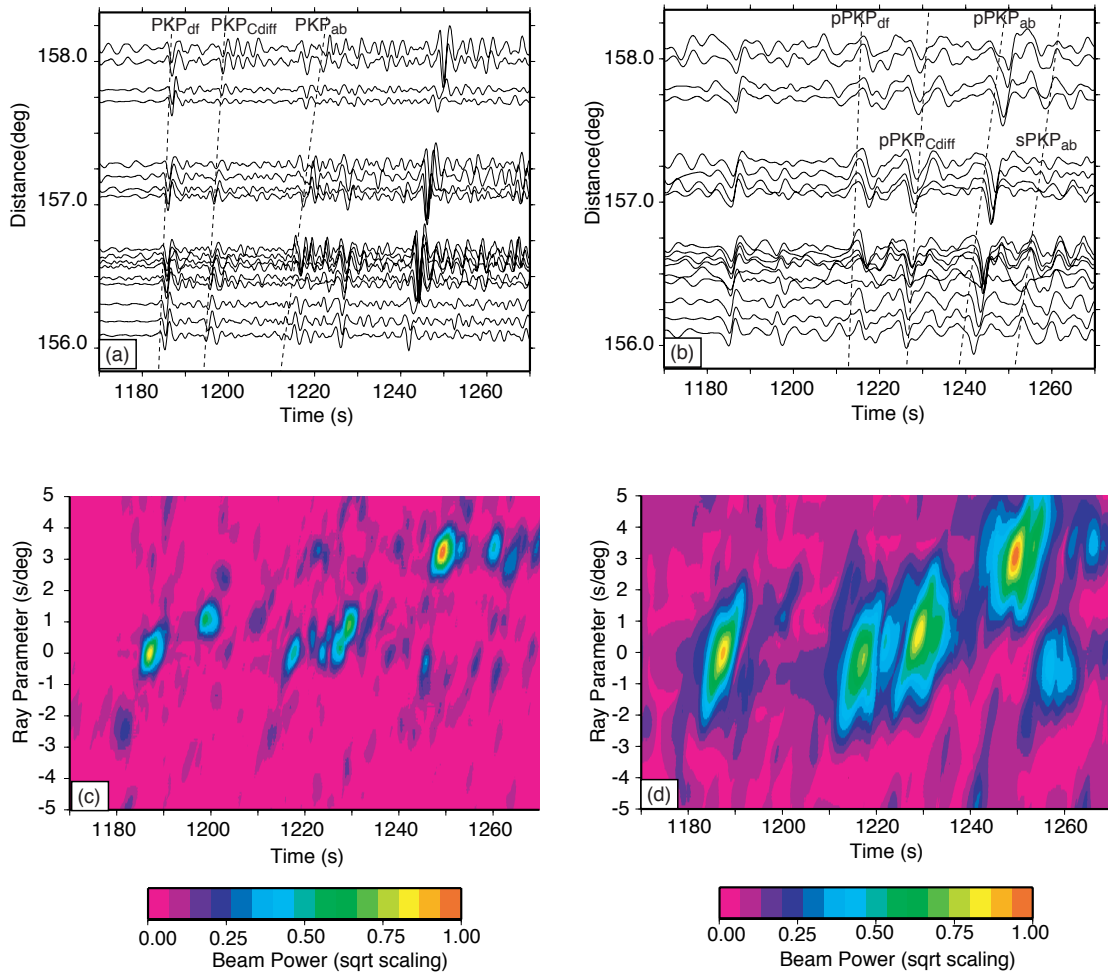


Figure 3.4: The same as Fig. 2 except for event 990305 in Fig. 1. From both the waveforms and the slant stack analysis, there is a lack of energy for the PKP_{cdiff} coda even though the PKP_{cdiff} itself is very strong.

made stacks for various values of the differential ray parameter. We chose a third order phase-weighted stack (PWS) method to reduce the incoherent noise in the array recordings (Schimmel and Paulssen, 1997). Because of the high SNR of the data and the relatively large aperture of the array, we have very good resolution in slowness, and the relatively small differences in ray parameter among the PKP waves are readily apparent (Figure 3.2). The slant stack clearly shows two separate peaks for PKP_{Cdiff} and its coda above 0.5 Hz, while at low frequencies it shows a peak only at the time of PKP_{Cdiff} . Note that the differential ray parameter of the PKP_{Cdiff} coda (0.84 s/deg) is very close to the differential ray parameter of PKP_{Cdiff} (0.94 s/deg), and much smaller than the differential ray parameter of PKP_{AB} (3.07 s/deg). This suggests that the coda waves following PKP_{Cdiff} are not simple precursors to the minimax phase PKP_{AB} .

To quantify the resolution of the slowness estimates we applied a bootstrap-type resampling algorithm (Tichelaar and Ruff, 1989). We randomly resampled the array elements with replacement, generating a pseudo-array with the same number of traces as the true array. We then performed a slant stack and found the optimal arrival time and differential ray parameter for each phase. Repeating this process 100 times, we generated a population of pseudo-solutions that was in turn used to estimate standard errors (1σ) for the actual solutions. The differential ray parameter of PKP_{DF} is 0.00 ± 0.03 s/deg (since we used PKP_{DF} as the reference phase) and the arrival time is 1183.15 ± 0.04 s at the array reference distance of 155.4° . The differential ray parameter of PKP_{Cdiff} is about 0.94 ± 0.06 s/deg at a time of 1192.55 ± 0.06 s, and the differential ray parameter of the PKP_{Cdiff} coda is 0.84 ± 0.06 s/deg at a time of 1198.80 ± 0.07 s. To test the robustness of these results we varied the backazimuth by $\pm 5^\circ$ and repeated the estimation process. The optimal differential ray parameters changed by less than 0.06 s/deg and had error bounds similar to those described above. We also experimented with stacks created by varying the backazimuth for a constant differential ray parameter. Using a similar bootstrap process we estimated the backazimuth of both PKP_{Cdiff} and its coda to be $307 \pm 8^\circ$, essentially indistinguishable from the theoretical backazimuth of 308° used in making the ray parameter estimates.

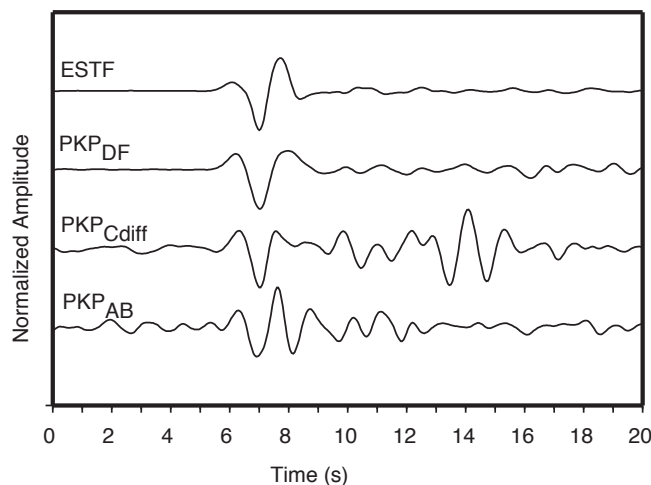


Figure 3.5: Comparison of waveforms of the empirical source time function (ESTF), PKP_{DF} , PKP_{Cdiff} , and PKP_{AB} for event 981008. All the waveforms have been filtered at 0.667-1.333 Hz. Only PKP_{Cdiff} has a prominent coda.

3.4 The Origin of the PKP_{Cdiff} Coda

To rule out the possibility that the PKP_{Cdiff} coda waves are due to source complexity, we obtained an empirical source time function (ESTF) using the first eigen-image technique (Ulrych *et al.*, 1999) on 15 teleseismic ($63^\circ - 70^\circ$) recordings with high SNRs. The first eigen-image represents the most coherent signal from trace to trace and so it is a good estimate of the source time function after excluding later phases (Bostock and Rondenay, 1999). We found a relatively simple ESTF for the event and no prominent energy within 10 s of the first arrival. As a comparison, we stacked all the traces after aligning them according to PKP_{DF} , PKP_{Cdiff} , and PKP_{AB} , respectively. Comparing the four waveforms, only PKP_{Cdiff} shows a prominent coda (Figure 3.5). Therefore the PKP_{Cdiff} coda is not due to source complexity, and is unrelated to heterogeneity near the source or the receivers. We also note that convolving the ESTF with a synthetic record section calculated by full wave theory (Cormier and Richards, 1988) for a radial Earth model does a good job of reproducing the observed PKP phases, excepting the anomalous coda waves (Figure 3.6).

We investigated the origin of the PKP_{Cdiff} coda using ray theory (therefore we restrict the modeling to high frequencies) to compute the travel time, amplitude, and slowness

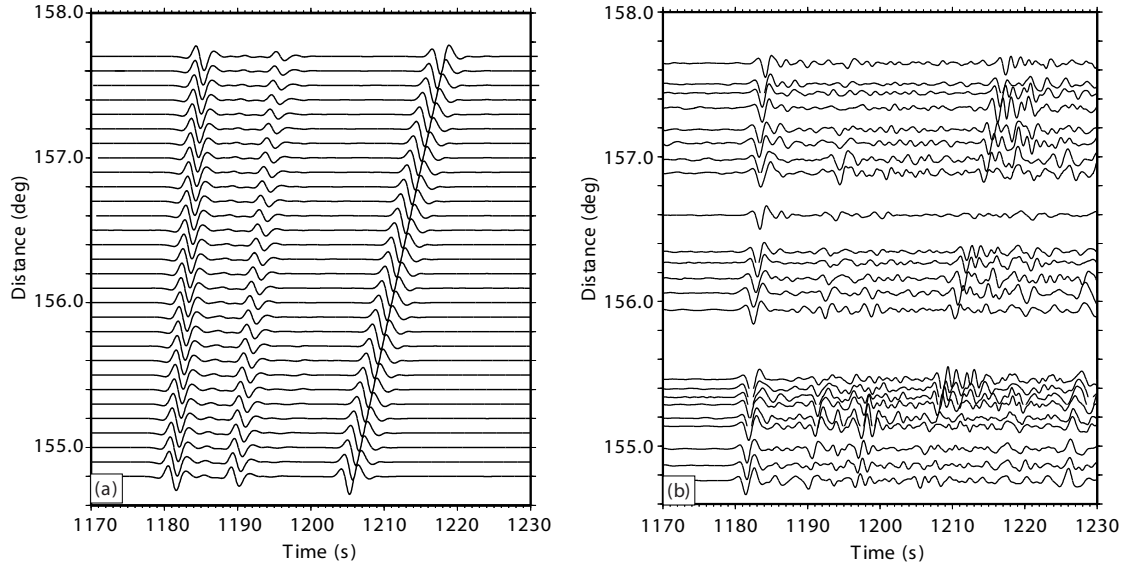


Figure 3.6: Comparison between **(a)** synthetic seismograms calculated by full wave theory in PREM and **(b)** the real data for event 981008. Both synthetic and observed seismograms are filtered around 2 s. We obtain the synthetic seismogram by convolving the synthetics obtained from full wave theory with the empirical source time function (ESTF) presented in Figure 3.3. No depth phases are included in the synthetic seismograms.

of waves scattered inside the Earth from various hypothetical locations. The basic idea is to consider potential point scatterers in a region, propagate a down-going ray from the source to each scatterer, and then propagate an up-going ray from each scatterer to the receiver. In general the ray parameter changes after the ray interacts with the scatterer, and we determined appropriate values to reach the receiver using pre-computed lookup tables relating depth, distance, and ray parameter, that were calculated for a spherical Earth model PREM (*Dziewonski and Anderson, 1981*). Given the appropriate ray parameter, we calculated the travel time and the amplitude by numerically integrating the corresponding expressions (*Červený, 2001*), which include the attenuation and geometrical spreading. We tested various schemes and found that use of the trapezoid rule with a step of 0.1 km gave accurate results. We accounted for the amplitude variations in the down-going rays induced by the radiation pattern of the earthquake using standard relations (*Aki and Richards, 2002*) and the Harvard CMT solution (see www.seismology.harvard.edu/CMT).

The change in amplitude during the scattering process can be estimated by using an equivalent reflection coefficient, obtained from the propagation of an elastic wave in a

heterogeneous medium (*Wu and Aki, 1985a,b*):

$$g^{PP}(\theta) = \frac{2(\omega/\alpha_0)^4 a^3 (\delta\alpha/\alpha_0)^2 (\cos\theta + \frac{1}{3} + \frac{2}{3} \cos^2\theta)^2}{(1 + 4(\omega^2/\alpha_0^2) a^2 \sin^2(\theta/2))^2}, \quad (3.1)$$

where θ is the scattering angle, ω is the angular frequency, a is correlation distance, α_0 is the background medium velocity, and $\delta\alpha$ is the P wave velocity variation in the heterogeneous medium. Here we have assumed an exponential autocorrelation function, which is commonly made in modeling crustal heterogeneity (*Sato and Fehler, 1998*). Continuing to consider only the relative amplitude variation among hypothetical scattered waves, we held all the variables on the right-hand-side of equation (1) constant, and calculated g^{PP} based on the value of θ that was appropriate for the change in ray parameter. In practice, this amplitude variation is small because our particular geometry is close to forward scattering ($\theta \approx 14^\circ$), but we nevertheless included it in our calculations. Finally, we projected the amplitude of the resulting up-going wave in the vertical direction and accounted for the free surface effect (*Červený, 2001*).

We computed the effect of a volumetric scattering by ray-tracing for the rays that leave the source to the scattering region (pre-scattering). Then, they interact with the scatterer by means of the apparent reflection coefficient mentioned before. Finally, we send the rays towards the receiver through the post-scattering ray (also using ray-tracing techniques). In Figure 3.7 we present the results of these calculations assuming that the causative scatterer is located just above the CMB and somewhere along the great circle path (i.e., in the sagittal plane). The scatterer produces 4 new core phases: $P.PKP_{DF}$, $P.PKP_{CD}$, and $P.PKP_{BC}$ in analogy with the normal PKP branches (Figure 3.7a), as well as a retrograde version of $P.PKP_{DF}$, which is not presented in Figure 3.7. There are significant differences in the relative amplitudes of the scattered waves, with the postcritical reflection from the ICB ($P.PKP_{CD}$) being the largest (Figure 3.7b). By matching the observed $P.PKP_{CD} - PKP_{DF}$ differential travel time with our numerical predictions we find a unique location for the scatterer, that also predicts a $P.PKP_{CD} - PKP_{DF}$ differential ray parameter that matches our observations (Figure 3.7c). This interpretation is supported by

two additional observations. First, for our source-receiver geometry, $P.PKP_{CD}$ only exists to a distance of $156^\circ - 158^\circ$; afterwards it begins to diffract and quickly loses energy. The precise distance of the cusp depends somewhat on the assumed reference Earth model. This then explains the sudden decrease of the observed PKP_{Cdiff} coda waves past about 157° (Figure 3.2), as well as the lack of significant PKP_{Cdiff} coda waves for two neighboring earthquakes that generated PKP waves across the INDEPTH-III array at slightly larger distances (Figure 3.3 and Figure 3.4), although it is also possibly because they sample slightly different area at the CMB. Second, note that the PKP_{Cdiff} coda wave has a shape much more similar to PKP_{AB} than the other pulses. PKP_{AB} passes through a caustic and so picks up a phase shift of 90° (Hilbert transform) with respect to the source pulse. It is expected that $P.PKP_{CD}$, being a post-critical reflection, would have a significant phase shift as well, and in fact the computed value is 83° .

Under the above assumptions, the geographical location of the scattering region is about 20° from the epicenter, roughly at 0.2°S and 56.9°W , beneath the Amazon basin. The precise distance along the great circle path depends on the assumed 1D reference model, and the distance off the great circle path is bounded by the observed uncertainties in the back-azimuth of $P.PKP_{CD}$. These constraints define an annular segment just above the CMB as shown by the ellipse in Figure 3.1. Unfortunately, there is still a trade-off involving the exact depth of the scattering region. For instance, the differential travel time and slowness observations of $P.PKP_{CD}$ can be equally well explained by placing the scattering region simultaneously at shallower depths (up to about 1100 km above the CMB) and smaller epicentral distances (down to 10°). However, we are confident that the scattering region is indeed located on the source side of the lower mantle. Any location on the receiver side of the lower mantle will produce large differential ray parameters at the appropriate time. Placing the heterogeneity at the inner core boundary would require a P wave to travel for almost 60° as a diffracted wave in order to arrive at the receiver with the appropriate time as in the data. In this case, the energy (especially the higher frequency contents) would be strongly attenuated, which is inconsistent with our observations. Locating the scatterer in the upper mantle would lead to the appearance of scattered phases after every direct PKP arrival, again inconsistent with our observations.

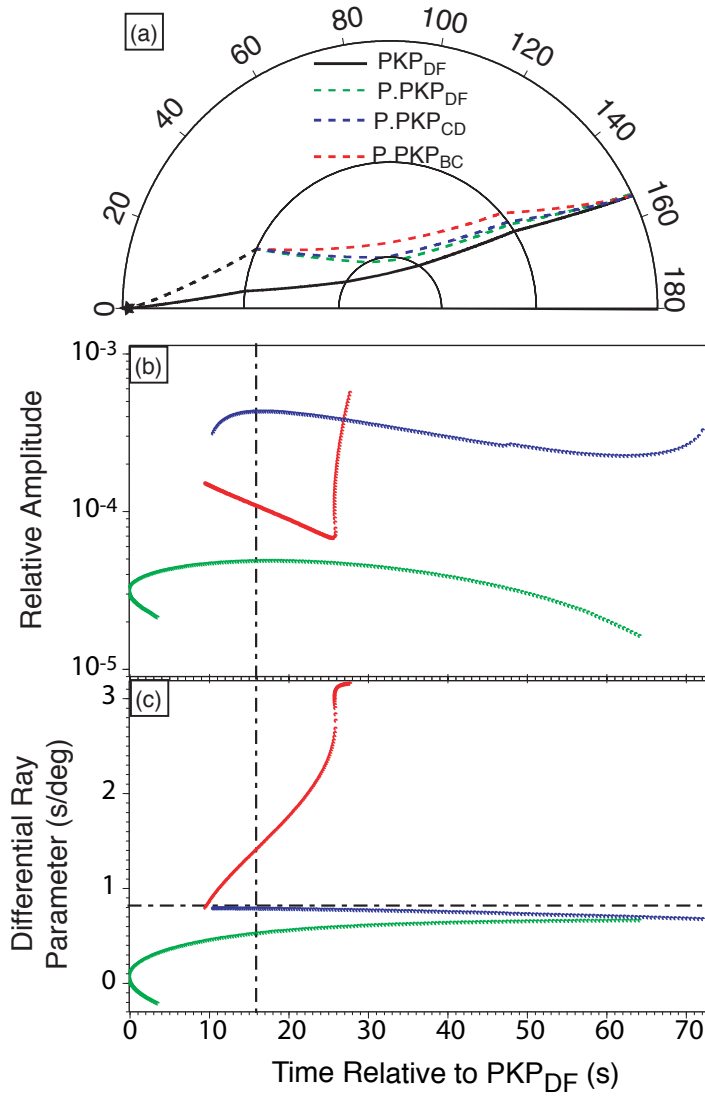


Figure 3.7: Properties of the geometrical scattered waves that result from a heterogeneity located at the CMB, 20° from the source: **(a)** ray paths of the direct arrival of PKP_{DF} (black full line) and 3 scattered waves (green for $P.PKP_{DF}$, blue for $P.PKP_{CD}$, and red for $P.PKP_{BC}$); **(b)** Relative amplitude with respect to PKP_{DF} by assuming both the velocity perturbation and scattering volume are 1; and **(c)** their differential ray parameter with respect to PKP_{DF} (following the same color code). The dashed black lines in the two lower panels show the differential time and differential ray parameter observed for the PKP_{Cdiff} coda, corresponding to the scatterer position shown in **(a)**.

Further insight on the nature of the scattering region can be gained by considering the relative amplitude of $P.PKP_{CD}$. Assuming a random inhomogeneous medium and the single scattering approximation (*Wu and Aki, 1985a; Cormier, 1995*), the directional scattering coefficient, g^{PP} , is related to the observed scattered wave amplitude, A , by:

$$\left(\frac{A}{A_0}\right)^2 = \frac{Vg^{PP}(\theta)}{G(r)} \quad (3.2)$$

where $G(r)$ is the geometric spreading with r as the total traveled distance, V is the scattering volume, and A_0 is the amplitude of the incident wave. In our case, the scattering angle, θ , is about 14° , the correlation distance, a , is about 10 km and the angular frequency is 2π . The geometrical spreading factor, $G(r)$, is obtained from the usual ray techniques (*Červený, 2001*). Plugging in these values, equation (2) can be combined with equation (1) to yield a relationship with just 2 free parameters: the scattering volume V and the r.m.s. P wave velocity contrast $\delta\alpha/\alpha_0$. To remove uncertainties in the source and receiver effect, as well as the instrument response, we computed the amplitude ratio between $P.PKP_{CD}$ and PKP_{DF} . At an epicentral distance of 156° , the observed amplitude ratio between $P.PKP_{CD}$ and PKP_{DF} is about 0.43 and corresponding theoretical amplitude ratio is $4.309 \times 10^{-4}(\delta\alpha/\alpha_0)^2V$ with V and $\delta\alpha/\alpha_0$ unknown. Equating the observed and theoretical values we get an implicit relation between V and $\delta\alpha/\alpha_0$ (Figure 3.8a).

Based solely on *Wu and Aki's* work (*Wu and Aki, 1985a,b*), there is always trade-off between the scattering volume and the velocity perturbation: a bigger scattering volume needs a smaller velocity perturbation to generate the same amplitude of the scattered wave; however, a large scattering volume should lead to a relatively long wave train of coda. For a small region, only a few rays will be able to sample it producing a smaller duration of the coda wave. Using a trial-and-error method, we computed synthetic envelopes for different suitable combinations of scattering volume and velocity perturbation, by considering all the possible down-going rays that were able to reach the heterogeneous medium and then arrive at the station. We assumed a cylindrical shape for the scattering region, and convolved in the ESTF with each terminal arrival before taking the envelope. Comparing the

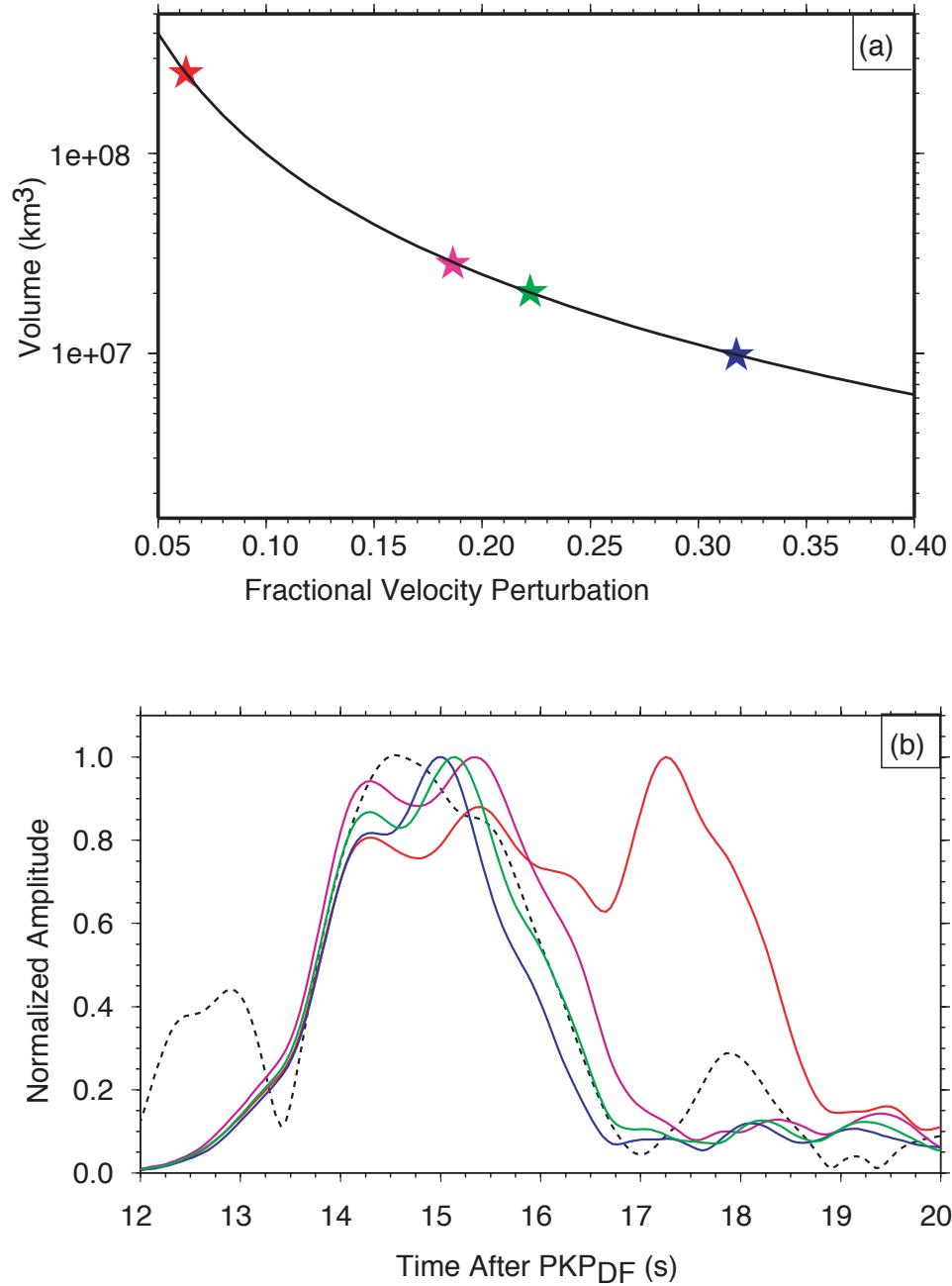


Figure 3.8: **(a)** Trade-off between scattering volume and fractional velocity perturbation. The black curve represents all possible volume-perturbation pairs that generate the observed amplitude of $P.PKP_{CD}$. The red, pink, green, and blue stars mark the position with 6%, 18%, 22%, and 31% P wave velocity perturbation, respectively. **(b)** Comparison between envelopes of PKP_{Cdiff} coda of data and synthetics generated for different volume-perturbation pairs. The black dashed line represents the real data, while the red, purple, green, and blue lines represent the synthetics for various levels of P wave velocity perturbation. The amplitudes are normalized to the maximum. The colors are consistent with those used in **(a)**.

synthetic envelopes with the data (Figure 3.8b), our best estimate of the velocity perturbation is about 18-31%, corresponding to an equivalent radius of ~ 150 km, if we imagine that the scattering volume is a cylinder with equal radius and height. It is important to point out that the way we calculate the synthetic envelopes is very rough since we do not know the shape of the anomalous region. However, under the single scattering theory, we believe the anomaly is very strong, with P wave velocity perturbation at least $\sim 15\%$.

3.5 Conclusions and Discussion

The magnitude of the velocity perturbation we infer is too large to be explained by chemical heterogeneity, and instead requires the existence of partial melt (*Williams and Garnero, 1996*). Furthermore, because at high pressure silicate melt is denser than the surrounding solid matrix (*Rigden et al., 1989*), it is unlikely that the scattering region we observe could exist anywhere except near the CMB. Here it has been suggested that dense partial melt raining down from above may be trapped by cumulus crystal growth (*Rost et al., 2005*). Partial melt at the CMB can also be caused by other means, such as enhanced heat flux from the core or viscous heating (*Steinbach and Yuen, 1997, 1999*), and its existence has been confirmed by experimental high pressure studies (*Holland and Ahrens, 1997; Zerr et al., 1998*). Hence, our preferred model is a partially molten region in the lowermost mantle beneath the Amazon River basin with a P wave velocity reduction of at least $\sim 15\%$. The precise shape of the region is virtually unconstrained, and it could be thin and broad in analogy with previously documented ULVZs.

The location of the scattering region found in this study (0.2°S and 56.9°W) is close to the newly discovered Atlantic Ridge plume (*Montelli et al., 2004*) at 12°N , 45°W . In that study, finite-frequency tomography results indicated the existence of a plume to a depth of at least 1900 km, however resolution was lost at deeper depths. And their 3-D image showed the plume tilted toward the south-west as it goes deeper (see Fig.S1 in their online supplemental material). Because the plume is rising in the convective mantle, it is expected that the plume may be tilted by the “mantle wind” on its way up (*Olson and Singer,*

1985). Global mantle convection models predict that the plume root can be offset horizontally more than 1000 km away from its surface location (*Steinberger and O'Connell, 1998*). Therefore, the Atlantic Ridge plume may actually originate at the CMB beneath the Amazon River basin, and tilt toward the north-east while it rises. A recent S-wave tomographic study (*Montelli et al., 2006*) confirmed its tilt direction (see their Fig.15), which is consistent with the result from P-wave tomography. Although no surface hot spot fed by this plume has been reported, a suggestion about an axial hot spot around this area has been made (*Sleep, 2002*).

This interpretation is consistent with similar seismic findings (*Garnero et al., 1998*), suggesting a link between extreme heterogeneity at the base of the mantle and upwelling plumes. For example, partial melt inferred to exist at the CMB north of Tonga (*Vidale and Hedlin, 1998; Wen and Helmberger, 1998*) is located very near the base of the tomographically imaged Samoa plume (*Montelli et al., 2004*). Likewise, partial melt inferred to exist at the CMB east of Australia is probably related to a trio of plumes near Tasmania (*Rost et al., 2005*). On a more general global scale, there is a statistically significant correlation between ULVZs at the CMB and hot spot surface locations (*Williams et al., 1998*). Therefore, it may be common for partial melt to exist in the lower mantle near the base of upwelling, thermal plumes.

Chapter 4

Using *PKP* Precursors Recorded at IMS Arrays to Determine the Small-scale Heterogeneity in the Mantle

It has been known that *PKP* precursors are direct evidence for the existence of small-scale, non-radially symmetric structure in the Earth's deep mantle since their re-interpretation in the 1970s. However, the scattering intensity, radial, and lateral distribution of the small-scale heterogeneities remain elusive. There are two possible reasons for the inconsistent results reported so far. One is related to the data used in different studies. Due to uneven data sampling and different data processing schemes, different authors may obtain different *PKP* precursor envelopes. The other possible reason may be related to differences in forward modeling methods. For the same data set, single-scattering theory may yield different results for heterogeneity strength than a multiple-scattering or diffusion-based theory. In this study, we take advantage of the globally distributed International Monitoring System (IMS) seismic arrays to assemble a large, geographically diverse dataset of *PKP* precursor envelopes. An advantage of using IMS arrays over single stations is that the recordings of all elements at one array can be coherently stacked to suppress noise, and thus provide high signal-to-noise (SNR) ratio *PKP* precursors, even for relatively small earthquakes. The average precursor amplitudes exhibit a steady increase with time and distance. We find that random heterogeneities with a scale-length of 8 km with 0.05% r.m.s. velocity perturbation uniformly distributed throughout the lower mantle can provide a reasonable fit to the observations. On the contrary, confining the heterogeneities near the CMB or in the D'' layer does not yield the amplitude versus time pattern observed in our data. Extra scattering near the CMB or in D'' is not justified from our data. We also find that the precursors' amplitudes vary from place to place. Some places such as off-shore of South America, the

southern part of the Atlantic Ocean, and central America, have weaker or similar precursors compared to the average precursor. The distribution of stronger precursor amplitudes is scattered. Even within a small geographic region, such as North America, the precursor amplitudes exhibit small-scale lateral variations. This implies that the lower mantle is not perfectly mixed by mantle convection and subducted oceanic lithosphere or other chemical impurities can survive in the mantle for billions of years.

4.1 Introduction

With the increasing high-quality seismic data and the improvements of seismic imaging techniques, we are obtaining a more and more detailed image of the Earth's interior. Not only is the radial seismic velocity structure well determined, but the non-radial large-scale heterogeneities have also been revealed, such as penetrating slabs and upwelling plumes. These findings are very important to understand mantle dynamics. Most of the discoveries are achieved by analyzing travel times and waveforms of the main seismic phases through tomography. However, resolving small-scale heterogeneity (with a scale length of 5-10 km) in the deep Earth is beyond the resolution of traditional seismic tomography because of spatial aliasing and contamination of the scattered waves by the strong heterogeneity in the upper part of the mantle.

High-frequency coda waves following P or S wave are the direct evidence for small-scale random heterogeneity in the Earth. *Aki* (1969) first showed that the scattered coda waves, which used to be treated as noise, can be used to estimate the strength of the random heterogeneity. Observations of PKP precursors concluded that small-scale heterogeneity must also exist in the deep mantle (*Doornbos and Husebye, 1972; Cleary and Haddon, 1972*). In order to obtain a fine image of the small-scale heterogeneity, which would lead to better understand mantle dynamics, we must carefully analyze high-frequency scattered waves.

PKP precursors have unique advantages in studying the deep Earth scatterers, as they are not contaminated by the direct arrivals and later-arriving scattered waves created by shallow structure. The sharp velocity decrease from the mantle to the core causes a P -wave

shadow zone at 105° - 143° (*Oldham*, 1906) and the first arrival is the *PKP* wave refracted in the inner core (*Lehmann*, 1936). Geometrical ray theory predicts no arrivals before *PKP* for a radially symmetric Earth model. However, when non-radial small-scale heterogeneities exist in the lower mantle, scattered energy from the outer core phase (*PKPab* or *PKPbc*) can arrive up to 18 s earlier than *PKP* in the range of 120° – 143° (Figure 4.1). This type of scattered energy preceding *PKP* was first observed in 1934 (*Gutenberg and Richter*, 1934). Older studies of the *PKP* precursors had controversy about their origin, including refraction in the inner core (*Gutenberg*, 1957), refraction or reflection in a transition layer between the outer and inner cores (*Bolt*, 1962; *Sacks and Saa*, 1969), and diffraction from the CMB (*Bullen and Burke-Gaffney*, 1958). However, it is now widely accepted that *PKP* precursors are generated by the scattering from volumetric inhomogeneities near the CMB or within the lower mantle, or from CMB topography (*Doornbos and Husebye*, 1972; *Cleary and Haddon*, 1972; *Bataille et al.*, 1990).

Since *Cleary and Haddon* (1972) showed that the precursors' travel times were consistent with those of singly scattered waves from irregularities near the CMB, numerous authors have focused on the scatterers' locations, their radial and lateral variations, and their magnitude. Several studies investigated *PKP* precursors recorded at some particular locations and inferred anomalously strong heterogeneities in the lowermost mantle underneath the source or receiver side (e.g. *Vidale and Hedlin*, 1998; *Wen and Helmberger*, 1998; *Wen*, 2000; *Niu and Wen*, 2001b). *Vidale and Hedlin* (1998) observed anomalously large *PKP* precursors from earthquakes in northern Tonga and inferred 10 – 15% r.m.s. velocity variation in a layer about 60 km thick near the CMB, supporting the presence of partial melt. By using short and long period *PKP* precursors, *Wen and Helmberger* (1998) also found evidence for the partial melt in a region 60-80 km in height, with at least 7% r.m.s. velocity perturbation beneath the Western Pacific. A few studies concentrated on modeling the time- and distance-dependent amplitudes of global average *PKP* precursors using single or multiple scattering theory (e.g. *Hedlin et al.*, 1997; *Shearer et al.*, 1998; *Cormier*, 1999; *Hedlin and Shearer*, 2000; *Margerin and Nolet*, 2003b). *Hedlin et al.* (1997) modeled the globally averaged *PKP* precursors using single-scattering theory and found the best model to fit the observations has $\sim 1\%$ r.m.s. velocity heterogeneity at a 8 km scale length

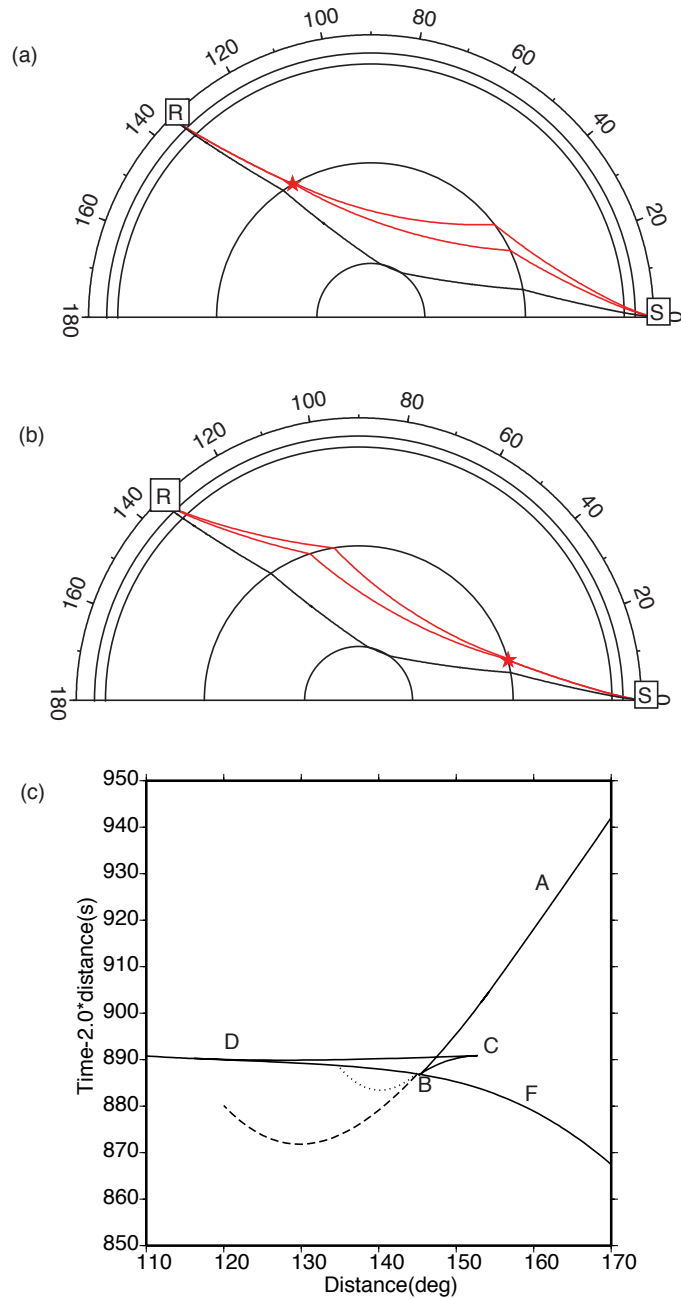


Figure 4.1: Ray paths and reduced travel time curves for the core phases and precursors. **(a)** The ray path for $PKIKP$ (black curve) and two PKP precursors (red curves) at 135° for a receiver side scatterer (red star) at the CMB. **(b)** Same as **(a)**, but for a scatterer located beneath the source side. **(c)** The solid curve is the standard PKP travel time curve in PREM, the dashed curve is the earliest precursor time when the scatterer is at the CMB, and the dotted curve is the earliest precursor time when the scatterer is 900 km above the CMB.

throughout the lower mantle. Using a revised single-scattering theory (Cormier, 1995) allowing for arbitrary levels of velocity and density perturbations, Cormier (1999) confirmed this conclusion by modeling the same dataset processed by Hedlin *et al.* (1997). However, by rejecting seismograms with no clear indications of *PKP* precursors in Hedlin *et al.* (1997)'s dataset and adding new ones from new deep events, Margerin and Nolet (2003a) used radiative transfer theory (Margerin and Nolet, 2003b) to model precursor envelopes and favored whole-mantle scattering with 0.1 – 0.2% velocity perturbations.

The basic mechanism of generating *PKP* precursors is now fairly well understood, however, the radial and lateral distributions, and magnitude of the small-scale mantle heterogeneity are still not fully resolved. Modeling of global average precursors tends to favor the whole mantle scattering model instead of confining the heterogeneity near the CMB. However, the magnitude of *P*-wave velocity perturbation is as much as 10 times different among different studies. The discrepancy comes from two possible causes. One is the dataset used in different studies. Due to uneven data sampling and different data processing schemes, different authors may obtain different global average *PKP* precursor envelopes. The other possible reason relates to differences in forward modeling theory. For the same precursors, single-scattering theory may yield different magnitudes of heterogeneity than a multiple-scattering or diffusion based theory. It is interesting to note that Margerin and Nolet (2003b) only selected those seismograms with strong precursors and obtained a velocity perturbation one order of magnitude smaller than that of Hedlin *et al.* (1997), who included data without strong precursors. Under the same forward modeling theory, Margerin and Nolet (2003b) are expected to obtain larger velocity perturbation than Hedlin *et al.* (1997). Therefore, a potential cause for the discrepancy is a difference between the single-scattering theory and transport theory. However, in another manuscript, Margerin and Nolet (2003a) showed that single-scattering and transport theories are essentially equivalent for perturbations less than 0.5%, and for large perturbations (1% or more), the two theories yield significantly different results. Since Margerin and Nolet (2003b) obtained 0.1 – 0.2% velocity perturbation, the scattering theories cannot explain the discrepancy. Therefore, the possibility that they obtained different average precursor envelopes due to using different data processing schemes cannot be excluded. With respect to the lateral variations of small-

scale mantle heterogeneity, there is only one complete study which was devoted to mapping out the large-scale variations (*Hedlin and Shearer, 2000*), while several individual studies inferred very strong heterogeneity near the CMB at some particular geographic locations (*Vidale and Hedlin, 1998; Wen and Helmberger, 1998; Wen, 2000; Niu and Wen, 2001b*).

In this study, we assemble a large, geographically diverse data set of *PKP* precursor envelopes by using the globally distributed international monitoring system (IMS) seismic arrays. An advantage of using arrays over single stations is that the recordings of all elements at one array can be coherently stacked to suppress noise, and thus obtain high signal-to-noise (SNR) ratio *PKP* precursors, even for relatively small earthquakes. We then apply a Monte Carlo seismic phonon method to model the global averaged *PKP* precursor envelopes to define the small-scale heterogeneity scattering model in the mantle. Lateral variations of small-scale heterogeneity will be discussed to better understand its distribution and nature.

4.2 Data Processing

The mission of the International Monitoring System (IMS) is to monitor the world for nuclear tests. A large portion of IMS seismic stations are small aperture arrays (with aperture from 4-25 km) equipped with 10-20 short-period vertical component seismometers in each array. Most of the IMS seismic data before December 2003 are freely available from the U. S. Army Space and Missile Defense Command (SMDC) Monitoring Research Program (MRP) website. Data from IMS arrays within the U.S., including PDAR, TXAR, ILAR and NVAR, are available from May 2000 until present at IRIS DMC. Continuous seismic data from the Yellowknife array (YKA) since 1989 can be requested from Canadian National Data Centre (CNDC) through AutoDRM. We searched the global CMT catalog to find the events at source-receiver distance between 120° and 145° with moment magnitude greater than 4.5 for each IMS array during the open time period. We checked over 9000 events recorded at 11 IMS seismic arrays in the proper distance range. For each event, the seismograms were visually inspected for the quality. We selected those events which have clear and impulsive *PKP* waves and high SNRs, regardless of precursor amplitudes. For

each good event, the obviously noisy or glitchy traces are removed. A total of 2,223 events (over 30,000 traces) recorded at 11 seismic arrays are selected for subsequent processing and analysis. Table 4.1 lists the properties of all the IMS arrays used in this study and the number of events selected for each array. Figure 4.2 shows the locations of the 11 IMS arrays and the entry and exit points at the CMB of PKP waves under the receiver and source sides of the selected events.

Table 4.1: IMS seismic arrays used and the number of events selected

Seismic Array	Lat °N	Lon °E	Number of Elements	Aperture ^a km	Events Selected
ARCES	69.535	25.506	23	3.7	247
ASAR	-23.665	133.951	19	9.8	216
CMAR	18.420	98.959	18	11.0	91
ESDC	39.671	-3.946	19	9.4	32
GERES	48.837	13.702	25	4.1	240
KSAR	37.447	127.894	19	10.8	40
NVAR	38.429	-118.303	11	9.9	171
PDAR	42.777	-109.583	13	3.4	285
TXAR	29.334	-103.667	9	4.5	572
WRA	-19.767	134.393	20	23.9	114
YKA	62.606	-114.605	18	24.2	215

^a We use the definition from *Koper et al.* (2003) as the diameter of the circle that has the same area as the smallest rectangle that includes all the elements.

To determine the global average precursor amplitudes, we process the data in the following four steps.

First, for each event, we bandpass filter the seismograms between 0.7 and 2.5 Hz since the dominant frequency of the precursor is 1-2 Hz. This frequency band can resolve small-scale heterogeneities with a scale length of about 5-10 km.

Second, instead of calculating envelope functions of individual traces, as in previous precursor studies which used data from single stations, we apply the sliding window, time-domain beamforming to the seismograms recorded at the array to obtain the amplitude maximum, slowness, back azimuth and coherence versus the lapse time (*Koper, 2005*), which is equivalent to the sliding window frequency-wavenumber (fk) analysis developed

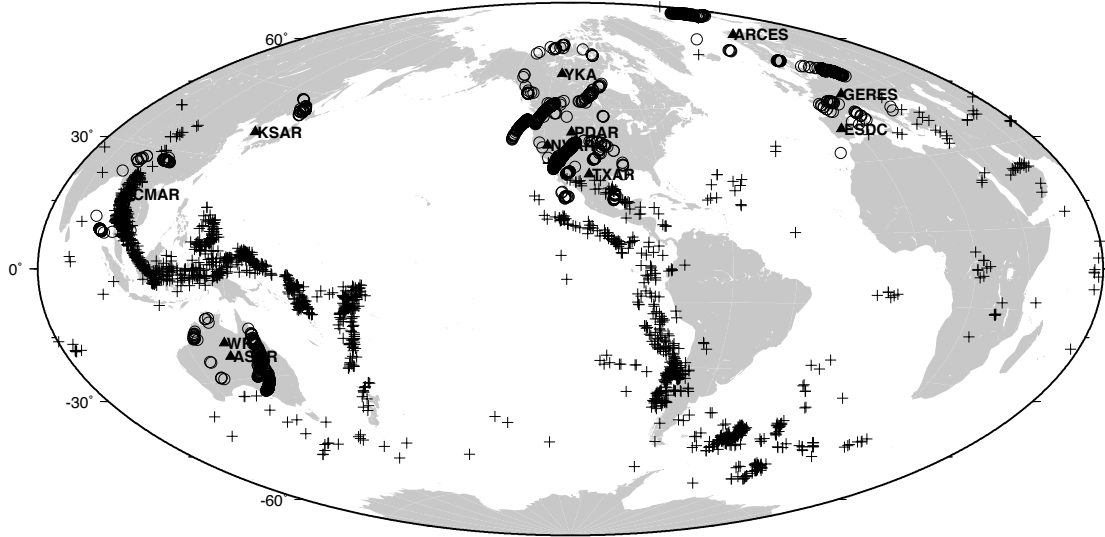


Figure 4.2: Locations of the 11 IMS arrays and the *PKIKP* entry and exit points at the CMB. Black triangles are IMS arrays. Circles and pluses are the entry and exit points of *PKIKP* at the CMB under the receiver side and source side.

by *Rost and Weber (2001)*. For a short time window with a fixed length of 1 s, we perform a grid search over all the possible slowness and back azimuth combinations to find the amplitude maximum. Then the fixed-length short time window is shifted along the seismograms with a constant step of 0.2 s, and we perform the same grid search for the best combination of slowness and azimuth. At each step, the power maximum, slowness, back azimuth and coherence are stored as time series. The sliding window beamforming instead of the simple beamforming at a fixed slowness (*PKP* slowness) is selected because the simple beamforming may under-estimate the precursor's amplitude due to its different slowness from *PKP*. The choices of the 1 s search time window and the 0.2 s shift step are based on the dominant period of the precursors and the size of the seismic arrays. The precursor has a dominant period of 0.5-1 s, so the time window should be long enough to include the complete signals across the array for a particular phase, while being short enough to avoid multiple phases with different slownesses appearing in the same time window, causing the ambiguity of identifying a single phase. In this manner, we obtain a high SNR and accurate estimate of *PKP* precursor's amplitude for each event, which has much higher quality than the recording at one single station. Figure 4.3 shows an example of this type of sliding window beamforming analysis for an event recorded at the YKA array.

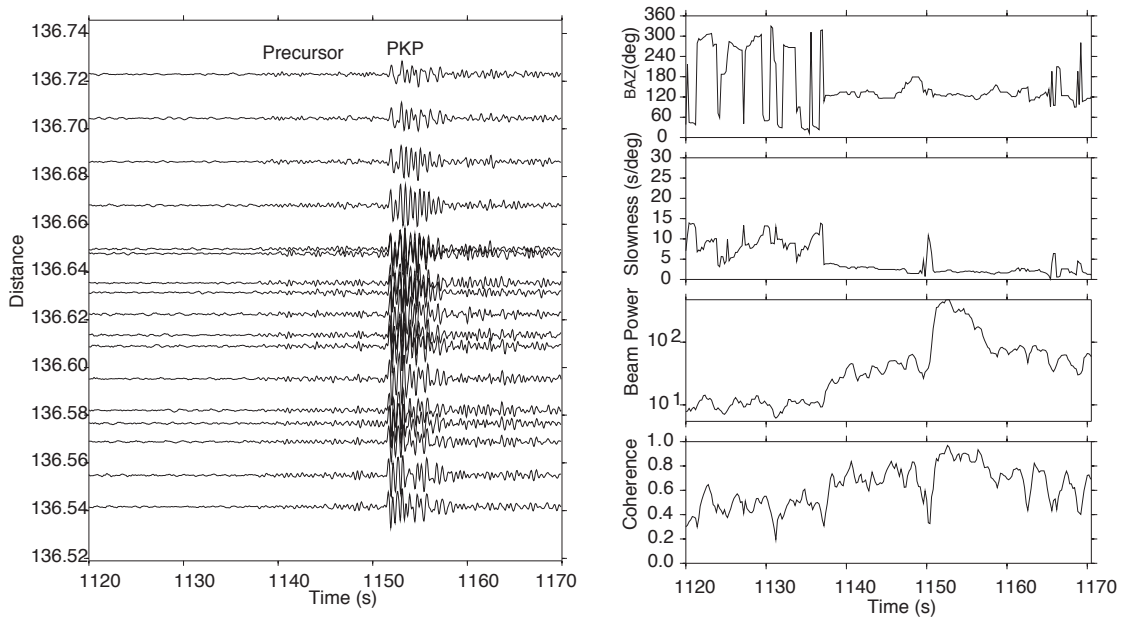


Figure 4.3: Vertical record section of an example event and its sliding window slowness analysis. **(Left)** Vertical component record section for an event with moment magnitude 5.3 at 82.8 km depth recorded at the YKA array. The seismograms have been bandpassed at 0.7-2.5 Hz with a 3-pole Butterworth filter. *PKP* waves arrive at about 1152 s and precursors can be clearly seen in the ~ 10 s time window before *PKP*. **(Right)** From top to bottom are the back-azimuth, slowness, power and coherence measured from the sliding window algorithm. Precursory energy is clearly seen from the beam power plot about 10 s before *PKP*. In the same time window, the back-azimuth and slowness are stable, and the coherence is higher than the background noise.

The third step of our data processing is that we apply a smoothing algorithm with width of 1 s (5 points) to smooth the power function (we use the term envelope to refer to it for simplicity, although it is slightly different from the common definition of an envelope) of each event obtained at the second step. For the smoothed envelope, we search for the peak amplitude within a time window of ± 5 s w.r.t. the predicted *PKP* arrival time in AK135 Earth model. Then we use the time corresponding to the peak amplitude as a reference and search for the first local maximum with amplitude $\geq 60\%$ of the global maximum amplitude. If there is a local maximum within this criteria, we use the time corresponding to the local maximum as the actual *PKP* peak arrival time. Otherwise, we use the time corresponding to the global maximum amplitude as the actual *PKP* peak arrival time. 60% is selected to do this search to find the actual *PKP* peak arrival time based on the following two considerations. First, the precursor's amplitude is usually less than 50% of the amplitude of *PKP* wave from previous studies (*Hedlin et al.*, 1997; *Bataille and Flatte*, 1988) and we do not observe any precursor with amplitude greater than that either. Therefore, using 60% as the criterion permits us to find the *PKP* time instead of the precursor time. Secondly, *PKiKP* arriving a little after *PKIKP* sometimes may have bigger amplitude than *PKIKP* although the predicted amplitude ratio between *PKIKP* and *PKiKP* is around 1 (*Cao et al.*, 2007). In this case, the global maximum amplitude may correspond to *PKiKP*. Therefore, searching for the first local maximum can enable us to find the *PKIKP* arrival time we intend to use as the reference for stacking. Finally, for the shallow events, the depth phase *pPKP* arriving a few seconds after *PKP* sometimes has slightly larger amplitude than *PKP*, although the ray path and radiation pattern coefficient are very close for the two phases. Thus, searching for the first local maximum gives us a better chance to find the *PKP* time instead of *pPKP* arrival time.

Finally, we use a 20 s time window starting from 45 s before *PKP* to estimate the noise level. SNR is defined to be the ratio between the *PKP* peak amplitude and the noise level. We then subtract the noise level from the envelope function and stack the envelopes from different events with $\text{SNR} \geq 10$ in 1° distance bins after aligning and normalizing the envelope functions according to the estimated *PKP* peak arrival time and amplitude. The stacked global average precursors' amplitudes increase with time and distance as shown in

Figure 4.4.

To test the robustness of our average precursors' amplitudes, we took a random half of our data set and applied the same stacking method, which yields a very similar result as the whole data set. It is important to note that within each 1° distance bin, *PKP* precursors' amplitudes exhibit a lot of variation from event to event. This will be discussed later.

4.3 Modeling Global Average *PKP* Precursor Envelopes

To model the scattering of random heterogeneity in the Earth, both single-scattering and multiple-scattering theories have been used to compute the synthetic scattered waves' envelopes (for a review, see *Sato and Fehler* (1998)). When the velocity and density perturbations of the heterogeneity are much weaker than those of background media, the Born approximation is valid and single-scattering theory may be sufficient to model the scattering phenomenon. Otherwise, a multiple-scattering approach is necessary to simulate the scattered wave field. Most multiple-scattering approaches are based on radiative transfer theory (*Wu and Aki*, 1985a,b; *Sato and Fehler*, 1998; *Margerin and Nolet*, 2003a). By using the Monte Carlo simulation based on radiative transfer theory, *Margerin and Nolet* (2003a) found that the Born approximation is only valid for the r.m.s velocity perturbation $\leq 0.5\%$.

In this study, we use a particle-based Monte Carlo method developed by *Shearer and Earle* (2004) to model the globally averaged *PKP* precursor amplitude. In this particle-based simulation, millions of particles (seismic phonons) are sprayed from the source, which are randomly scattered using probabilities computed from random media theories (*Shearer and Earle*, 2004). In this algorithm, the multiple-scattering is naturally implemented and intrinsic attenuation is included. We apply the seismic phonon method to a standard Earth model PREM with random heterogeneities at different depth ranges in the mantle. We assume an exponential autocorrelation function for the random media with variable scale-length and r.m.s. velocity perturbation to model the observed globally averaged *PKP* precursor envelopes.

Since only a small fraction of precursors are affected by upper mantle scattering (Figure

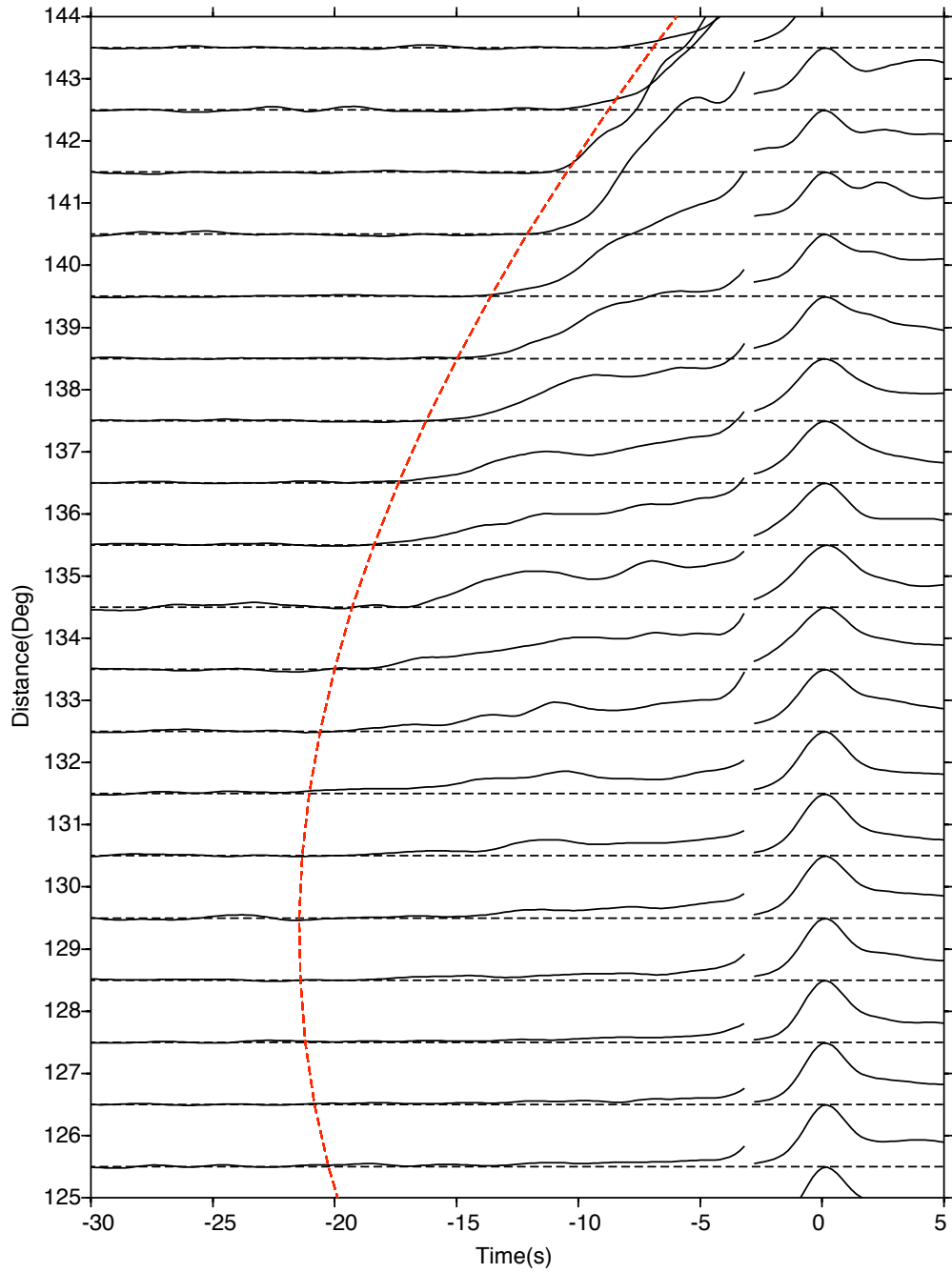


Figure 4.4: Average precursor amplitudes as a function of time and distance. Times are relative to the peak of PKP envelopes (shows at 0 s). Amplitudes before -2 s are magnified by a factor of 10. The envelope from each individual event is normalized according to the peak of PKP envelope before stacking. The red dotted curve across all the distances is the earliest precursor traveltimes curve when the scatterer is at the CMB.

4.1), we will not try to constrain the scattering strength in the crust and upper mantle and instead we use the fixed scattering model for this portion of the Earth obtained by *Shearer and Earle* (2004) in our modelling process. In addition the inner core scattering has no effect on the precursor but only modifies the reference phase *PKP*'s amplitude. Therefore, we will not attempt to constrain the inner core scattering either, and instead use the preferred inner core scattering model obtained by *Peng et al.* (2007).

We first confine the small-scale heterogeneities in a 20 km thick layer just above the CMB. However, as pointed out in previous studies (*Hedlin et al.*, 1997; *Shearer et al.*, 1998), in this case the precursors' amplitude increases with time for the first few seconds and then stabilizes quickly until the *PKP* arrival, which is inconsistent with our observations (Figure 4.5). The amplitudes do not stabilize as fast as in the synthetic experiments done by *Hedlin et al.* (1997) and *Shearer et al.* (1998) since we also include upper mantle scattering which contributes precursor wavefield at 2-5 s before *PKP* after a distance 130°.

In order to fit the observed amplitude versus time pattern, we increase the depth extent of mantle scattering to the D'' region (from the CMB to 200 km above). In this case, the amplitudes still increase with time for the first few seconds and then stabilizes quickly again (Figure 4.6). Even when we increase the depth extent of mantle scattering scatter from the CMB to 600 km above, the predicted precursor amplitude still does not exhibit the observed amplitude versus time feature (Figure 4.7). By experimenting with different scattering depth ranges, scale-lengths and r.m.s. velocity perturbations for the random media, we find that uniformly distributed heterogeneities with a scale-length of 8 km and 0.05% r.m.s perturbation in the whole lower mantle gives an overall reasonable fit to the observed precursors (Figure 4.8). We also find that extra scattering near the CMB or in D'' is not necessary in order to fit our data. For example, when we increase the r.m.s. perturbation in the D'' to 0.1%, the predicted precursor amplitudes are too big compared with our observations (Figure 4.9). When we change the r.m.s. perturbation near the CMB (from CMB to 20 km above) to 0.1%, the predicted precursors are almost the same as the uniform whole lower mantle scattering with 0.05% r.m.s. velocity perturbation. However, when we raise the perturbation near the CMB to 0.2%, the predicted precursor amplitudes

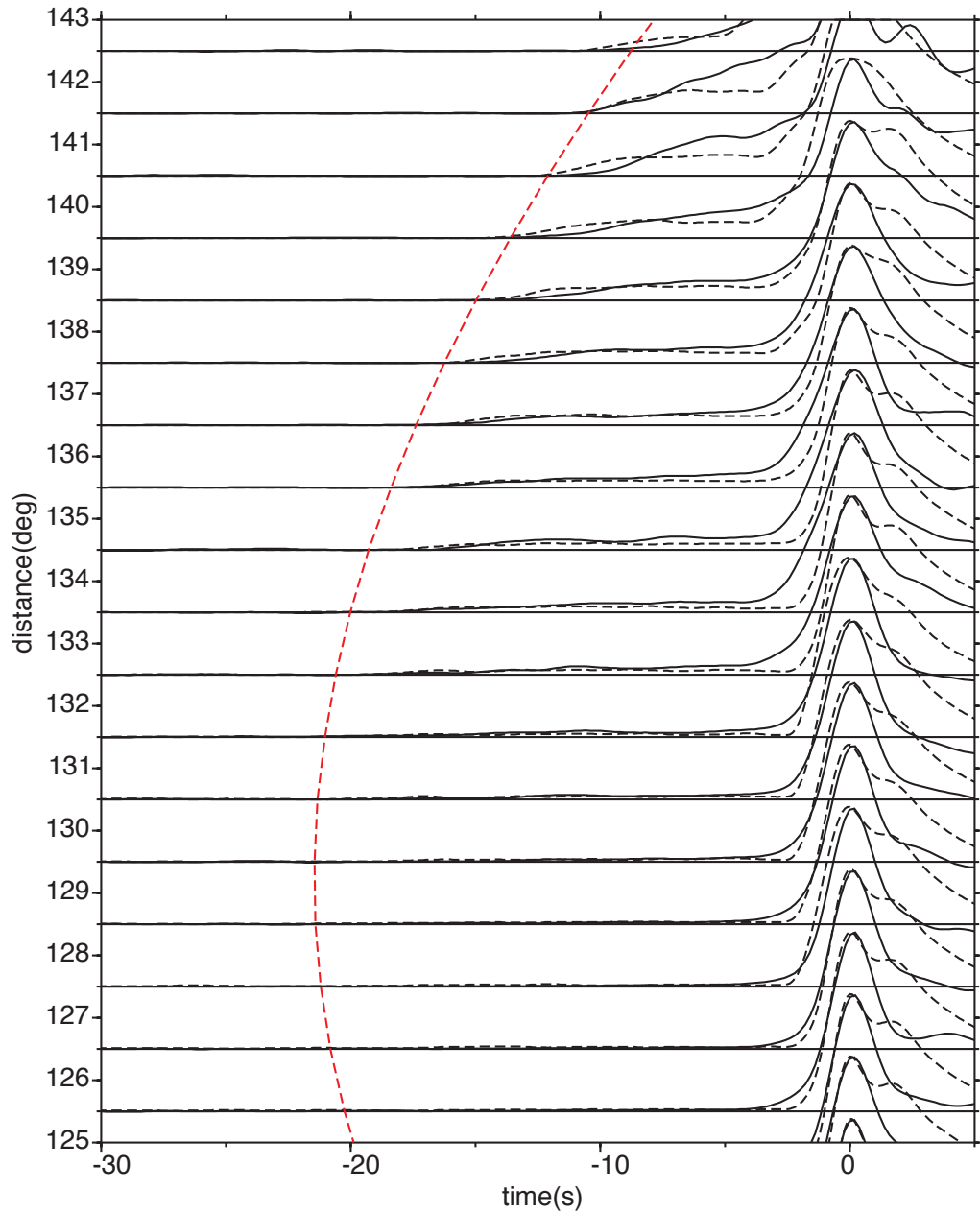


Figure 4.5: Comparison of observed precursors (solid) and those predicted (dashed) for a model with 0.2% r.m.s. velocity perturbation confined to a 20 km thick layer just above the CMB. Times are relative to the peak of *PKP* envelopes (shown at 0 s). The dashed curve across all the distances is the earliest precursor traveltime curve when the scatterer is at the CMB. Those predicted precursors increase with time for the first few seconds and then stabilizes quickly until the *PKP* arrival, which is inconsistent with the observations.

are too big compared with our observations (Figure 4.10). Therefore, extra scattering in the D'' or near the CMB is not justified based on our observations and we believe that the CMB and D'' do not differ significantly than the rest of the lower mantle in terms of small-scale heterogeneities. This is consistent with previous results from modeling globally averaged precursor (*Hedlin et al., 1997*).

The estimate for the r.m.s. perturbation above is obtained by assuming the scale-length of the auto-correlation function of the random media to be 8 km. It is important to mention that there is always a trade-off between the assumed scale-length and the r.m.s. perturbation of the random media. A smaller scale-length will need a larger r.m.s. perturbation to achieve similar precursor amplitudes. For example, when we assume the scale-length to be 4 km, we obtain slightly smaller precursor amplitudes from the whole lower mantle scattering model with a 0.05% r.m.s. perturbation. Instead, a 0.07% r.m.s. perturbation with a 4 km scale length can fit our data reasonably well. On the contrary, when we assume the scale-length to be 16 km, a 0.04% r.m.s. perturbation provides reasonable fits. Modeling the precursors at different frequency bands may help to minimize this trade-off, however, the scale-length can not be too long since the precursors are most prominent at frequencies higher than 1.0 Hz. Results from assuming the scale-length to be 8 km only are presented here because it is comparable to the wavelength of the 1.0 Hz wave.

It is also important to point out that the inner core Q value will affect the r.m.s. perturbation estimate since it has a significant effect on the reference phase PKP amplitude. The results above are based on the inner core Q value of 360 from *Bhattacharyya et al. (1992)*. When we use an inner core Q value of 440 as in PREM (*Dziewonski and Anderson, 1981*), we found that the r.m.s. velocity perturbation a little bit higher than 0.06% in the lower mantle is needed to provide a reasonable fit to the observed precursor amplitude versus time pattern. Concerning the Q values in the crust and mantle, we find that they do not have a significant effect on our results since both the reference phase PKP and precursor travel through this region.

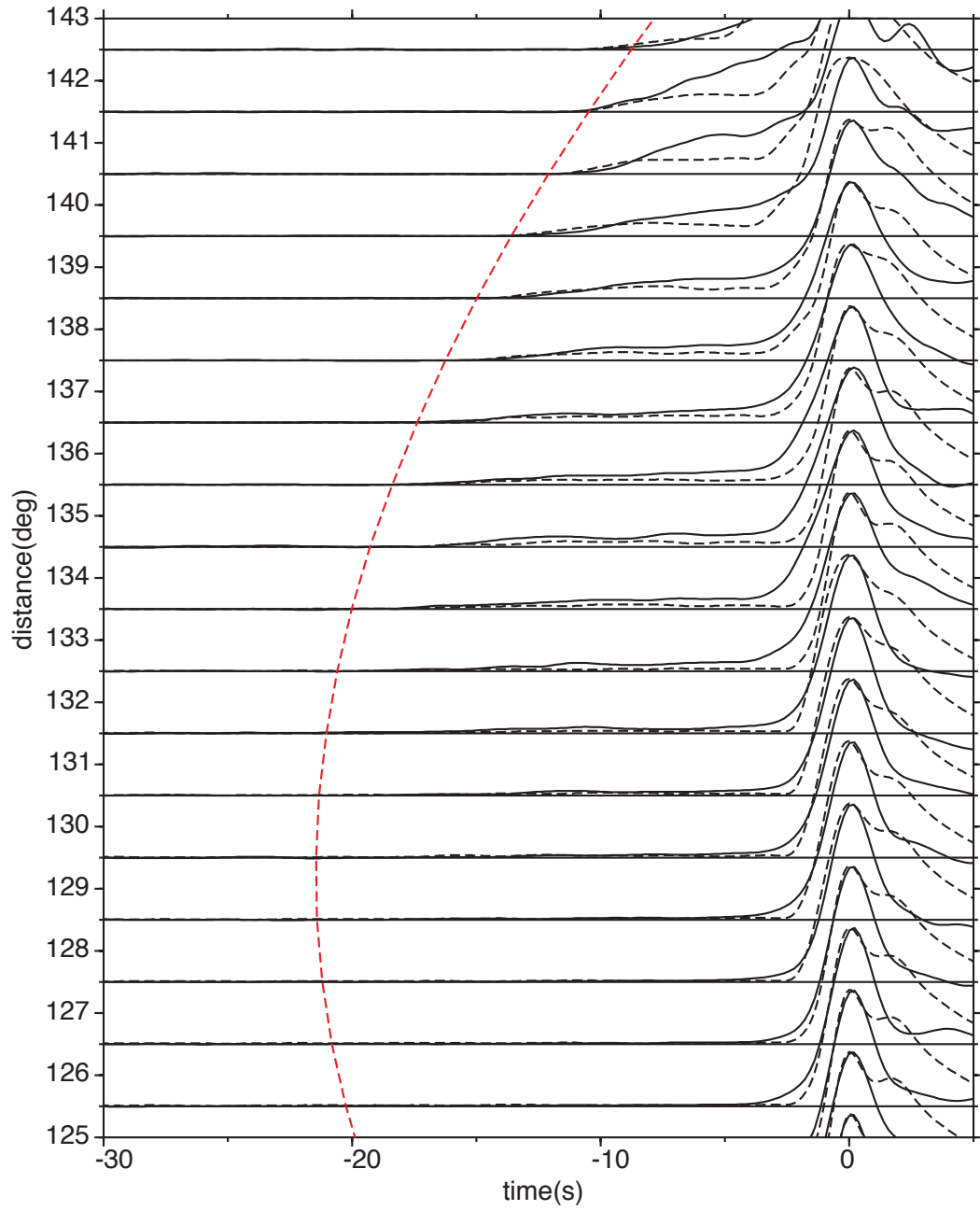


Figure 4.6: Same as 4.5, but for a model with 0.05% r.m.s. perturbation in the 200 km thick layer above the CMB.

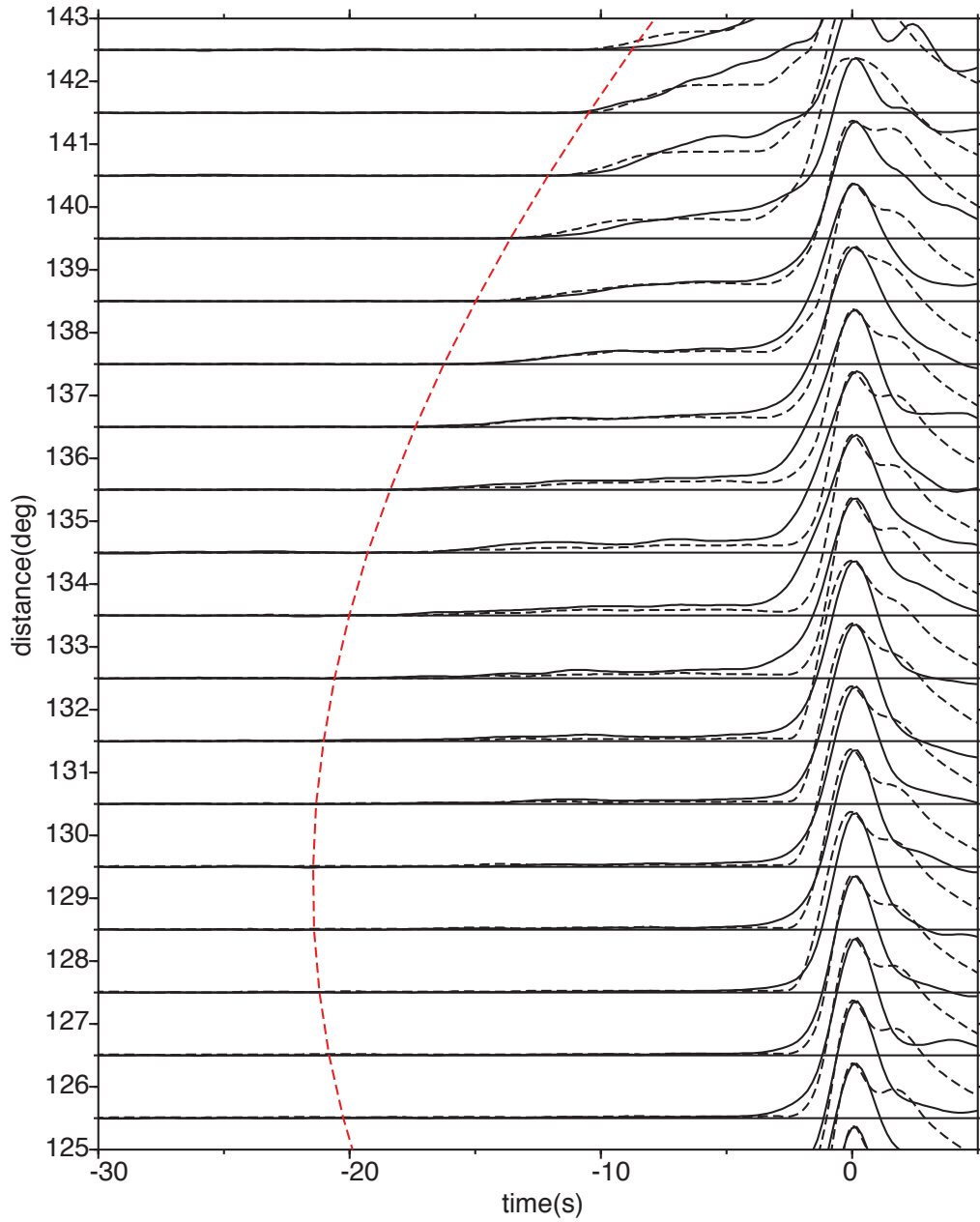


Figure 4.7: Same as 4.5, but for a model with 0.05% r.m.s. perturbation in the 600 km thick layer above the CMB. The predicted precursors still exhibit features that are not seen in the data.

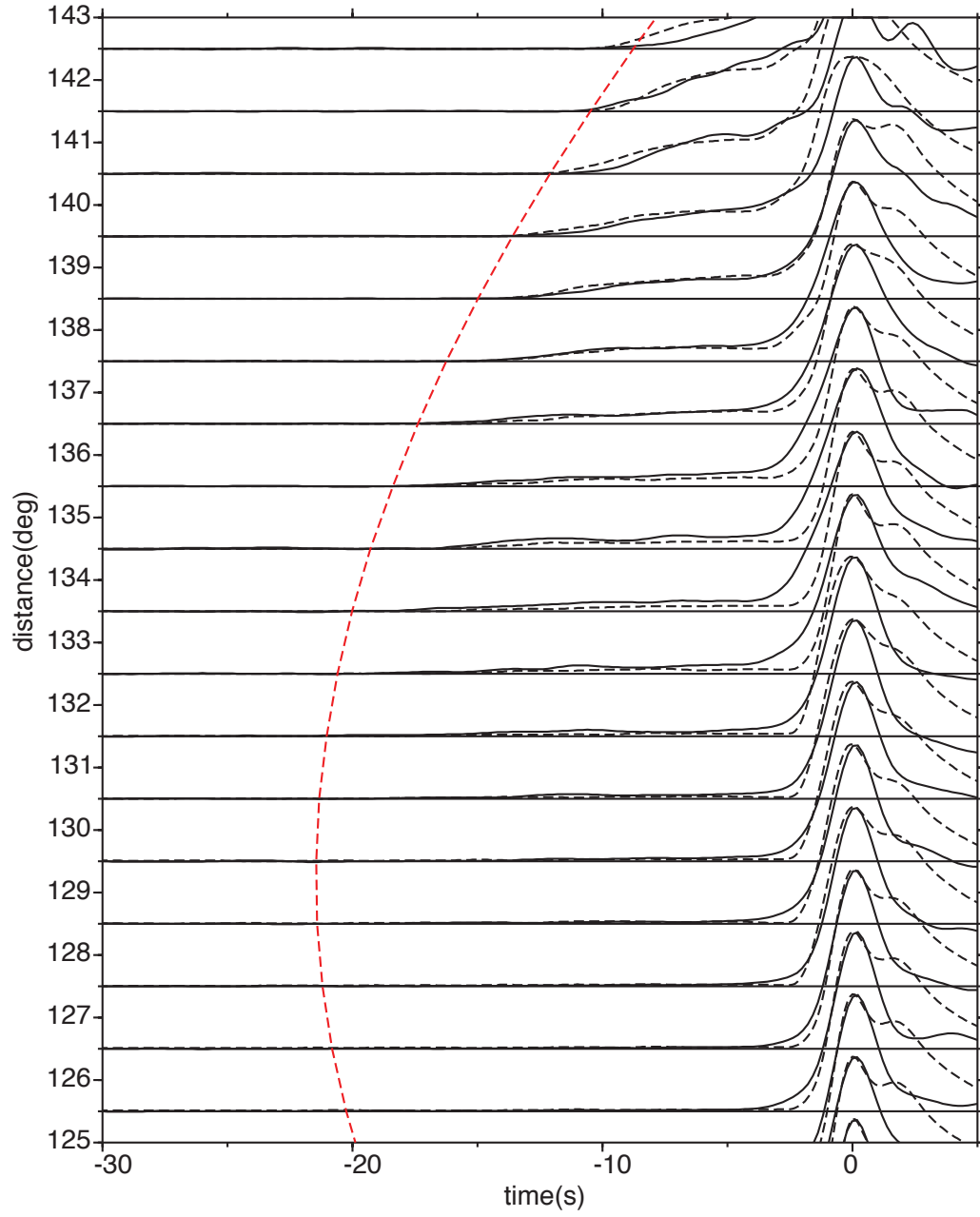


Figure 4.8: Same as 4.5, but for a model with scattering in the entire lower mantle with a 0.05% r.m.s. perturbation. This model does predict reasonable fits to the observations.

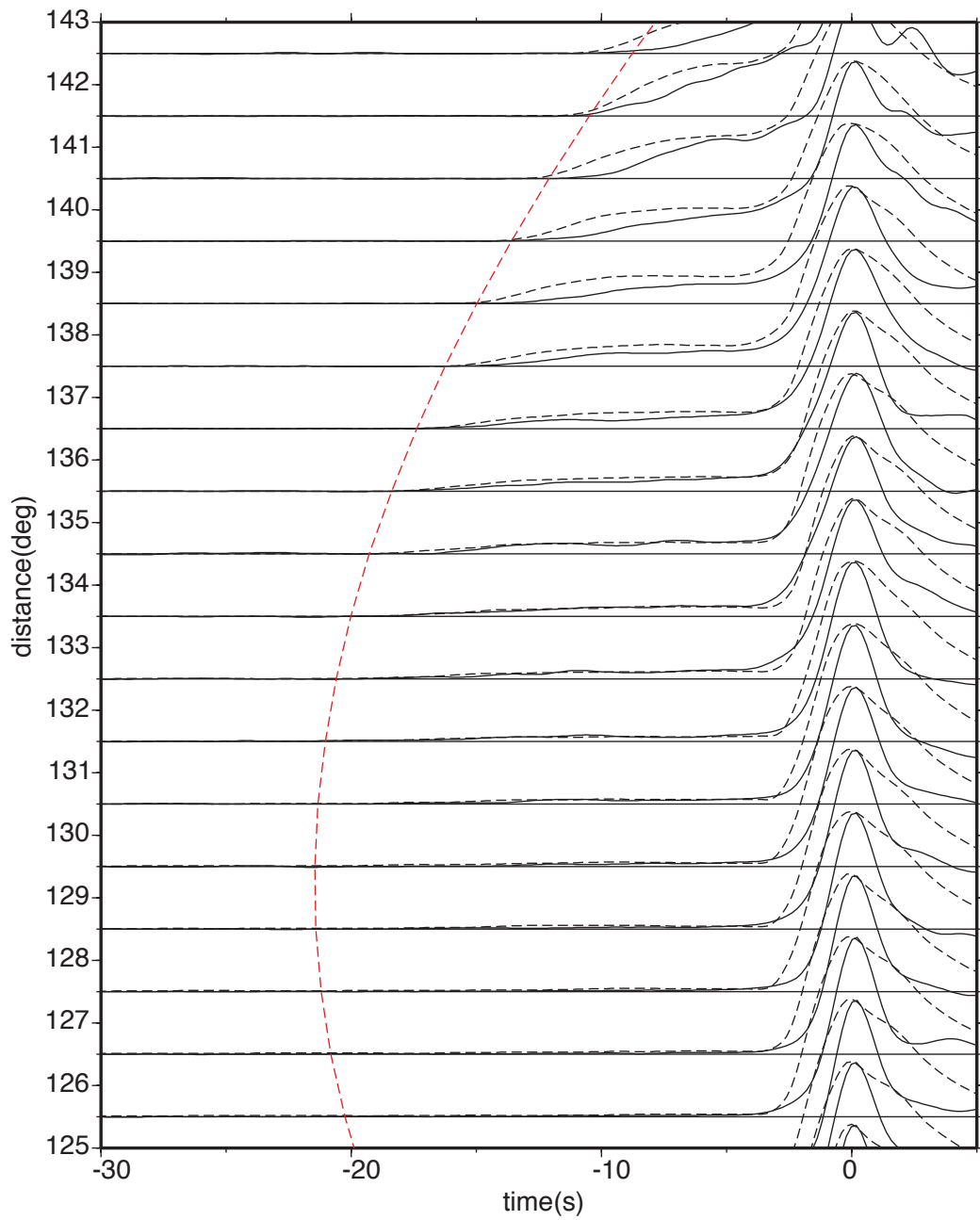


Figure 4.9: Same as 4.5, but the dashed curves are the predicted precursors from the whole lower mantle scattering model shown in Figure 4.8 plus 0.1% r.m.s. perturbation in a 200 km thick layer just above the CMB. Those predicted precursors are a little bit too large compared with the observations for the first few seconds of the precursor time window.

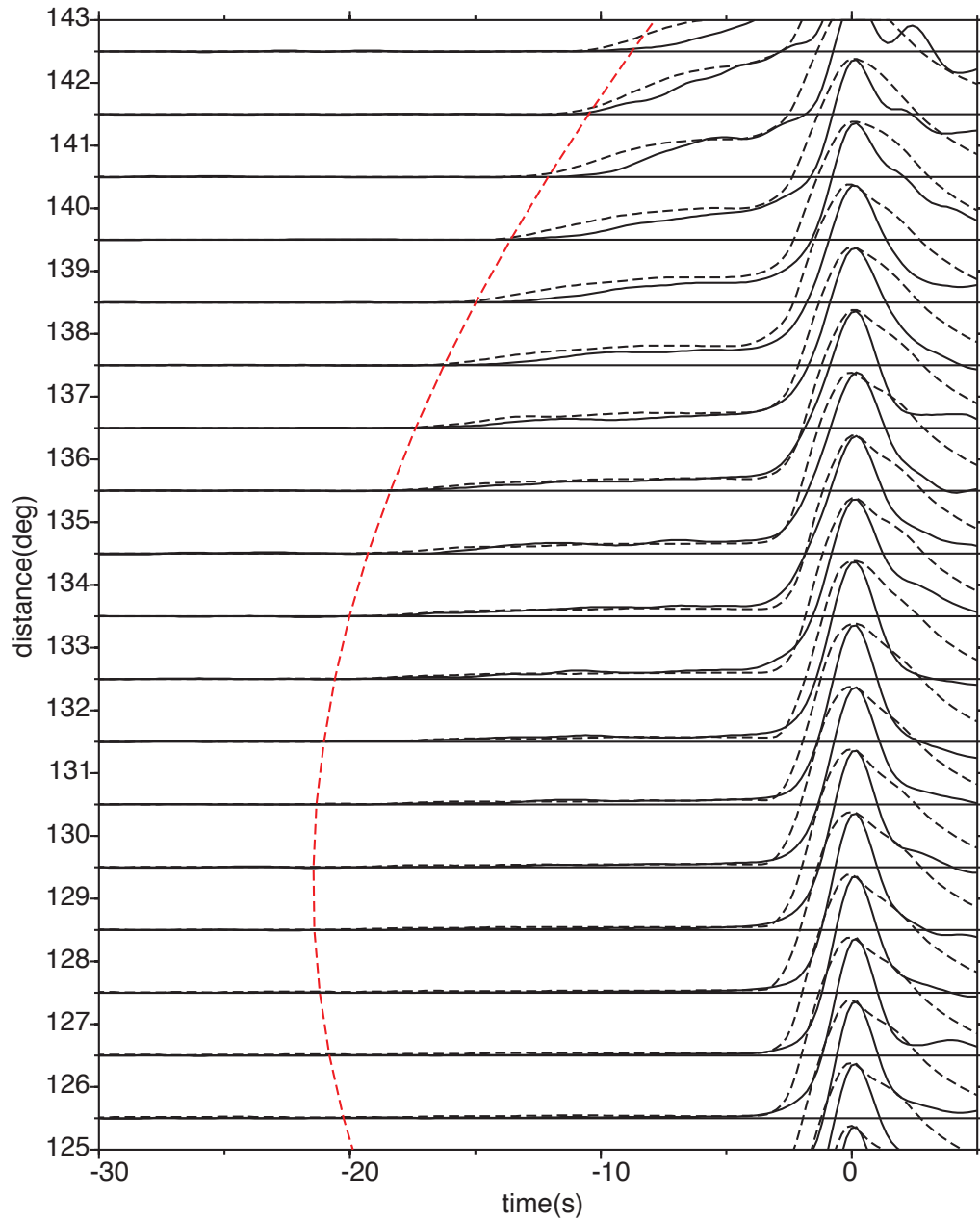


Figure 4.10: Same as 4.9, but the dashed curves are the predicted precursors from the whole lower mantle scattering model shown in Figure 4.8 plus 0.2% r.m.s. perturbation in a 20 km thick layer just above the CMB.

4.4 Regional Variations of PKP Precursor Amplitude

The PKP precursor amplitude exhibits large variations from event to event, which implies the small-scale heterogeneities are not uniformly distributed throughout the lower mantle, with stronger scattering in some places than others. Figure 4.11 shows the global average amplitude of PKP precursors and its standard deviation. At greater distances, the precursor amplitudes become larger, as do their deviations. Large standard deviations imply big variations in scattering strength from place to place. In order to map the geographic variations of PKP precursor amplitudes, we calculate the misfit between each individual envelope and the globally averaged envelope at its corresponding distance for the events with distances between 131° and 141° . At distances smaller than 131° , PKP precursors are insensitive to the lower mantle scattering and amplitudes are very small. At distances greater than 141° , PKP precursor amplitudes can be affected by the $PKP - B$ caustic.

Generally, PKP precursor energy can come from scatterers in the lower mantle under both the source-side and receiver-side. Although the slowness of the PKP precursor can help to clarify this ambiguity, unfortunately, our dataset collected from small aperture IMS arrays does not possess this capability. Therefore, our precursor amplitude strength distribution is somewhat messy and does not show consistent geographic feature due to the ambiguity between the source and receiver side scattering. However, when we plot the strong and weak precursor amplitudes (stronger or weaker than the global average precursor) separately (Figure 4.12), some consistent regional patterns can be identified. For the weak precursors, it is likely that the mantle beneath both the source and receiver sides has weak scattering. For the strong precursors, both the source and receiver sides are possible causes. Comparing the two panels in Figure 4.12, it is fairly robust that off-shore of South America and the southern part of the Atlantic ocean have weaker PKP precursor than the global average. Central America, Australia and the northern part of Southeast Asia are likely to have weaker or similar precursor compared to the global average precursor amplitude. The stronger precursor distribution is somewhat scattered around parts of North America, the southeast Asian islands, and the southern Pacific.

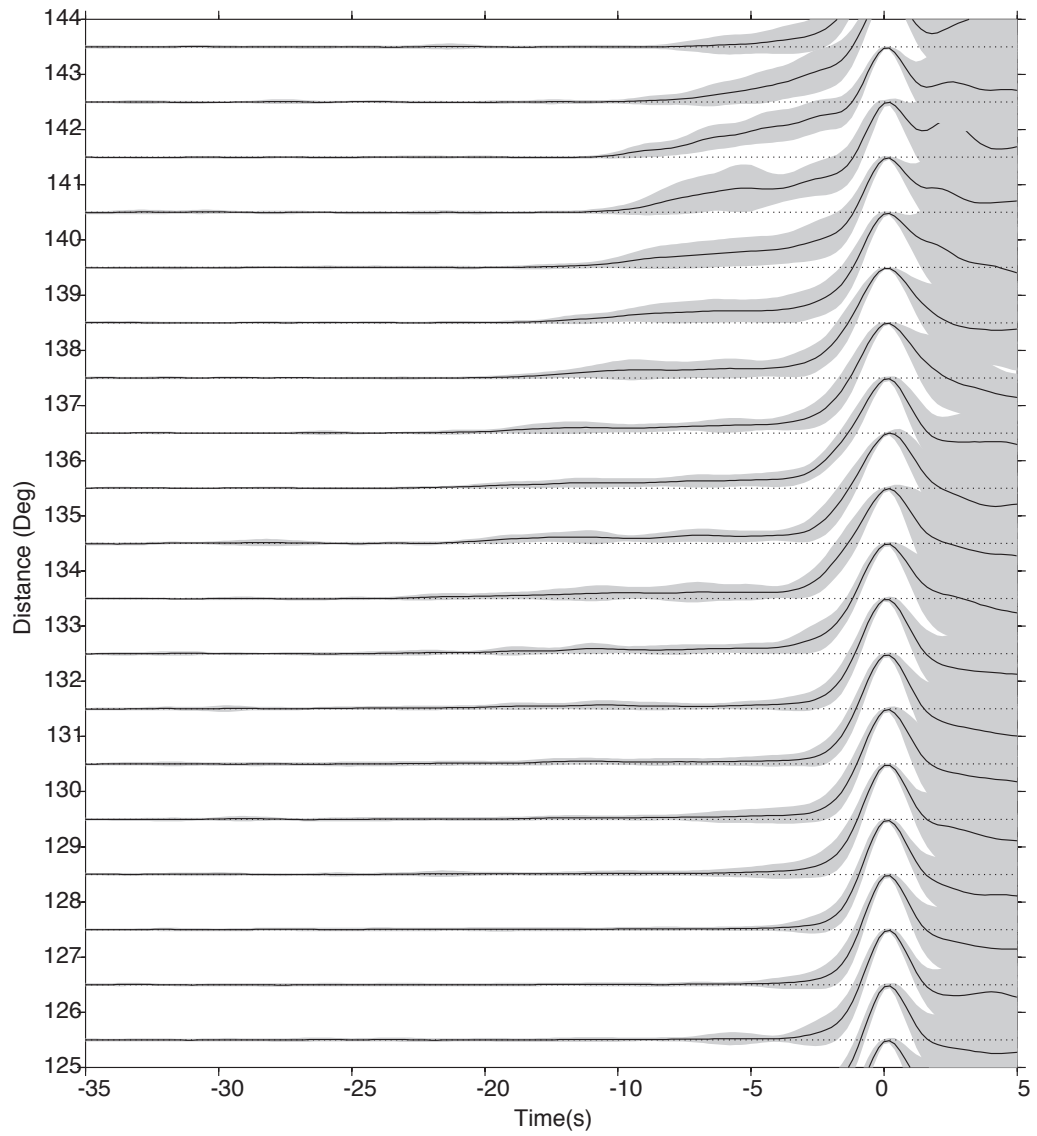


Figure 4.11: The standard deviations of the globally averaged precursors' amplitudes.

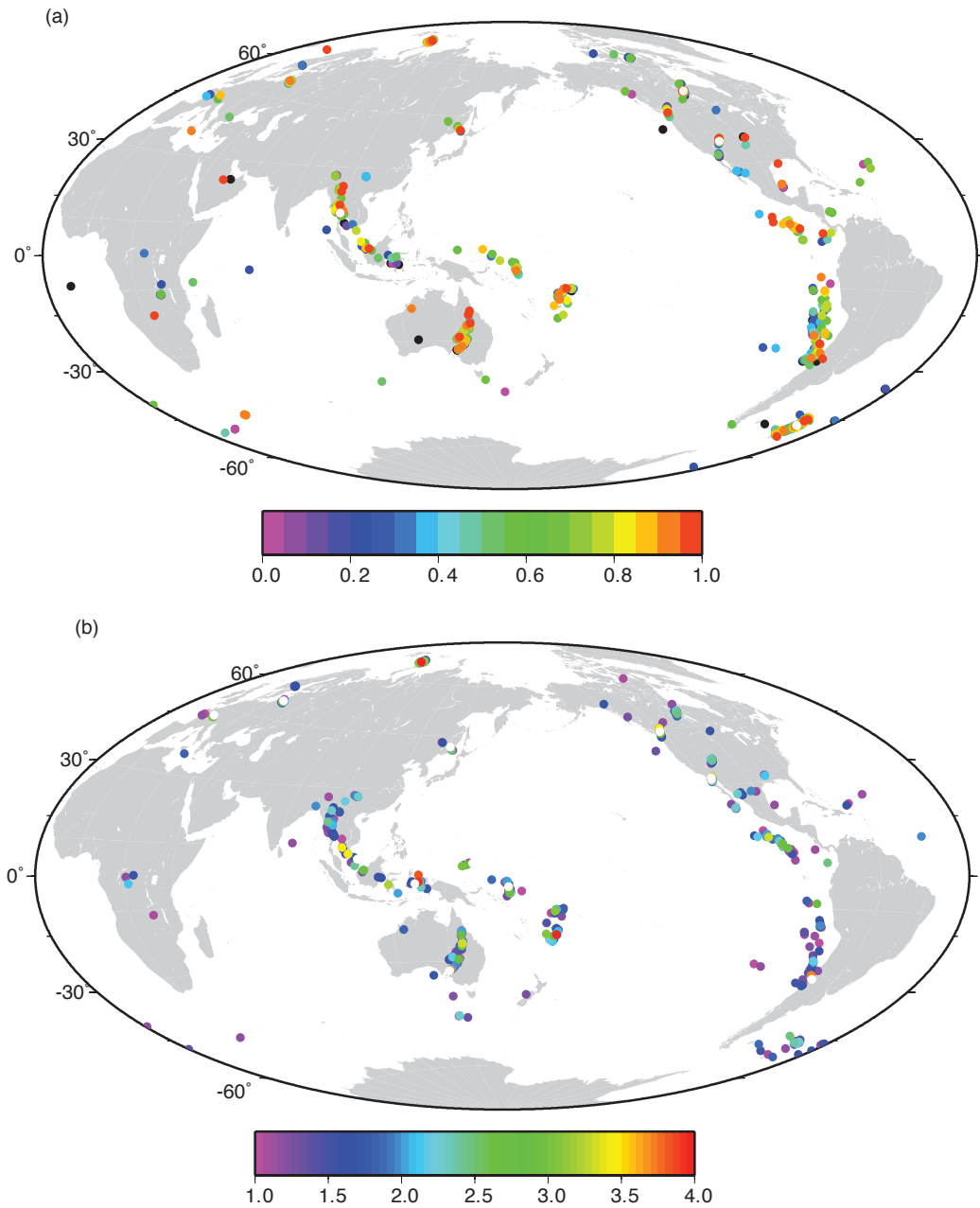


Figure 4.12: The geographical distribution of weak and strong precursors. The dots are the entry or exit points of $PKIKP$ waves at the CMB. The color scale represents the precursor amplitude ratios between individual precursor and the global average. **(a)** The geographical distribution of precursors weaker than the global average. **(b)** Same as **(a)**, but for precursors stronger than the global average.

4.5 Conclusions and Discussion

We have assembled a large, high-quality *PKP* precursor waveform dataset from short-period IMS seismic arrays. The observed average *PKP* precursor amplitudes gradually increase with time before the *PKP* arrivals and with distances at $124^\circ - 142^\circ$. We find that random heterogeneities with a scale-length of 8 km with 0.05% r.m.s. perturbation uniformly distributed throughout the lower mantle can provide a reasonable fit to the observations. On the contrary, confining the heterogeneities near the CMB or in D'' does not yield the amplitude versus time pattern as observed in our data. Extra scattering near the CMB or in D'' is not justified from our data. The r.m.s. velocity perturbation we find is much smaller than the previous result from modeling globally averaged *PKP* precursor with single scattering theory (*Hedlin et al.*, 1997), and it is also smaller than the latest result from modeling the high-frequency *P* wave coda using the same approach as in this study. However, it is more or less consistent with the result of *Margerin and Nolet* (2003b), who obtained 0.1% r.m.s. perturbation by modeling the average precursor using another multiple-scattering method by selecting the seismograms with strong precursors only. Our data selection criteria was to include all the seismograms with high SNRs, regardless of the visibility of precursors, therefore, we would expect that our data would yield a smaller r.m.s. velocity perturbation since both studies use multiple-scattering approaches.

Modeling the average precursor amplitudes gives us some insight about the average intensity of mantle scattering due to small-scale heterogeneities. However, we find that the precursor amplitudes vary a lot from place to place as shown in Figure 4.12 with the standard deviations. Although some regions with weaker or similar precursors compared with the global average are identifiable from the map, for instance, off-shore of South America, the southern part of Atlantic ocean, central America, Australia and the northern part of Southeast Asia, the distribution of strong precursor amplitudes is variable. Even within a small geographic region, for example, the southeast Asian islands and North America, the precursor amplitudes exhibit small-scale lateral variations as discovered by *Vidale and Hedlin* (1998), who found that two groups of events which sample slightly different patches of the CMB displayed very different precursors. Therefore, although uniform scattering in-

tensity throughout the lower mantle can provide a reasonable fit to the observed globally averaged precursor, how well this type of scattering model represents the real situation is questionable. It is possible that strong small-scale scatterers are located at some places while other places have very weak small-scale heterogeneities. The possible origin of the small-scale heterogeneities may come from subducted oceanic lithosphere (*Davies, 1984*) and their lateral variation may imply that the lower mantle is not perfectly mixed by mantle convection and subducted oceanic lithosphere can survive in the mantle for billions of years (*Gurnis and Davies, 1986; Christensen and Hoffmann, 1994*).

Appendix A

Copyright Permission

Request of Copyright Permission:

To Whom It May Concern,

My name is Zuihong Zou and I'm a PhD candidate in geophysics at Saint Louis University. I published a paper in Geophys. J. Int. (details below) and I plan to make it part of my PhD thesis. I am writing to ask for a copyright permission for reproducing the whole article.

The details of the article is following:

Title: 'Partial melt in the lowermost mantle near the base of a plume'

Authors: Zuihong Zou, Felipe Leyton and Keith D. Koper

Journal: Geophys. J. Int.

Volume: 168

Pages: 809-817

Doi: 10.1111/j.1365-246X.2006.03266.x

Year: 2007

The details of my PhD thesis:

Title: 'STUDY OF DEEP EARTH STRUCTURE USING CORE PHASES AND THEIR SCATTERED ENERGY RECORDED AT SEISMIC ARRAYS'

Author: Z. Zou

Year: 2008

University: Saint Louis University, Dept. Earth & Atmosph. Sciences

Thank you for your time.

Sincerely,

Zuihong Zou, PhD Candidate

email: zoukathy@gmail.com

Address: Dept. Earth & Atm. Scs. - Saint Louis University
3642 Lindell Blvd., Saint Louis, MO 63108, USA

Phone: (1-314) 977-3654 Fax: (1-314) 977-3117

Reply from the Publisher:

Dear Zuihong Zou,

Thank you for your email request. Permission is granted for you to use the material below for your thesis, subject to the usual acknowledgements and on the understanding that you will reapply for permission if you wish to distribute or publish your thesis commercially.

With best wishes,

Sally

Sally Byers

Permissions Assistant

Wiley-Blackwell Publishing Ltd.

PO Box 805, 9600 Garsington Road

Oxford OX4 2DQ UK

Tel.01865 476149 Fax. 01865 471149

Requests for permission to reprint material from this journal should be addressed to:

Journals Rights & Permissions Controller

Blackwell Publishing Ltd

9600 Garsington Road

Oxford OX4 2DQ UK

Email: JournalsRights@oxon.blackwellpublishing.com

References

- Adams, R. D., and M. J. Randall (1964), The fine structure of the Earth's core, *Bull. Seismol. Soc. Am.*, *54*, 1299–1313.
- Aki, K. (1969), Analysis of seismic coda of local earthquakes as scattered waves, *J. Geophys. Res.*, *74*, 615–631.
- Aki, K., and P. G. Richards (2002), *Quantitative Seismology*, University Science Books, Sausalito, California.
- Alexander, S. S., and R. Phinney (1966), A study of the core-mantle boundary using P waves diffracted by the Earth's core, *J. Geophys. Res.*, *71*, 5943–5958.
- Anderson, D. L. (1967), Phase changes in the upper mantle, *Science*, *157*, 1165–1173.
- Anderson, W. W., and T. J. Ahrens (1994), An equation of state for liquid iron and implications for the Earth's core, *J. Geophys. Res.*, *99*, 4273–4284.
- Bataille, K., and S. M. Flatte (1988), Inhomogeneities near the core-mantle boundary inferred from short-period scattered *PKP* waves recorded at the global digital seismograph networks, *J. Geophys. Res.*, *93*, 15,057–15,064.
- Bataille, K., R. Wu, and S. Flatte (1990), Inhomogeneities near the core-mantle boundary evidenced from scattered waves: A review, *PAGEOPH*, *132*, 151–174.
- Bergman, M. I. (1997), Measurements of elastic anisotropy due to solidification texturing and the implications for the Earth's inner core, *Nature*, *389*, 60–63.
- Bergman, M. I. (2003), Solidification of Earth's core, in *Earth's Core: Dynamics, Structure, Rotation*, edited by V. Dehant, K. C. Creager, S. Karato, and S. Zatman, pp. 105–127, AGU monograph.

- Bergman, M. I., M. Macleod-Silberstein, M. Haskel, B. Chandler, and N. Akpan (2005), A laboratory model for solidification of Earth's core, *Phys. Earth Planet Int.*, 153, 150–164.
- Bhattacharyya, J., P. Shearer, and G. Masters (1992), Inner core attenuation from short-period $PKP(BC)$ versus $PKP(DF)$, *J. Geophys. Res.*, 97, 6573–6586.
- Birch, F. (1940), The alpha-gamma transformation of iron at high pressures, and the problem of the Earth's magnetism, *AM. J. Sci.*, 238, 192–211.
- Bolt, B. A. (1962), Gutenberg's early PKP observations, *Nature*, 196, 122–124.
- Bolt, B. A. (1964), The velocity of seismic waves near the Earth's center, *Bull. Seismol. Soc. Am.*, 54, 191–208.
- Bostock, M. G., and S. Rondenay (1999), Migration of scattered teleseismic body waves, *Geophys. J. Int.*, 137, 732–748.
- Braña, L., and G. Helffrich (2004), A scattering region near the core-mantle boundary under the north atlantic, *Geophys. J. Int.*, 158, 625–636.
- Buchbinder, G. G. R. (1971), Velocity structure of the Earth's core, *Bull. Seismol. Soc. Am.*, 61, 429–456.
- Bullen, K. E. (1963), An index of degree of chemical inhomogeneity in the Earth, *Geophys. J. Int.*, 7, 584–592.
- Bullen, K. E., and T. N. Burke-Gaffney (1958), Diffracted seismic waves near the PKP caustic, *Geophys. J. Int.*, 1, 9–17.
- Cao, A., and B. Romanowicz (2004), Hemispherical transition of seismic attenuation at the top of the Earth's inner core, *Earth Planet. Sci. Lett.*, 228, 243–253.
- Cao, A., W. Masson, and B. Romanowicz (2007), Short wavelength topography on the inner-core boundary, *PNAS*, 104, 31–35, doi:10.1073/pnas.0609810104.
- Červený, V. (2001), *Seismic Ray Theory*, Cambridge University Press.

- Chernov, L. A. (1960), *Wave Propagation in a Random Medium*, (trans. Silverman, R.A.) McGraw-Hill, New York.
- Choy, G. L., and V. F. Cormier (1983), The structure of the inner core inferred from short-period and broadband GDSN data, *Geophys. J. R. astr. Soc.*, *72*, 1–21.
- Choy, G. L., V. F. Cormier, R. Kind, G. Muller, and P. G. Richards (1980), A comparison of synthetic seismograms of core phases generate by the full wave theory and by the reflectivity method, *Geophys. J. R. astr. Soc.*, *61*, 21–39.
- Christensen, U. R., and A. W. Hoffmann (1994), Segregation of subducted oceanic crust in the convecting mantle, *J. Geophys. Res.*, *99*, 19,867–19,884.
- Cleary, J. R., and R. A. W. Haddon (1972), Seismic wave scattering near the CMB: A new interpretation of precursors to *PKP*, *Nature*, *240*, 549–551.
- Copley, S., A. Giamei, S. Johnson, and M. Hornbecker (1970), The origin of freckles in unidirectionally solidified casting, *Metall. Trans.*, *1*, 2193–2204.
- Cormier, V., and P. Ricards (1976), Comments on “The Damping of Core Waves” by Anthony Qamar and Alfredo Eisenberg, *J. Geophys. Res.*, *81*, 3066–3068.
- Cormier, V. F. (1981), Short-period *PKP* phases and the anelastic mechanism of the inner core, *Phys. Earth Planet Int.*, *24*, 291–301.
- Cormier, V. F. (1995), Time domain modeling of *PKIKP* precursors for constraints on the heterogeneity in the lowermost mantle, *Geophys. J. Int.*, *212*, 725–736.
- Cormier, V. F. (1999), Anisotropy of heterogeneity scale lengths in the lower mantle from *PKIKP* precursors, *Geophys. J. Int.*, *136*, 373–384.
- Cormier, V. F. (2007), Texture of the uppermost inner core from forward- and back-scattered seismic waves, *Earth Planet. Sci. Lett.*, doi:10.1016/j.epsl.2007.04.003.
- Cormier, V. F., and X. Li (2002), Frequency dependent attenuation in the inner core: Part II. A scattering and fabric interpretation, *J. Geophys. Res.*, *107*(B12), doi:10.1029/2002JB001796.

- Cormier, V. F., and P. Richards (1977), Full wave theory applied to a discontinuous velocity increase: The inner core boundary, *J. Geophys. Res.*, *43*, 3–31.
- Cormier, V. F., and P. Richards (1988), Spectral synthesis of body waves in earth models specified by vertically varying layers, in *Seismological Algorithms, Computational Methods and Computer Programs*, edited by D. J. Dornboos, Academic Press.
- Creager, K. (1992), Anisotropy of the inner core from differential travel times of the phases *PKP* and *PKIKP*, *Nature*, *356*, 309–314.
- Davies, G. F. (1984), Geophysical and isotropic constraints on mantle convection: an interim synthesis, *J. Geophys. Res.*, *89*, 6017–6040.
- Doornbos, D. J. (1978), On seismic wave scattering by a rough core-mantle boundary, *Geophys. J. R. astr. Soc.*, *53*, 643–662.
- Doornbos, D. J., and E. S. Husebye (1972), Array analysis of *PKP* phases and their precursors, *Phys. Earth Planet Int.*, *5*, 387–399.
- Dziewonski, A., and F. Gilbert (1971), Solidity of the inner core of the Earth inferred from normal mode observations, *Nature*, *234*, 465–466.
- Dziewonski, A. M., and D. L. Anderson (1981), Preliminary reference Earth model, *Phys. Earth Planet Int.*, *25*, 297–356.
- Garcia, R. (2002), Constraints on upper inner core structure from waveform inversion of core phases, *Geophys. J. Int.*, *150*, 651–664.
- Garcia, R., H. Tkalčić, and S. Chevrot (2006), A new global *PKP* data set to study Earth's core and deep mantle, *Phys. Earth Planet Int.*, doi:10.1016/j.pepi.2006.05.003.
- Garnero, E. J., J. S. Revenaugh, Q. Williams, T. Lay, and L. H. Kellogg (1998), Ultralow velocity zone at the core-mantle boundary, in *The Core-Mantle Boundary Region, Geodynamics Series, Vol. 28*, edited by M. Gurnis, M. Wyssession, E. Knittle, and B. Buffet, pp. 319–334, American Geophysical Union.

- Grand, S. P., R. D. van der Hilst, and S. Widiyantoro (1997), Global seismic tomography: A snapshot of convection in the Earth, *GSA today*, 7, 1–7.
- Gubbins, D., G. Masters, and F. Nimmo (2007), A thermo-chemical boundary layer at the base of Earth's outer core and independent estimate of core heat flux, *Geophys. J. Int.*, *Submitted*, Preprint.
- Gurnis, M., and G. F. Davies (1986), Mixing in numerical models of mantle convection incorporating plate tectonics, *J. Geophys. Res.*, 91, 6375–6395.
- Gutenberg, B. (1913), Über die konstitution des Erdinnern, weschlossen aus Erdbebenbeobachtungen, *Z. Geophys.*, 14, 1217–1218.
- Gutenberg, B. (1957), The boundary of the Earth's inner core, *Eos Trans. AGU*, 38, 750–753.
- Gutenberg, B., and C. F. Richter (1934), On seismic waves: I, *Gerlands Beitr. Geophysik.*, 43, 56–133.
- Haddon, R. A. W., and J. R. Cleary (1974), Evidence for scattering of seismic *PKP* waves near the core-mantle boundary, *Phys. Earth Planet Int.*, 8, 211–234.
- Hedlin, M. A. H., and P. M. Shearer (2000), An analysis of large-scale variations in small-scale mantle heterogeneity using Global Seismographic Network recordings of precursors to *PKP*, *J. Geophys. Res.*, 105, 13,655–13,673.
- Hedlin, M. A. H., and P. M. Shearer (2002), Probing mid-mantle heterogeneity using *PKP* coda waves, *Phys. Earth Planet Int.*, 130, 195–208.
- Hedlin, M. A. H., P. M. Shearer, and P. S. Earle (1997), Seismic evidence for small-scale heterogeneity throughout the Earth's mantle, *Nature*, 387, 145–150.
- Herrmann, R. B., and B. Mandal (1986), A study of wavenumber integration techniques, *Earthquakes Notes*, 57, 33–40.
- Holland, K. G., and T. J. Ahrens (1997), Melting of $(Mg, Fe)_2SiO_4$ at the core-mantle boundary of the Earth, *Science*, 275, 1623–1625.

- Huang, B. S. (1996), Investigation of the inner-outer core boundary structure from the seismograms of a deep earthquake recorded by a regional seismic array, *Geophys. Res. Lett.*, *23*, 209–212.
- Jeffreys, H. (1939), The times of the core waves, *Mon. Not. R. Astr. Soc. Geophys. Suppl.*, *4*, 498.
- Johnson, L. (1967), Array measurements of P velocities in the upper mantle, *J. Geophys. Res.*, *72*, 6309–6325.
- Kaneshima, S., K. Hirahara, T. Ohtaki, and Y. Yoshida (1994), Seismic structure near the inner core-outer core boundary, *Geophys. Res. Lett.*, *21*, 157–160.
- Kennett, B. L. N., and E. R. Engdahl (1991), Traveltimes for global earthquake location and phase identification, *Geophys. J. Int.*, *105*, 429–465.
- Kennett, B. L. N., E. R. Engdahl, and R. Buland (1995), Constraints on seismic velocities in the Earth from travel times, *Geophys. J. Int.*, *122*, 108–124.
- Koper, K. D. (2005), The generic array processing (GAP) software package, (abstract), *annual meeting of the Seismological Society of America*.
- Koper, K. D., and M. Dombrovskaya (2005), Seismic properties of the inner core boundary from $PKiKP/P$ amplitude ratios, *Earth Planet. Sci. Lett.*, *237*, 680–694.
- Koper, K. D., M. L. Pyle, and J. M. Franks (2003), Constraints on aspherical core structure from $PKiKP - PcP$ differential travel times, *J. Geophys. Res.*, *108*, doi: 10.1029/2002JB001995.
- Koper, K. D., J. Franks, and M. Dombrovskaya (2004), Evidence for small-scale heterogeneity in Earth's inner core from a global study of $PKiKP$ coda waves, *Earth Planet. Sci. Lett.*, *228*, 227–241.
- Krasnoshchekov, D. N., P. B. Kaazik, and V. M. Ovtchinnikov (2005), Seismological evidence for mosaic structure of the surface of the Earth's inner core, *Nature*, *435*, 483–487.

- Lay, T., J. Hernlund, E. Garnero, and M. S. Thorne (2006), A post-perovskite lens and D'' heat flux beneath the central Pacific, *Science*, *314*, 1272–1276.
- Lehmann, I. (1936), P', *Bur. Cent. Seismol. Int.*, *14*, 3–31.
- Lei, J., and D. Zhao (2006), A new insight into the Hawaiian plume, *Earth Planet. Sci. Lett.*, *241*, 438–453.
- Leyton, F., and K. D. Koper (2007), Using PKiKP coda to determine inner core structure: 2. Determination of Q_c , *J. Geophys. Res.*, doi:10.1029/2006JB004370.
- Li, X., and V. F. Cormier (2002), Frequency dependent attenuation in the inner core: Part I. A viscoelastic interpretation, *J. Geophys. Res.*, *107*(B12), doi:10.1029/2002JB001795.
- Loper, D. E. (1978), Some thermal consequences of a gravitationally powered dynamo, *J. Geophys. Res.*, *83*, 5961–5970.
- Loper, D. E., and P. Roberts (1978), On the motion of an iron-alloy core containing a slurry. I. General theory, *Geophys. Astrophys. Fluid Dyn.*, *9*, 289–321.
- Loper, D. E., and P. H. Roberts (1981), A study of the conditions at the inner core boundary of the Earth, *Phys. Earth Planet Int.*, *24*, 302–307.
- Margerin, L., and G. Nolet (2003a), Multiple scattering of high-frequency seismic waves in the deep Earth: Modeling and numerical examples, *J. Geophys. Res.*, *108*, doi:10.1029/2002JB001974.
- Margerin, L., and G. Nolet (2003b), Multiple scattering of high-frequency seismic waves in the deep Earth: PKP precursor analysis and inversion for mantle granularity, *J. Geophys. Res.*, *108*, doi:10.1029/2003JB002455.
- Menke, W. (1982), On extending Biot's theory of multiple scattering at low frequencies from acoustic to elastic media, *Geophys. J. R. astr. Soc.*, *69*, 819–830.
- Menke, W. (1989), *Geophysical data analysis: Discrete inverse theory*, Academic Press, San Diego.

- Montelli, R., G. Nolet, F. A. Dahlen, G. Masters, E. R. Engdahl, and S. H. Hung (2004), Finite-frequency tomography reveals a variety of plumes in the mantle, *Science*, *303*, 338–343.
- Montelli, R., G. Nolet, F. Dahlen, and G. Masters (2006), A catalogue of deep mantle plumes: new results from finite-frequency tomography, *Geochem. Geophys. Geosys. - G Super* *3*, *7*, doi:10.1029/2006GC001248.
- Nakanishi, I. (1990), High-frequency waves following PKP_{Cdiff} at distances greater than 155° , *Geophys. Res. Lett.*, *17*, 639–642.
- Niazi, M., and D. L. Anderson (1965), Upper mantle structure of western North America from apparent velocities of P waves, *J. Geophys. Res.*, *70*, 4633–4640.
- Niu, F., and L. Wen (2001a), Hemispherical variations in seismic velocity at the top of the Earth's inner core, *Nature*, *410*, 1081–1084.
- Niu, F., and L. Wen (2001b), Strong seismic scatterers near the core-mantle boundary west of Mexico, *Geophys. Res. Lett.*, *28*, 3557–3560.
- Oldham, R. D. (1906), Constitution of the interior of the Earth as revealed by earthquakes, *Q. J. Geol. Soc.*, *62*, 456–475.
- Olson, P., and H. A. Singer (1985), Creeping plumes, *J. Fluid Mech.*, *158*, 511–531.
- Peng, Z., K. Koper, J. E. Vidale, F. Leyton, and P. Shearer (2007), Inner-core fine-scale structure from scattered waves recorded by IAS3, *J. Geophys. Res.*, *Submitted*, Preprint.
- Phinney, R., and S. S. Alexander (1966), P wave diffraction theory and the structure of the core-mantle boundary, *J. Geophys. Res.*, *71*, 5959–5975.
- Poupinet, G., and B. L. N. Kennett (2004), On the observation of high frequency $PKiKP$ and its coda in Australia, *Phys. Earth Planet Int.*, *146*, 497–511.
- Qamar, A. (1973), Revised velocities in the Earth's core, *Bull. Seismol. Soc. Am.*, *63*, 1073–1105.

- Rawlinson, N., and B. Kennett (2004), Rapid estimation of relative and absolute delay times across a network by adaptive stacking, *Geophys. J. Int.*, *157*, 332–340.
- Resovsky, J., J. Trampert, and R. D. van der Hilst (2005), Error bars for the global seismic Q profile, *Earth Planet. Sci. Lett.*, *230*, 413–423.
- Rial, J. A., and V. F. Cormier (1980), Seismic waves at the epicenter’s antipode, *J. Geophys. Res.*, *85*, 2662–2668.
- Rigden, S. M., T. J. Ahrens, and E. M. Stolper (1989), High-pressure equation of state of molten anorthite and diopside, *J. Geophys. Res.*, *94*, 9508–9522.
- Rost, S., and M. Weber (2001), A reflector at 200 km depth beneath the nw Pacific, *Geophys. J. Int.*, *147*, 12–28.
- Rost, S., E. J. Garnero, Q. Williams, and M. Manga (2005), Seismological constraints on a possible plume root at the core-mantle boundary, *Nature*, *435*, 666–669.
- Ruff, L. J., and D. V. Helmberger (1982), The structure of the lowermost mantle determined by short-period P-wave amplitudes, *Geophys. J. R. astr. Soc.*, *68*, 95–119.
- Sacks, I. S., and G. Saa (1969), The structure of the transition zone between the inner core and the outer core, *Yb. Carnegie Inst. Wash.*, *69*, 419–426.
- Sato, H., and M. C. Fehler (1998), *Seismic Wave Propagation and Scattering in the Heterogeneous Earth*, AIP Press, New York.
- Schimmel, M., and H. Paulssen (1997), Noise reduction and detection of weak, coherent signals through phase-weighted stacks, *Geophys. J. Int.*, *130*, 497–505.
- Schulitz, F., Y. Lu, and H. Wadley (1998), Ultrasonic metal powder-viscous liquid suspensions, *J. Acoust. Soc. Am.*, *103*, 1361–1369.
- Shearer, P. (1994), Constraints on inner core anisotropy from *PKP(DF)* travel times, *J. Geophys. Res.*, *99*, 19,647–19,659.

- Shearer, P., M. Hedlin, and P. Earle (1998), PKP and PKKP precursor observations: Implications for the small-scale structure of the deep mantle and core, in *The Core-Mantle Boundary Region, Geodynamics Series, Vol. 28*, edited by M. Gurnis, M. Wysession, E. Knittle, and B. Buffett, pp. 37–55, American Geophysical Union.
- Shearer, P. M., and P. S. Earle (2004), The global short-period wavefield modelled with a monte carlo seismic phonon method, *Geophys. J. Int.*, *158*, 1103–1117.
- Shimizu, H., J. P. Poirier, and J. L. L. Mouel (2005), On crystallization at the inner core boundary, *Phys. Earth Planet Int.*, *151*, 37–51.
- Sleep, N. H. (2002), Ridge-crossing mantle plumes and gaps in tracks, *Geochem. Geophys. Geosys. - G Super 3*, *3*(12), 8505, doi:10.1029/2001GC00290.
- Song, X., and D. V. Helmberger (1992), Velocity structure near the inner core boundary from waveform modeling, *J. Geophys. Res.*, *97*, 6573–6586.
- Song, X., and D. V. Helmberger (1995), A P wave velocity model of Earth's core, *J. Geophys. Res.*, *100*, 9817–9830.
- Song, X., and P. G. Richards (1996), Observational evidence for differential rotation of the Earth's inner core, *Nature*, *382*, 221–224.
- Souriau, A., and G. Poupinet (1991), The velocity profile at the base of the liquid core from *PKP(BC + Cdiff)* data: an argument in favor of radial inhomogeneity, *Geophys. Res. Lett.*, *18*, 2023–2026.
- Souriau, A., and P. Roudil (1995), Attenuation in the uppermost inner core from broad-band GEOSCOPE PKP data, *Geophys. J. Int.*, *123*, 572–587.
- Steinbach, V., and D. A. Yuen (1997), Dynamical effects of a temperature and pressure dependent lower-mantle rheology on the interaction of upwelling with the transition zone, *Phys. Earth Planet Int.*, *103*, 85–100.
- Steinbach, V., and D. A. Yuen (1999), Viscous heating: a potential mechanism for the formation of the ultra low velocity zone, *Earth Planet. Sci. Lett.*, *172*, 213–220.

- Steinberger, B. M., and R. J. O'Connell (1998), Advection of plumes in mantle flow: implications on hotspot motion, mantle viscosity and plume distribution, *Geophys. J. Int.*, *132*, 412–434.
- Stroujkova, A., and V. F. Cormier (2004), Regional variations in the uppermost 100 km of the Earth's inner core, *J. Geophys. Res.*, *109*, doi:10.1029/2004JB002976.
- Tanaka, S. (2005), Characteristics of PKP_{Cdiff} coda revealed by small-aperture seismic arrays: Implications for the study of the inner core boundary, *Phys. Earth Planet Int.*, *153*, 49–60.
- Tichelaar, B. W., and L. J. Ruff (1989), How good are our best models? Jackknifing, bootstrapping, and earthquake depth, *Eos Trans. AGU*, *70*, 605–606.
- Ulrych, T. J., M. D. Sacchi, and S. L. M. Freire (1999), Eigenimage processing of seismic sections, in *Covariance Analysis of Seismic Signal Processing, Geophysical Developments Series, No.8*, edited by R. L. Kirilin and W. J. Done, Society of Exploration Geophysicists, Tulsa.
- Valenzuela, R. W., and M. Wyssession (1998), Illuminating the base of the mantle with diffracted waves, in *The Core-Mantle Boundary Region, Geodynamics Series 28*, pp. 57–71, American Geophysical Union.
- van Decar, J. C., and R. Crosson (1990), Determination of teleseismic relative phase arrival times using multi-channel cross-correlation and least squares, *Bull. Seismol. Soc. Am.*, *80*, 150–159.
- van der Hilst, R. D., S. Widiyantoro, and E. Engdahl (1997), Evidence for deep mantle circulation from global tomography, *Nature*, *386*, 578–584.
- Vidale, J. E., and P. Earle (2000), Fine-scale heterogeneity in the Earth's inner core, *Nature*, *404*, 273–275.
- Vidale, J. E., and M. A. H. Hedlin (1998), Evidence for partial melt at the core-mantle boundary north of Tonga from the strong scattering of seismic waves, *Nature*, *391*, 682–685.

- Vinnik, L., B. Romanowicz, and L. Bréger (1994), Anisotropy in the center of the inner core, *Geophys. Res. Lett.*, *21*, 1671–174.
- Wen, L. (2000), Intense seismic scattering near the Earth's core-mantle boundary beneath the Comoros hotspot, *Geophys. Res. Lett.*, *27*, 3627–3630.
- Wen, L. (2006), Localized temporal change of the Earth's inner core boundary, *Science*, *314*, 967–970.
- Wen, L., and D. V. Helmberger (1998), Ultra-low velocity zones near the core-mantle boundary from broadband *PKP* precursors, *Science*, *279*, 1701–1703.
- Wen, L., and F. Niu (2002), Seismic velocity and attenuation structures in the top of the Earth's inner core, *J. Geophys. Res.*, *107*, doi:10.1029/2001JN000170.
- Williams, Q., and E. J. Garnero (1996), Seismic evidence for partial melt at the base of Earth's mantle, *Science*, *273*, 1528–1530.
- Williams, Q., J. S. Revenaugh, and E. J. Garnero (1998), A correlation between ultra-low basal velocities in the mantle and hot spots, *Science*, *281*, 546–549.
- Wu, R. S., and K. Aki (1985a), Elastic wave scattering by a random medium and the small-scale inhomogeneities in the lithosphere, *J. Geophys. Res.*, *90*, 10,261–10,273.
- Wu, R. S., and K. Aki (1985b), Scattering characteristics of elastic waves by an elastic heterogeneity, *Geophysics*, *50*, 582–595.
- Yu, W., and L. Wen (2006), Seismic velocity and attenuation structures in the top 400 km of the Earth's inner core along equatorial paths, *J. Geophys. Res.*, *111*, doi:10.1029/2005JB003995.
- Yu, W., L. Wen, and F. Niu (2005), Seismic velocity structure in the Earth's outer core, *J. Geophys. Res.*, *110*, doi:10.1029/2003JB002928.
- Zerr, A., A. Diegeler, and R. Boehler (1998), Solidus of Earth's deep mantle, *Science*, *281*, 243–246.

Zhu, L., and L. Rivera (2002), A note on the dynamic and static displacements from a point source in multi-layered media, *Geophys. J. Int.*, 148, 619–627.

Zou, Z., F. Leyton, and K. D. Koper (2007), Partial melt in the lowermost mantle near the base of a plume, *Geophys. J. Int.*, 168, 809–817.

Vita Auctoris

Zuihong Zou was born in Linchuan of Jiangxi Province, a beautiful town famous for poet and prose writers in the history of China. As the youngest child among five siblings, Zuihong got an early education from her older brothers and sister before school age, which was one of the reasons that she excelled in most of the subjects taught in school.

In 1995, Zuihong graduated from high school with the 2nd highest total score in town in the higher education entrance examination, and decided to continue her education in the highly prestigious Peking University in China. At Peking University, she got essential training in advanced mathematics, physics, and first learned about the mysteries of the Earth. After she got her bachelor's degree in geophysics in the Department of Geophysics at Peking University in June 1999, she decided to explore her career in seismology and continued her study in the same department.

In June 2002, she received her master of science degree in Geophysics awarded as an outstanding master's thesis. Three years of study and research towards the master's degree inspired her deeper interests in the Earth. She decided to follow her thesis advisor's career path and applied for the PhD program at the universities in the United States to further her research.

In August 2002, Zuihong joined University of Illinois at Urbana-Champaign in the USA as a graduate student in seismology. After spending one and a half years at UIUC, she moved to Saint Louis University to study the deep earth structure in the Earth and Atmospheric Sciences department. From then on, she has devoted her full-time to the study of the core and the lower mantle. Zuihong expects to receive the Doctor of Philosophy in Geophysics in March 2008 from Saint Louis University.